

1 **Atomically Dispersed Antimony on Carbon Nitride for the Artificial Photosynthesis**  
2 **of Hydrogen Peroxide**

3 Zhenyuan Teng,<sup>1,7,8</sup> Qitao Zhang,<sup>2,8</sup> Hongbin Yang,<sup>3,8</sup> Kosaku Kato,<sup>4</sup> Wenjuan Yang,<sup>2</sup> Ying-  
4 Rui Lu,<sup>5</sup> Sixiao Liu,<sup>6,7</sup> Chengyin Wang,<sup>6,7</sup> Akira Yamakata,<sup>4</sup> Chenliang Su,<sup>2,\*</sup> Bin Liu,<sup>3,\*</sup> and  
5 Teruhisa Ohno<sup>1,7,\*</sup>

6  
7 <sup>1</sup>Department of Applied Chemistry, Faculty of Engineering, Kyushu Institute of Technology,  
8 Kitakyushu 804-8550, Japan

9 <sup>2</sup>International Collaborative Laboratory of 2D Materials for Optoelectronics Science and  
10 Technology of Ministry of Education, Institute of Microscale Optoelectronics, Shenzhen  
11 University, Shenzhen 518060, China

12 <sup>3</sup>School of Chemical and Biomedical Engineering, Nanyang Technological University, 62  
13 Nanyang Drive, Singapore 637459, Singapore

14 <sup>4</sup>Graduate School of Engineering, Toyota Technological Institute, 2-12-1 Hisakata,  
15 Tempaku Nagoya 468-8511, Japan

16 <sup>5</sup>National Synchrotron Radiation Research Center, Hsinchu 30076, Taiwan

17 <sup>6</sup>College of Chemistry and Chemical Engineering, Yangzhou University, 180 Si-Wang-Ting  
18 Road, Yangzhou 225002, China

19 <sup>7</sup>Joint Laboratory of Yangzhou University, Kyushu Institute of Technology, Yangzhou  
20 University, 180 Si-Wang-Ting Road, Yangzhou 225002, China

21 <sup>8</sup>These authors contributed equally.

22 ORCID:

23 Teruhisa Ohno: <https://orcid.org/0000-0002-7825-8189>

24 Chenliang Su: <https://orcid.org/0000-0002-8453-1938>

25 Bin Liu: <https://orcid.org/0000-0002-4685-2052>

26 E-mail address:

27 Teruhisa Ohno: [tohno@che.kyutech.ac.jp](mailto:tohno@che.kyutech.ac.jp)

28 Chenliang Su: [chmsuc@nus.edu.sg](mailto:chmsuc@nus.edu.sg)

29 Bin Liu: [liubin@ntu.edu.sg](mailto:liubin@ntu.edu.sg)

30 **Abstract**

**Commented [TB1]:** \* The choice of title is largely yours and must be under 150 characters. However, we think it may be good to include "carbon nitride" so we suggest the alternative:

"Atomically Dispersed Antimony on Carbon Nitride for the artificial Photosynthesis of Hydrogen Peroxide"

**Commented [TB2R1]:** We agree with the editor that the revised title is more specific. We have changed the title of this work.

31 Artificial photosynthesis offers a promising strategy to produce hydrogen peroxide  
32 ( $\text{H}_2\text{O}_2$ ) – an environmentally friendly oxidant and a clean fuel. However, the low activity and  
33 selectivity of the two-electron oxygen reduction reaction (ORR) in the photocatalytic  
34 process greatly restricts the  $\text{H}_2\text{O}_2$  production efficiency. Here we show a robust antimony  
35 single-atom photocatalyst (Sb-SAPC, single-Sb-atom dispersed on carbon nitride) for the  
36 synthesis of  $\text{H}_2\text{O}_2$  in a simple water and oxygen mixture under visible light irradiation. An  
37 apparent quantum yield of 17.6% at 420 nm together with a solar-to-chemical conversion  
38 efficiency of 0.61% for  $\text{H}_2\text{O}_2$  synthesis was achieved. Based on time-dependent density  
39 function theory calculations, isotopic experiments and advanced spectroscopic  
40 characterizations, the outstanding photocatalytic performance is ascribed to the  
41 significantly promoted two-electron ORR by forming  $\mu$ -peroxide at the Sb sites and highly  
42 concentrated holes at the neighboring N atoms. The *in-situ* generated  $\text{O}_2$  via water  
43 oxidation is rapidly consumed by ORR, leading to boosted overall reaction kinetics.

## 44 45 Introduction

46 Hydrogen peroxide ( $\text{H}_2\text{O}_2$ ) is an important green oxidant<sup>1</sup> widely used in a variety of  
47 industries and a promising clean fuel for jet car and rockets<sup>2-7</sup> (60 wt.%  $\text{H}_2\text{O}_2$  has an energy  
48 density of 3.0 MJ L<sup>-1</sup>, higher than compressed  $\text{H}_2$  gas at 35 MPa, 2.8 MJ L<sup>-1</sup>). Currently,  
49  $\text{H}_2\text{O}_2$  is manufactured by the energy-consuming, waste-intensive, and indirect  
50 anthraquinone method<sup>8,9</sup>. Photocatalytic  $\text{H}_2\text{O}_2$  synthesis on semiconductor materials from  
51 water and oxygen has emerged as a safe, environmental-friendly and energy-saving  
52 process<sup>10,11</sup>. To achieve high selectivity and rate for  $\text{H}_2\text{O}_2$  production, it is crucial to boost  
53 the 2e<sup>-</sup> oxygen reduction reaction (ORR, Equation 1)<sup>12</sup> or the 2e<sup>-</sup> water oxidation reaction  
54 (WOR, Equation 2)<sup>13</sup>. The light-driven 2e<sup>-</sup> WOR pathway is difficult to be achieved because  
55 of the uphill thermodynamics (1.76 V vs. NHE), i.e. the as-synthesized  $\text{H}_2\text{O}_2$  will  
56 decompose at this highly oxidative potential since  $\text{H}_2\text{O}_2$  is an excellent hole  
57 scavenger<sup>11,14,15</sup>. On the contrary, the 2e<sup>-</sup> ORR pathway has been realized for artificial  
58 photosynthesis of  $\text{H}_2\text{O}_2$  in several particulate systems<sup>12,16-23</sup>. However, the highest  
59 apparent quantum yield ( $\Phi\text{AQY}$ ) for non-sacrificial  $\text{H}_2\text{O}_2$  production (Equation 3) is still  
60 smaller than 8% (at  $\lambda = 420 \text{ nm}$ )<sup>16-24</sup>, much lower than the highest  $\Phi\text{AQY}$  values reached

Commented [TB3]: The abstract — which should be roughly 150 words long and contain no references — should serve both as a general introduction to the topic and a non-technical summary of your main results and their implications. It should contain a brief account of the background and rationale of the work, followed by a statement of the main conclusions introduced by the phrase 'Here we show' or some equivalent phrase. Because we hope that researchers in a wide range of disciplines will be interested in your work, the abstract should be as accessible as possible, explaining essential but specialized terms concisely. We encourage you to show your abstract to colleagues outside of your direct field of expertise to uncover any problematic concepts.

Commented [TB4R3]: We have revised the abstract to meet the requirements.

Commented [TB5]: Please remove this, We avoid the use of phrases such as 'novel', 'for the first time', 'record', etc. This should be clear from the context.

Commented [TB6R5]: We have removed all phrases of ('novel', 'for the first time', 'record') in both manuscript and supplementary information.

Commented [TB7]: spectroscopic

Commented [TB8R7]: We have revised the word 'spectral' to 'spectroscopic'.

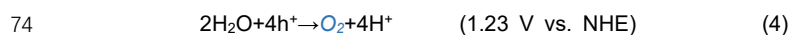
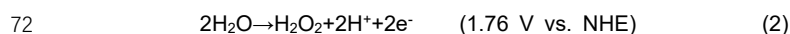
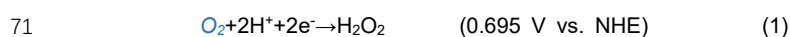
Commented [TB9]: Please avoid the repetition of because, change to "since"

Commented [TB10R9]: We have change the word 'because' to 'since' to avoid the repetition.

Commented [TB11]: In the introduction, we realised that some sentences have a high degree of overlap with your recent <https://doi.org/10.1016/j.apcatb.2020.119589>. Please revise the sentences or add the appropriate citation to this work.

Commented [TB12R11]: We have added the appropriate citations.

61 for overall water splitting (~30% at  $\lambda = 420 \text{ nm}$ )<sup>25</sup>. To boost the photocatalytic activity for  
62 the non-sacrificial H<sub>2</sub>O<sub>2</sub> production, both 2e<sup>-</sup> ORR (Equation 2) and 4e<sup>-</sup> WOR (Equation 4)  
63 should be promoted simultaneously. Unlike some other photocatalytic processes (e.g.,  
64 overall water splitting and N<sub>2</sub> fixation)<sup>25,26</sup>, these redox reactions cannot be separately  
65 considered as irrelevant half reactions, since O<sub>2</sub> is not only a product in the 4e<sup>-</sup> WOR  
66 (Equation 4), but also a reactant in the 2e<sup>-</sup> ORR (Equation 1). If the *in-situ* generated O<sub>2</sub>  
67 from WOR (Equation 4) can be consumed rapidly by ORR, it will kinetically facilitate the  
68 WOR. Therefore, introducing highly active and selective sites for the 2e<sup>-</sup> ORR in the  
69 photocatalytic system to consume the O<sub>2</sub> generated from the WOR shall offer a promising  
70 strategy for breaking the bottleneck of photocatalytic H<sub>2</sub>O<sub>2</sub> synthesis.



76 Manipulating metallic sites can change both the activity and selectivity of ORR<sup>27</sup>. The  
77 O<sub>2</sub> molecular adsorption on metal surface can be generally classified into three types  
78 (Figure 1a): Pauling-type (end-on), Griffiths-type (side-on), and Yeager-type (side-on)<sup>27,28</sup>.  
79 The end-on O<sub>2</sub> adsorption configuration is able to minimize the O-O bond breaking, leading  
80 to a suppressed 4e<sup>-</sup> ORR (Equation 5), and thus, a highly selective 2e<sup>-</sup> ORR. On metal  
81 particles, both end-on and side-on O<sub>2</sub> molecular adsorption exist, and thus the O-O bond  
82 splitting on the surface of metal particles can hardly be prevented<sup>29,30</sup>. Benefiting from the  
83 desirable features of single atom catalyst (SAC), the adsorption of O<sub>2</sub> molecules on  
84 atomically isolated sites is usually end-on type, which therefore could reduce the possibility  
85 of O-O bond breaking (Figure 1b)<sup>31-34</sup>. For instance, SACs with Pt<sup>2+</sup><sup>35</sup> and Co-N<sub>4</sub><sup>36,37</sup>  
86 centers could electrochemically reduce O<sub>2</sub> to H<sub>2</sub>O<sub>2</sub> via a 2e<sup>-</sup> ORR pathway with ultrahigh  
87 selectivity (>96 %). However, Pt<sup>2+</sup> and Co-N<sub>4</sub> sites can hardly be coupled in the  
88 photocatalytic system due to their high charge recombination characteristics, which  
89 originate from the intermediate band formed by the half-filled d electrons. Constructing  
90 photocatalysts with atomically dispersed elements possessing the d<sup>10</sup> electronic

Commented [TB13]: the highest AQY values reached for

Commented [TB14R13]: We have changed the word 'current record  $\Phi$ AQY for' to 'the highest  $\Phi$ AQY values reached for'.

91 configuration can eliminate the formation of the intermediate band in the band structure,  
92 which shall be favorable for efficient charge separation and formation of reactive centers  
93 with high density of electrons/holes<sup>15,38,39</sup>. This implies that SACs with d<sup>10</sup> electronic  
94 configuration would be ideal candidates for photocatalytic H<sub>2</sub>O<sub>2</sub> synthesis via the 2e<sup>-</sup> ORR.

95 Herein, we develop a Sb single atom photocatalyst (Sb-SAPC) for non-sacrificial  
96 photocatalytic H<sub>2</sub>O<sub>2</sub> synthesis in a water and oxygen mixture under visible light irradiation,  
97 in which the oxidation state of Sb is regulated to +3 with a 4d<sup>10</sup>5s<sup>2</sup> electron configuration.

98 Notably, an apparent quantum efficiency of 17.6% at 420 nm and a solar-to-chemical  
99 conversion (SCC) efficiency of 0.61% are achieved on the as-developed photocatalyst.

Commented [TB15]: please rephrase

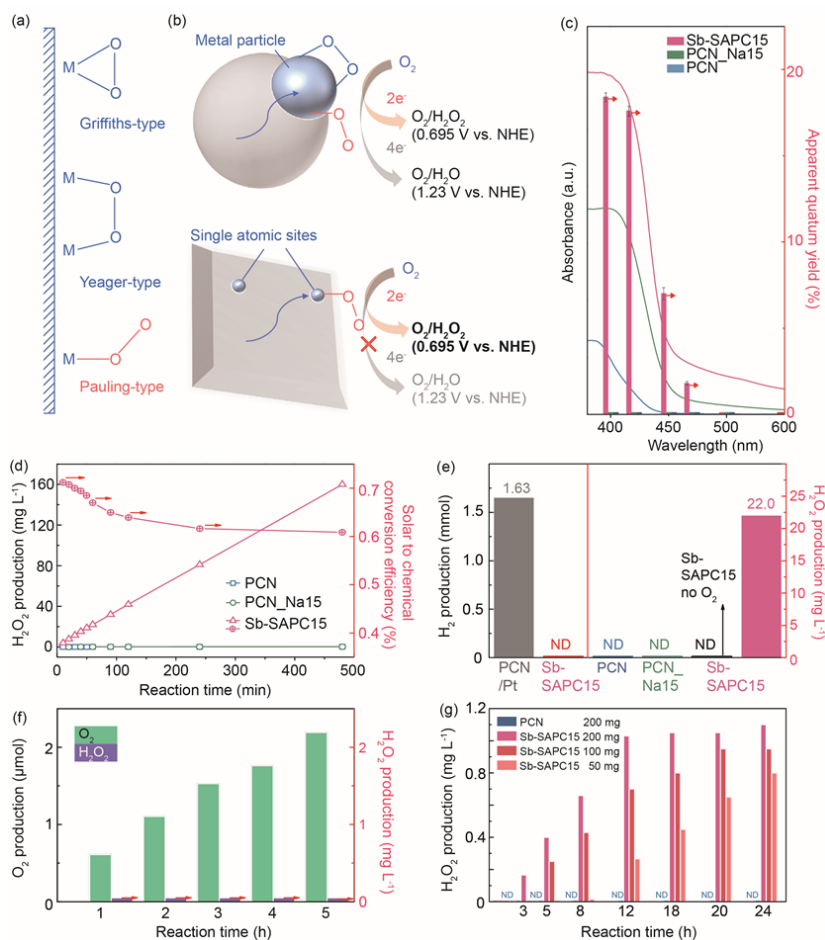
Commented [TB16R15]: We have removed the word record-high.

100 Combining experimental and theoretical investigations, it is found that the adsorption of O<sub>2</sub>  
101 on isolated Sb atomic sites is end-on type, which promotes formation of Sb- $\mu$ -peroxide (Sb-  
102 OOH), leading to an efficient 2e<sup>-</sup> ORR pathway for H<sub>2</sub>O<sub>2</sub> production. More importantly, the  
103 Sb sites also induce highly concentrated holes at the neighboring melem units, promoting  
104 the 4e<sup>-</sup> WOR. The concept of using SAC to simultaneously boost reduction and oxidation  
105 reactions shall provide a design guide to develop more advanced photocatalytic systems  
106 for extensive applications.

Commented [TB17]: this can be removed

Commented [TB18R17]: The word "the" has been removed.

107



108

109 **Figure 1 | Photocatalytic performance of Sb-SAPC toward H<sub>2</sub>O<sub>2</sub> production.** a, Schematic structures  
 110 of O<sub>2</sub> adsorption on metal surface. b, ORR on a metal particle (top) and an isolated atomic site (bottom).  
 111 c, Action spectra of PCN, PCN\_Na15 and Sb-SAPC15 toward H<sub>2</sub>O<sub>2</sub> production in a phosphate buffer  
 112 solution (pH = 7.4). Error bars represent the standard deviations of 3 replicate measurements. d, Solar-  
 113 to-chemical conversion efficiency of PCN, PCN\_Na15 and Sb-SAPC15 under AM 1.5 illumination in a  
 114 phosphate buffer solution. e, Selectivity comparison of Sb-SAPC15 and pristine PCN for different  
 115 photoreduction reactions (Reaction time: 1h). Left: comparison of hydrogen evolution activity of Sb-  
 116 SAPC15 and PCN loaded with 1 wt.% Pt in a 10% (v/v) 2-propanol aqueous solution. Right: comparison  
 117 of activity for photocatalytic H<sub>2</sub>O<sub>2</sub> production on pristine PCN, PCN\_Na15 and Sb-SAPC15 in a phosphate

118 buffer solution with or without O<sub>2</sub>. **f**, Amount of O<sub>2</sub> and H<sub>2</sub>O<sub>2</sub> produced on Sb-SAPC15 in NaIO<sub>3</sub> (0.1 M,  
119 as the electron acceptor) solution. **g**, Photocatalytic H<sub>2</sub>O<sub>2</sub> production with electron acceptor (0.1 mM Ag<sup>+</sup>)  
120 under N<sub>2</sub> atmosphere. Irradiation condition:  $\lambda > 420$  nm (Xe lamp, light intensity at 420-500 nm: 30.3 W  
121 m<sup>-2</sup>), at 298 K. NDs in Figure 1e and Figure 1g mean that H<sub>2</sub>O<sub>2</sub> cannot be detected in the photocatalytic  
122 system.

123

## 124 **Results**

### 125 **Photocatalytic H<sub>2</sub>O<sub>2</sub> production on Sb-SAPC**

126 The Sb-SAPC was prepared by a wet chemical method using NaSbF<sub>6</sub> and melamine  
127 as the precursor (Supplementary Figure 1). Control samples including pristine polymeric  
128 carbon nitride (PCN) and Na<sup>+</sup> incorporated PCNs, were also prepared for references.  
129 According to the amount of metal salt added ( $x = 0.5, 1, 3, 5, 10, 15$  or 20 mmol of NaF or  
130 NaSbF<sub>6</sub>) into 4 g melamine, the samples are denoted as PCN\_Nax or Sb-SAPCx,  
131 respectively. The as-prepared Sb-SAPC reached a quantity of 100 grams in one batch,  
132 which is very promising for scalable production (Supplementary Figure 2).

133 The photocatalytic performance of Sb-SAPC for H<sub>2</sub>O<sub>2</sub> production was assessed in a  
134 water and oxygen mixture without presence of any sacrificial agents under visible light  
135 illumination. As shown in Supplementary Figure 3, Sb-SAPC15 shows the highest H<sub>2</sub>O<sub>2</sub>  
136 production rate (12.4 mg L<sup>-1</sup> in 120 min) among the samples, which is about 248 times  
137 higher than pristine PCN (0.05 mg L<sup>-1</sup> in 120 min). The surface area of Sb-SAPC15 (1.89  
138 m<sup>2</sup> g<sup>-1</sup>, Supplementary Figure 4) is only about 1/7.78 of pristine PCN (14.7 m<sup>2</sup> g<sup>-1</sup>),  
139 indicating that the activity per area enhancement induced by introducing Sb into PCN is  
140 increased by more than 1900 folds as compared to pristine PCN. After we optimized the  
141 reaction conditions (Supplementary Figures 5-6)<sup>19</sup>, the action spectra (Figure 1c) for H<sub>2</sub>O<sub>2</sub>  
142 production were measured. The  $\Phi_{AQY}$  of Sb-SAPC15 at 420 nm is determined to be  
143 17.6%, which is twice of the most efficient photocatalyst (RF-resin, Supplementary Table  
144 1) for non-sacrificial H<sub>2</sub>O<sub>2</sub> production<sup>16</sup>. The solar-to-chemical conversion efficiency of Sb-  
145 SAPC15 reaches as high as 0.61% (Figure 1d), comparable with the most efficient water  
146 splitting photocatalyst (~0.8%)<sup>25</sup>. Interestingly, the Sb-SAPC15 displays negligible  
147 photocatalytic activity for the hydrogen evolution reaction (Figure 1e, left). Furthermore, by

**Commented [TB19]:** \* We do not use combined "Results and Discussion" section. Please change to "Results".

**Commented [TB20R19]:** We have changed the word "Results and Discussion" to "Results".

**Commented [TB21]:** Please shorten any section subheadings that are longer than 60 characters (including spaces).

**Commented [TB22R21]:** This section subheading has been shortened to be no longer than 60 characters (including spaces).

**Commented [TB23]:** Our style does not allow for the use of Schemes.

Please change this into a Supplementary Figure.  
\* Supplementary Figures should be referred to as 'Supplementary Figure 1', etc., in both the SI and main text. Note that the 'S' prefix is not used in the SI-

**Commented [TB24R23]:** We have revised all the styles of Figures in the revised manuscript and supplementary information.

148 comparing the photocatalytic products at two different reaction conditions (with and without  
149 O<sub>2</sub>), the H<sub>2</sub>O<sub>2</sub> is clearly shown to be produced via the 2e<sup>-</sup> ORR (no H<sub>2</sub>O<sub>2</sub> was detected in  
150 the photocatalytic system without O<sub>2</sub>, [Figure 1e, right](#)). Besides activity, more than 95% of  
151 the initial activity (Sb-SAPC15) could be maintained after 5 consecutive photocatalytic runs  
152 indicating the good stability ([Supplementary Figure 7a](#)). Reproducibilities of Sb-SAPC15  
153 (5 different batches) are also excellent for AQY and SCC measurements ([Supplementary](#)  
154 [Figures 7b-c](#)). The long-term stability and potential for scalable photocatalytic H<sub>2</sub>O<sub>2</sub>  
155 production using the Sb-SAPC photocatalyst were demonstrated in a fixed bed reactor  
156 ([Supplementary Figure 8](#)).

157 To study the overall reaction for photocatalytic H<sub>2</sub>O<sub>2</sub> production, the half redox reactions  
158 on Sb-SAPC15 were separately investigated as follows: Sb-SAPC15 in a 2-propanol  
159 aqueous solution (2-propanol as an electron donor, 10% v/v) with saturated O<sub>2</sub>  
160 ([Supplementary Figure 9](#)) and in a NaIO<sub>3</sub> aqueous solution (NaIO<sub>3</sub> as an electron acceptor)  
161 with N<sub>2</sub> ([Figure 1f](#) and [Supplementary Figure 10](#)) respectively under visible light irradiation,  
162 which confirm that the H<sub>2</sub>O<sub>2</sub> is indeed produced via the ORR on Sb-SAPC15. Isotope  
163 experiments<sup>16</sup> ([Supplementary Figure 11](#)) were further performed to verify the 4e<sup>-</sup> WOR  
164 mechanism, in which Sb-SAPC15 in H<sub>2</sub><sup>16</sup>O and <sup>18</sup>O<sub>2</sub> gas was irradiated for 6, 24 and 72 h.  
165 Fe<sup>3+</sup> and high concentration H<sup>+</sup> were added into the reaction system to decompose H<sub>2</sub>O<sub>2</sub>  
166 to release O<sub>2</sub>, and the evolved gas was analyzed by gas chromatography-mass  
167 spectrometry. The gaseous product obtained after 6 h reaction exhibits a strong <sup>18</sup>O<sub>2</sub> (m/z)  
168 peak (94.5%) and a weak <sup>16</sup>O<sub>2</sub> (m/z) peak (25.2%), manifesting that H<sub>2</sub><sup>18</sup>O<sub>2</sub> was produced  
169 by O<sub>2</sub> reduction at the initial stage of the reaction. The gaseous product obtained with  
170 increasing reaction time shows a decreased intensity of <sup>18</sup>O<sub>2</sub> peak (24 h: 55.7%; 72 h:  
171 45.5%) and an increased intensity of <sup>16</sup>O<sub>2</sub> peak (24 h: 32.5%; 72 h: 45.5%), indicating that  
172 the oxygen generated by WOR gradually participated in the ORR process<sup>16</sup>.

173 To quantitatively reveal the relationship between the WOR and ORR, low-concentration  
174 electron acceptor (0.1 mM Ag<sup>+</sup>) was added into the PCN and Sb-SAPC system in the  
175 absence of O<sub>2</sub>. In this case, H<sub>2</sub>O<sub>2</sub> can only be produced via the reduction of O<sub>2</sub> generated  
176 from water oxidation. PCN showed no photocatalytic activity in this condition, while Sb-  
177 SAPC gradually produced H<sub>2</sub>O<sub>2</sub> in a certain time interval. After that, the H<sub>2</sub>O<sub>2</sub> concentration

178 kept constant  $\sim 1.0 \text{ mg L}^{-1}$  no matter how much catalyst was used (Figure 1g). The  
179 quantitative relationship between the amount of added  $\text{Ag}^+$  and  $\text{H}_2\text{O}_2$  produced from WOR  
180 is discussed in Supplementary note 1. Isotope experiment using  $\text{H}_2^{18}\text{O}$  was also  
181 conducted to confirm that the  $\text{H}_2\text{O}_2$  generated in the system is indeed derived from the  $\text{O}_2$   
182 produced by the  $4e^-$  WOR process (Supplementary Figure 12). The intensity of  $^{18}\text{O}_2$  peak  
183 ( $m/z=36$ ) gradually increases with increasing reaction time, indicating that  $\text{H}_2^{18}\text{O}_2$  is  
184 originated from the  $^{18}\text{O}_2$  generated by WOR. Therefore, the  $\text{O}_2$  generated from WOR in  
185 Sb-SAPC system was rapidly consumed by the  $2e^-$  ORR process to produce  $\text{H}_2\text{O}_2$ .

186

### 187 **Characterization of Sb-SAPC**

188 To understand the superb photocatalytic performance of Sb-SAPC for  $\text{H}_2\text{O}_2$  production,  
189 the catalyst synthesis process (Supplementary Figures 13-17, Supplementary note 2) and  
190 the structural characteristics of the as-synthesized catalysts were carefully investigated.  
191 As revealed in the  $\zeta$ -potential measurements, negative surface charges appeared on the  
192 as-prepared Sb-SAPCs to neutralize the positive charges induced by the incorporated Na  
193 and Sb cations (Supplementary Figure 18). The crystalline structures of Sb-SAPCx show  
194 no obvious changes as compared to the pristine PCN, as evidenced in the XRD patterns  
195 and high-resolution transmission electron microscopy (HRTEM) images (Supplementary  
196 note 3, Supplementary Figures 19-20). As a powerful tool for visualizing individual heavy  
197 atoms, high-angle annular dark-field scanning transmission electron microscopy (HAADF-  
198 STEM) was used to further examine the morphology and elemental distribution. The Sb-  
199 SAPC15 is composed of aggregated two-dimensional nanosheets, on which Sb and Na  
200 elements are homogeneously distributed (Supplementary Figure 21). For Sb-SAPC0.5, 1,  
201 3, 5, 10 and 15, Supplementary Figure 22 and Figure 2a show that the bright spots with  
202 high density are uniformly dispersed in the entire carbon nitride matrix. The electron energy  
203 loss spectroscopy (EELS) (Figure 2b and Supplementary Figure 23) measurement reveals  
204 the bright spots corresponding to Sb atoms. The size distribution as displayed in Figure 2a  
205 shows that 99.6% of Sb species are less than 0.2 nm, demonstrating that Sb exists  
206 exclusively as isolated single atoms<sup>40</sup>. The mass ratio of Sb species in Sb-SAPC15 (10.9  
207 wt.%, Supplementary Table 2) is considerably larger than that of the noble or transition

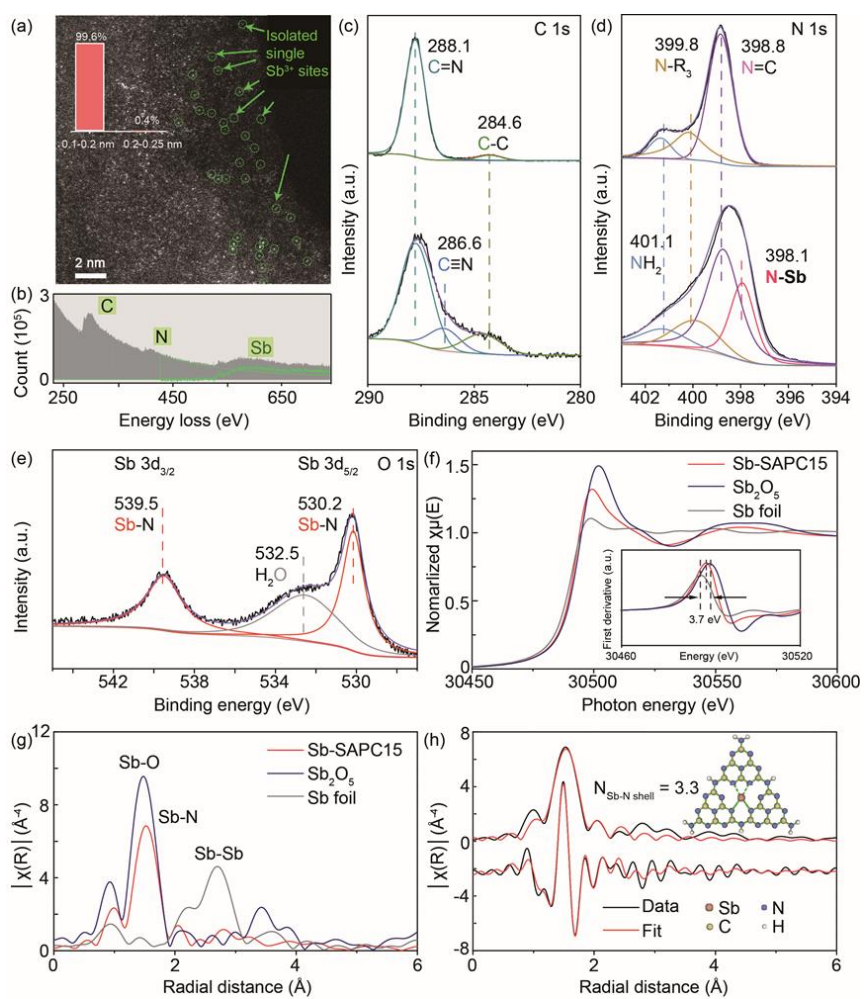


208 metal single atom species in many reported SACs.

209 To investigate the interaction between the isolated Sb atoms and the PCN skeleton, FT-  
210 IR and XPS measurements were conducted. The spectra of PCN, PCN\_Na15 and Sb-  
211 SAPC15 show no obvious difference in the wavenumber range of 700-900  $\text{cm}^{-1}$  and 1200-  
212 1600  $\text{cm}^{-1}$  (Supplementary Figure 24), indicating that the skeleton of PCN hardly changes  
213 before and after incorporation of Na and Sb ions (Supplementary Table 3, Supplemental  
214 note 4). All fluoride elements have been removed during the calcination process  
215 (Supplementary Figures 25-26). In the high-resolution C 1s spectrum of pristine PCN  
216 (Figure 2c), the typical components at around 287.6 and 284.6 eV can be indexed as the  
217 C=N and adventitious carbon, respectively. It is important to note that a new nitrogen peak  
218 (N 1s) emerges at 398.1 eV in the spectrum of Sb-SAPC15 (Figure 2d), which can be  
219 assigned to the chemical bond of Sb-N. The binding energy of Sb 3d for Sb-SAPC15 (Sb  
220  $3d_{3/2}$  at 539.5 eV and Sb  $3d_{5/2}$  at 530.2 eV) is close to that for  $\text{Sb}_2\text{O}_3$  (Sb  $3d_{3/2}$  at 539.8 eV  
221 and Sb  $3d_{5/2}$  at 530.5 eV)<sup>41</sup>, indicating that the oxidation state of Sb in Sb-SAPC15 is close  
222 to +3 (Figure 2e).

223 The oxidation state of the Sb atoms in Sb-SAPC15 was further determined by the  
224 position of the absorption edge in the Sb K-edge X-ray absorption near edge structure  
225 (XANES) (Figure 2f). The absorption edge for Sb-SAPC15 is 2.2 eV higher than that for  
226 the  $\text{Sb}^0$  foil, and 1.5 eV lower than that for  $\text{Sb}^{+5}_2\text{O}_5$ , suggesting around +3 valence state of  
227 the Sb atoms in Sb-SAPC15. FT-EXAFS spectrum (Figure 2g) obtained from  $k^3$ -weighted  
228  $k$ -space (Supplementary Figure 27) of Sb-SAPC15 shows only one peak at about 1.53 Å,  
229 and no Sb-Sb bond at 2.71 Å can be detected, implying that the Sb sites in Sb-SAPC15  
230 are atomically dispersed. The coordination structure of the Sb atoms was estimated by  
231 fitting the EXAFS spectrum of Sb-SAPC15 using Artemis (version 0.9.25)<sup>42</sup> (Figure 2h,  
232 Supplementary Table 4) based on the DFT optimization result of the carbon nitride cluster  
233 with single Sb sites (Melem\_3Sb3+, Supplementary Figure 28c). The best fitting result for  
234 the first shell shows that each Sb atom is coordinated with 3.3 N atoms in average and can  
235 be fitted well with the optimized DFT model (Supplementary Figure 28d), further indicating  
236 that the Sb species are atomically dispersed, consistent with the HAADF-STEM results  
237 (Figure 2a and Supplementary Figure 22). It is noteworthy that post-characterizations of

238 Sb-SAPC15 after continuous reaction for 5 days are almost the same as the fresh one  
 239 (Supplementary Figure 29), confirming the excellent stability of Sb-SAPC (Supplementary  
 240 Figure 7, note 5).



241  
 242 **Figure 2 | Characterization of Sb-SAPC.** **a**, High-magnification HAADF-STEM image of Sb-SAPC15.  
 243 Inset is the size distribution of the bright spots. **b**, EELS spectrum of Sb-SAPC15. **c-e**, High-resolution C  
 244 1s (**c**) and N 1s XPS spectra (**d**) of PCN (up) and Sb-SAPC15 (down) and Sb 3d XPS spectrum (**e**) of Sb-  
 245 SAPC15. **f**, Sb-K edge XANES (**f**) and Fourier transform-extended X-ray absorption fine structure (FT-  
 246 EXAFS) spectra (**g**) of the Sb foil, Sb<sub>2</sub>O<sub>5</sub> and Sb-SAPC15. **h**, Fitting of the EXAFS data of the Sb-SAPC15

247 based on the model obtained from DFT optimization. Inserted figures: optimized molecular models based  
248 on DFT for EXAFS fitting.

249

### 250 ***Properties of Sb-SAPC and photocatalytic mechanism***

251 The optical properties and the band diagram of Sb-SAPC were investigated. The  
252 introduction of Sb and Na species slightly narrowed the bandgap (2.77 eV for PCN and  
253 2.63 eV for Sb-SAPC15) and significantly improved the light absorbance (Figure 1c and  
254 Supplementary Figure 30a-b). Confirmed by valence-band XPS and Mott-Schottky  
255 measurements, the introduction of Na and/or Sb species slightly shifted the conduction  
256 band minimum (CBM) from  $\sim$ 1.3 eV (vs. NHE) to  $\sim$ 1.2 eV while rarely influencing the  
257 valence band maximum ( $\sim$ 1.45 eV) (Supplementary Figure 30c-g, Supplementary note 6).

258 The charge separation and recombination process were monitored by steady-state  
259 photoluminescence emission (PL) spectroscopy (Supplementary Figure 31a).<sup>43</sup> The  
260 radiative recombination of excited charge pairs was clearly observed in pristine PCN while  
261 the PL intensity was markedly reduced with addition of Sb and/or Na, indicating that the  
262 radiative recombination was greatly retarded after addition of Sb and/or Na species. This  
263 phenomenon is consistent with the highest photocatalytic activity of Sb-SAPC15. In  
264 addition, the onset of PL wavelength gradually red-shifted, which is also consistent with  
265 the narrowed bandgap. The facilitated charge migration in Sb-SAPC15 could be further  
266 verified by the enhanced photocurrent density (Supplementary Figure 31b) and decreased  
267 electrochemical impedance in the Nyquist plots (Supplementary Figure 31c). It is  
268 noteworthy that the significantly shortened life-time of PL (Supplementary Figure 31d)  
269 could be attributed to the generated deeply trapped sites, which have been proved to  
270 facilitate the ORR process<sup>43,44</sup>.

271 To further investigate whether the deeply trapped sites in Sb-SAPC15 could facilitate  
272 both ORR and OER, time-resolved infrared absorption (TR-IR) spectroscopy was  
273 performed to monitor the charge carrier dynamics and the reactivities of Sb-SAPC15 for  
274 ORR and WOR in microsecond time-scale<sup>43,45</sup>. To probe the charge transfer dynamics from  
275 electron to O<sub>2</sub> and hole to H<sub>2</sub>O, the decay kinetics of deeply trapped electrons (at 5000  
276 cm<sup>-1</sup>) of PCN, PCN\_Na15 and Sb-SAPC15 were investigated (Supplementary Figure 32,

Commented [TB25]: Subheadings must be no longer than 60 characters including spaces and should not contain punctuation.

Perhaps shorten this to "Properties of Sb-SAPC and photocatalytic mechanism" or similar

Commented [TB26R25]: We have changed the subtitle to "Properties of Sb-SAPC and photocatalytic mechanism"

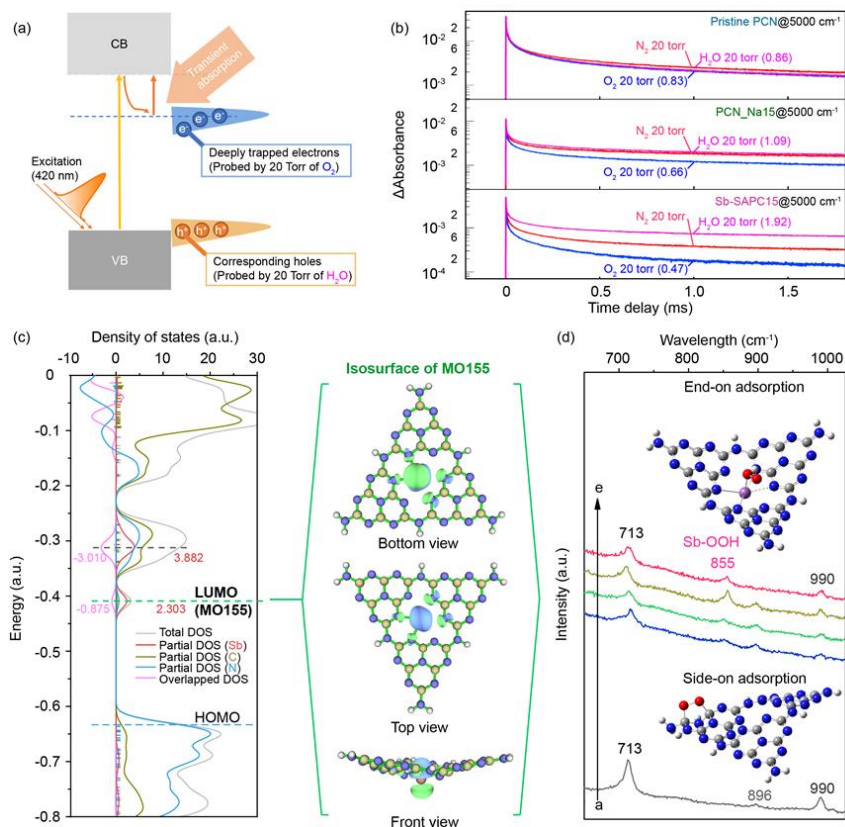
277 [Figure 3a](#)) and compared under N<sub>2</sub>, O<sub>2</sub> and H<sub>2</sub>O atmosphere ([Figure 3b](#)). The decay of the  
278 deeply trapped electrons at 5000 cm<sup>-1</sup> on pristine PCN accelerated very slightly ([Figure](#)  
279 [3b](#)) in O<sub>2</sub> as compared to that in N<sub>2</sub> ( $I_{O_2}/I_{N_2} = 0.83$ ). The decay on PCN\_Na15 showed a  
280 little acceleration in O<sub>2</sub> than that in N<sub>2</sub> ( $I_{O_2}/I_{N_2} = 0.66$ ), indicating that introduction of Na  
281 could generate reactive sites for charge transfer of trapped electrons to O<sub>2</sub><sup>43,44</sup>. When Sb  
282 was introduced into the catalyst, we observed significant decay of the deeply trapped  
283 electrons on Sb-SAPC15 in O<sub>2</sub> as compared to that in N<sub>2</sub> ( $I_{O_2}/I_{N_2} = 0.46$ ). This indicates  
284 that the reactant O<sub>2</sub> would preferentially react with the deeply trapped electrons that were  
285 induced by the Sb sites. In the case of holes, the decay on pristine PCN and PCN\_Na15  
286 changed very little in H<sub>2</sub>O environment compared to that in N<sub>2</sub> ( $I_{H_2O}/I_{N_2} = 0.86$  for PCN and  
287  $I_{H_2O}/I_{N_2} = 1.09$  for PCN\_Na15), indicating that the photogenerated holes barely transferred  
288 to H<sub>2</sub>O. On the contrary, the decay on Sb-SAPC15 was significantly retarded in H<sub>2</sub>O as  
289 compared to that in N<sub>2</sub> ( $I_{H_2O}/I_{N_2} = 1.92$ ), suggesting that the photogenerated holes could  
290 readily transfer to H<sub>2</sub>O molecules: hole-consuming reaction by H<sub>2</sub>O reduced the number of  
291 surviving holes in the catalyst and hence elongated the lifetime of electrons<sup>45</sup>. Additionally,  
292 an isotopic experiment ([Supplementary Figure 33](#)) to simulate the real system (without Ag<sup>+</sup>  
293 or NaIO<sub>3</sub>) was conducted to verify the as-proposed mechanism of WOR by utilizing <sup>16</sup>O<sub>2</sub>  
294 (as an electron acceptor) and H<sub>2</sub><sup>18</sup>O (as an electron donor). As shown in [Supplementary](#)  
295 [Figure 32b](#), the signal of <sup>18</sup>O<sub>2</sub> ( $m/z = 36$ ) could be detected after photocatalytic reaction for  
296 1 h, indicating that the oxygen evolution reaction indeed occurred in the real reaction  
297 system. It is important to note that this signal could not be detected in absence of Sb-  
298 SAPC15 or light irradiation, indicating that the photogenerated holes participated in the  
299 WOR to generate <sup>18</sup>O<sub>2</sub>. The highly active holes for OER could also be confirmed by rotating  
300 ring disk electrode measurements ([Supplementary Figure 34](#)). A clear signal of O<sub>2</sub>  
301 reduction to H<sub>2</sub>O was detected by the ring disk, verifying O<sub>2</sub> generation on the Sb-SAPC  
302 surface via WOR. These results confirm that the deeply trapped electrons and the  
303 corresponding holes in Sb-SAPC15 are the major contributors for the ORR and OER  
304 process ([Supplementary note 7](#)), respectively, leading to a significantly promoted  
305 photocatalytic activity of H<sub>2</sub>O<sub>2</sub> production.

306 The density functional theory (DFT) calculation also shows how the Sb and Na species

307 promote the inner and inter layer charge transfer in Sb-SAPC ([Supplementary Figures 35-](#)  
308 [36](#)). Four periodic models including graphitic carbon nitride (GCN), sodium incorporated  
309 graphitic carbon nitride (Na-GCN), antimony incorporated graphitic carbon nitride (Sb-  
310 GCN), and sodium and antimony co-incorporated graphitic carbon nitride (NaSb-GCN)  
311 were optimized, and the Bader charges of each layer in different models are presented in  
312 [Supplementary Figure 35](#)<sup>43,46</sup>. The Bader charge difference between each adjacent layers  
313 of pristine GCN is extremely small ( $|\Delta q| \sim 0.004 e$ ), suggesting very weak adiabatic  
314 coupling between interlayers in GCN<sup>45,46</sup>, leading to poor interlayer charge transfer. Both  
315 Na-GCN and Sb-GCN display a relatively large number of electrons accumulation on the  
316 2<sup>nd</sup> and 4<sup>th</sup> layer ( $\sim 0.1 e$  of layer charge)<sup>46,47</sup>. As a result, the Na-GCN and Sb-GCN exhibit  
317 a high value of charge difference between the adjacent layers ( $|\Delta q| \sim 0.3 e$ ), indicating that  
318 the adiabatic coupling has been significantly boosted by introducing Na or Sb. The co-  
319 presence of Na and Sb atoms makes the electron distribution more balanced between the  
320 layers ([Supplementary Figure 35](#)). In other words, when both Na and Sb are present in  
321 the carbon nitride structure, the Na-induced and Sb-induced electron density polarization  
322 can be counterbalanced to lower the  $|\Delta q|$  ( $\sim 0.05 e$ ) and at the same time the distance for  
323 adiabatic coupling is significantly increased ( $|\Delta q|$  between the 1<sup>st</sup> and 2<sup>nd</sup> layer and  
324 between the 3<sup>rd</sup> and 4<sup>th</sup> layer are significantly increased). This implies that the charge  
325 transfer between the interlayers in carbon nitride incorporated with Sb and Na atoms is  
326 more facilitated than that in pristine GCN<sup>46,47</sup>. The deformation charge density near surface  
327 of NaSb-GCN ([Supplementary Figure 36](#)) reveals a clear pathway from Na to Sb. The Sb  
328 on the surface of GCN with weak interlayer bridging shows a larger number of electron  
329 accumulation on the first layer ( $-0.0395 e$  of layer charge) than the second layer ( $0.1345$   
330  $e$  of layer charge)<sup>46-50</sup>. Note that a clear electron accumulation region and an electron  
331 depletion region respectively locate at the 1<sup>st</sup> and 2<sup>nd</sup> layer while the pristine CN layer (the  
332 3<sup>rd</sup> layer) can hardly be polarized, indicating that the inner layer charge transfer is  
333 significantly improved with incorporation of Sb and Na species<sup>48-50</sup>. These results show  
334 that the electron transfer can be significantly promoted by the incorporation of Sb and Na  
335 species in GCN, which can explain the higher photocatalytic activities of Sb-SAPC15.

336 The excited properties of Sb-SAPC were further studied by Time Dependent DFT

337 (TDDFT) to understand the correlation between structure and photocatalytic activity using  
338 a mono-layer cluster model<sup>51,52</sup>. The possible simulated excited states (ES) that  
339 contributed to photocatalytic H<sub>2</sub>O<sub>2</sub> production (corresponding to the spectra from 420 nm  
340 to 470 nm) were confirmed by comparing the action spectra (Figure 1c, Supplementary  
341 note 6) with the simulated ones (Supplementary Figure 37a-c). Based on the action spectra  
342 and the photocatalytic H<sub>2</sub>O<sub>2</sub> production activities, the ES1-16 of Melem\_3, the ES 1-15 of  
343 Melem\_3Na+ and the ES 1-26 of Melem\_3Sb3+ are highlighted in the distribution heatmap  
344 of photogenerated electrons and holes (Supplementary Figure 37d-i)<sup>53</sup>. On the one hand,  
345 most of electrons are accumulated at the Sb sites (ES 1-26, Supplementary Table 5), a  
346 ligand-to-metal charge transfer from neighboring melem units to Sb, in Melem\_3Sb3+ with  
347 high density (~20-80%), while most of states (ES 1-16 for Melem\_3, Supplementary Table  
348 6; ES 1-15 for Melem\_3Na+, Supplementary Table 7) show averagely distributed electrons  
349 at the C sites (< 10%) in Melem\_3 and Melem\_3Na+<sup>51-53</sup>. Note that the photogenerated  
350 electrons and holes barely locate at the Na atoms, indicating that the coordinated Na  
351 species on the catalyst's surface could not serve as the active sites for the photocatalytic  
352 reaction. Additionally, a comprehensive investigation of charge separation and  
353 delocalization of holes and electrons were conducted by utilizing Melem\_6, Melem\_6Na+  
354 and Melem\_6Sb3+ as models (Supplementary Figure 38-40, Supplementary note 7). The  
355 significantly improved separation of electron-hole pairs and highly concentrated  
356 electron/holes may effectively promote both photocatalytic ORR and WOR in Sb-SAPC15  
357 by introducing atomic Sb sites.



358

359 **Figure 3 | Excitation properties and OER/ORR reactivities of Sb-SAPC15.** a, The systematic diagram  
 360 of transition absorption after excitation as the probe for OER/ORR (details for the pulse light: 420 nm, 6  
 361 ns, 5 mJ and 0.2 Hz). b, The comparison of transient absorption decay among PCN, PCN\_Na15 and Sb-  
 362 SAPC15 at 5000 cm<sup>-1</sup> under N<sub>2</sub>, O<sub>2</sub> and H<sub>2</sub>O atmosphere (20 Torr). The absorption intensities at the time  
 363 point of 1 ms was used as the benchmark for investigating how deeply trapped electrons/holes interact  
 364 with O<sub>2</sub>/H<sub>2</sub>O. c, Total density of states (TDOS), partial density of states (PDOS) and overlapped density  
 365 of states (ODOS) of Melem\_3Sb3+ combined with the isosurface of LUMO (Isovalue is 0.05). d,  
 366 Experimental Raman spectra recorded during photoreaction in a 2-propanol aqueous solution with  
 367 saturated oxygen. Spectrum a, b, c and d: PCN, Sb-SAPC1, Sb-SAPC5 and Sb-SAPC15 in 10% (v/v) 2-  
 368 propanol aqueous solution. Spectrum e: Sb-SAPC15 in pure water.

369

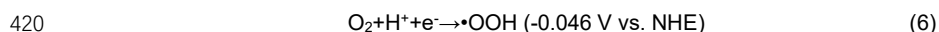
370 The influence of Sb single atoms on the photo-redox reactions was further studied by

371 analyzing the contributions of MOs to holes and electrons from ES1 to ES26 of  
372 Melem\_3Sb3+ (Supplementary Table 5). Several MOs with energetic levels equal to or  
373 lower than HOMO all contribute to holes (ranging from 0% to ~60%), while almost of  
374 electrons are contributed by LUMO (MO155) in most of transitions. This observation  
375 implies that the electronic configuration of LUMO can almost represent the photogenerated  
376 electronic configuration. The result from partial DOS (PDOS) of Melem\_3Sb3+ shows that  
377 a new molecular orbital (MO) mainly contributed by electrons from Sb forms the LUMO. It  
378 is important to note that this MO exhibits a slightly lower energetic level than the MO  
379 contributed by C and N, which is in accordance with the slightly shifted CBM of Sb-  
380 SAPC15<sup>22</sup>. Combined with the simulated results of charge separation, iso-surface of LUMO  
381 of Melem\_3Sb3+ reveals that most of the electrons (>75%) are concentrated at the single  
382 Sb sites with ideal electronic configuration for adsorption of electrophilic oxygen (Figure  
383 3c). To study the ORR mechanism on Sb-SAPC, rotating disk electrode (RDE) analysis  
384 was performed to investigate the number of electrons (n) transferred in the ORR process  
385 (Supplementary Figure 41). The estimated "n" value is close to 2 for Sb-SAPC15 in both  
386 dark and light irradiation conditions. The preferred 2e<sup>-</sup> ORR pathway on Sb-SAPC can be  
387 further supported by DFT calculation using the computational hydrogen electrode (CHE)  
388 method. As shown in Supplementary Figure 42a, the calculated  $\Delta G_{\text{*OOH}}$  is 4.53 eV (U = 0  
389 V versus the reversible hydrogen electrode [RHE]), which is smaller than 4.59 eV of  $\Delta G_{\text{*O}}$ ,  
390 a crucial intermediate in 4e<sup>-</sup> ORR<sup>36</sup>. The large energetic barrier toward forming \*O would  
391 suppress the 4e<sup>-</sup> ORR process. For a 2e<sup>-</sup> ORR catalyst, the adsorption energy of \*OOH  
392 should be larger than the thermoneutral value at the equilibrium potential (U = 0.7 V vs.  
393 RHE), corresponding to  $\Delta G_{\text{*OOH}}$  of 3.52 eV. The calculated  $\Delta G_{\text{*OOH}}$  is 3.83 eV (U = 0.7 V  
394 vs. RHE), suggesting that the ORR on single atom Sb may follow a 2e<sup>-</sup> pathway  
395 (Supplementary Figure 42b). It can be seen that the difference between \*OH and \*O is as  
396 high as 3.742 eV, indicating that a considerably large energetic barrier needs to be  
397 overcome for the 4e<sup>-</sup> OER process. In this case, the Sb site should not function as an  
398 effective site to catalyze 4e<sup>-</sup> OER. It is noteworthy that the calculated  $\Delta G_{\text{*H}}$  on Sb-SAPC15  
399 is significantly larger (0.937 eV) than that on Pt (111) (Supplementary Figure 43),  
400 suggesting that HER on Sb-SAPC15 is energetically unfavorable, matching well with the



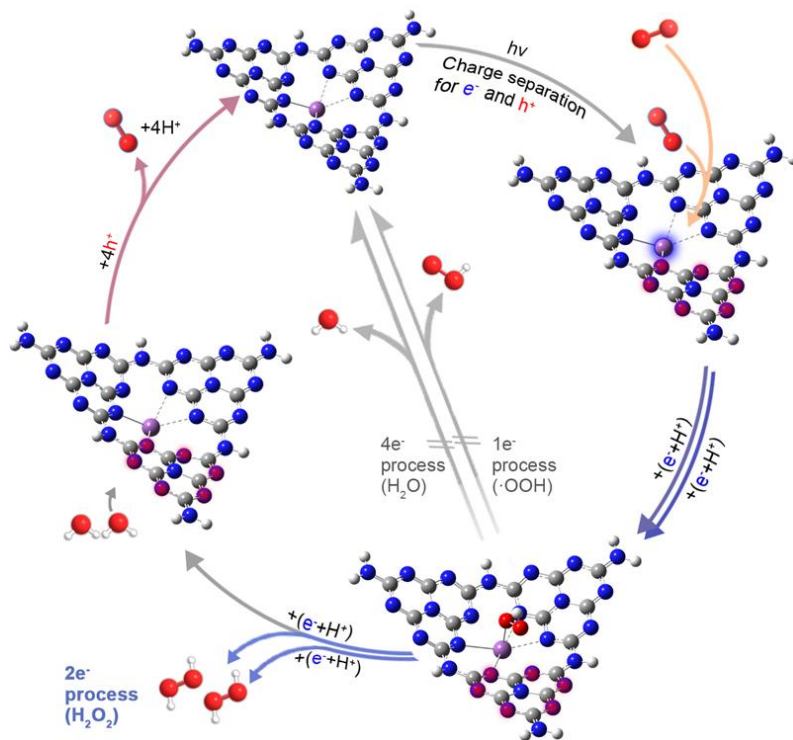
401 experimental result (Figure 1e).

402 To identify the intermediate in the photocatalytic process, Raman spectroscopy  
403 measurements (Figure 3d) were performed under *operando* condition. For PCN, after  
404 reaction with 2-propanol as an electron donor under visible light irradiation, a new band  
405 appears at 896 cm<sup>-1</sup>, which can be assigned to the C–O vibration and O–O stretching on  
406 the melem<sup>12</sup>. While for Sb-SAPCs, a new absorption band at 855 cm<sup>-1</sup> increases with Sb  
407 content in the sample, which can be assigned to the O–O stretching mode of a Sb-OOH  
408 species with end-on adsorption configuration<sup>54,55</sup>. This relative chemical shift between O<sub>2</sub>  
409 end-on/side-on adsorption configuration has been also confirmed by DFT calculations  
410 (Supplementary Figure 44, Supplementary note 8). It is noteworthy that Sb-OOH exists  
411 even without addition of electron donor, implying that formation of Sb-OOH, rather than the  
412 side-on configuration, dominates in the photocatalytic process on Sb-SAPCs. The end-on  
413 adsorption shall significantly suppress the 4e<sup>-</sup> ORR, leading to a high selectivity of the 2e<sup>-</sup>  
414 process<sup>29,30</sup>. Additionally, electron spin resonance (ESR) signal of 5,5-Dimethyl-1-pyrroline  
415 N-oxide-·O<sub>2</sub><sup>-</sup> (DMPO-·O<sub>2</sub><sup>-</sup>) could be hardly observed in the Sb-SAPC system  
416 (Supplementary Figure 45). Since ·O<sub>2</sub><sup>-</sup> is an important intermediate in the stepwise 1e<sup>-</sup>  
417 pathway (Equation 6) during formation of 1-4 endoperoxide, the invisible signal of  
418 DMPO-·O<sub>2</sub><sup>-</sup> in the Sb-SAPC system demonstrates rapid reduction of O<sub>2</sub> on Sb-SAPC to  
419 generate H<sub>2</sub>O<sub>2</sub> via a 2e<sup>-</sup> ORR pathway<sup>22,23,55</sup>.



Commented [TB27]: \* Please do not refer to parts of figures ('top', 'middle', 'left', etc.) in the text.

Commented [TB28R27]: According to the editor's suggestion, we have removed the word "left".



421

422 **Figure 4 | Mechanism of photocatalytic H<sub>2</sub>O<sub>2</sub> production.** (The white, gray, blue, red and magenta  
 423 spheres refer to hydrogen, carbon, nitrogen, oxygen and Sb atoms). After shining visible light, the  
 424 photogenerated electrons are localized at the Sb sites (with blue glow), while the photogenerated holes  
 425 are localized at the N atoms at the melem units (with red glow). Subsequently, the dissolved O<sub>2</sub> molecules  
 426 are adsorbed (orange arrows) onto the Sb sites and then get reduced (blue arrows) via a 2e<sup>-</sup> transfer  
 427 pathway through forming an electron  $\mu$ -peroxide as the intermediate. Simultaneously, water molecules  
 428 are oxidized (pink arrows) to generate O<sub>2</sub> by the highly concentrated holes on the melem units.

429

430 Based on the above characterizations and analyses, the reaction mechanism (Figure 4)  
 431 of Sb-SAPC for photocatalytic H<sub>2</sub>O<sub>2</sub> production is proposed as follows: Firstly, efficient  
 432 charge separation occurred on Sb-SAPC under visible light irradiation, generating  
 433 photoexcited electrons and holes for ORR and WOR, respectively. Then, water molecules  
 434 were oxidized to evolve O<sub>2</sub> by photogenerated holes localized at the N atoms near the  
 435 single Sb atoms. Simultaneously, O<sub>2</sub> dissolved in water and generated from the WOR both

18

**Commented [TB29]:** \* In addition to the title, Figures should also have a brief caption describing the figure. Ideally figures should be understandable without reference to the main text. Please provide this. The color legend must be placed in the caption.

**Commented [TB30R29]:** We have provided a brief caption describing the figure. The color legend has been placed in the caption.

**Commented [TB31]:** \* In keeping with our style, please do not use numbered or bulleted lists.

**Commented [TB32R31]:** We removed the numbered lists. Instead, some conjunctions are used for describing the process.

436 participated in the ORR process to produce H<sub>2</sub>O<sub>2</sub>. It is worthy noting that the efficient  
437 charge separation, ideal single atomic sites for end-on type O<sub>2</sub> adsorption and close spatial  
438 distribution of active sites boost both the 2e<sup>-</sup> ORR and 4e<sup>-</sup> WOR for efficient H<sub>2</sub>O<sub>2</sub>  
439 production.

440

## 441 **Conclusions**

442 In summary, we have reported a well-defined, highly active, selective, and  
443 photochemically robust single Sb atom photocatalyst for non-sacrificial H<sub>2</sub>O<sub>2</sub> production in  
444 a water and oxygen mixture under visible light irradiation. The single Sb sites are able to  
445 accumulate electrons, which act as the photo-reduction sites for O<sub>2</sub> via a 2e<sup>-</sup> ORR pathway.  
446 Simultaneously, the accumulated holes at the N atoms of the melem units neighboring to  
447 the Sb sites accelerate the water oxidation kinetics. The collaborative effect between the  
448 single atom sites and the support shall open up a **vista** for designing various single atom  
449 catalysts for a variety of photocatalytic reactions in energy conversion and environmental  
450 remediation.

451

## 452 **Methods**

### 453 **Preparation of photocatalysts**

454 Unless otherwise stated, the purities of all reagents for photocatalysts preparation and  
455 for photoelectrochemical measurements are above the analytical grade. The pristine PCN  
456 and PCN\_Na15 were prepared according to the reported methods<sup>19</sup>. The Sb-SAPCs were  
457 prepared by a bottom-up method as follows: a certain amount of NaSbF<sub>6</sub> (HuNan HuaJing  
458 Powdery Material Co., LTD, 0.5 mmol, 1 mmol, 3 mmol, 5 mmol, 10 mmol, 15 mmol and  
459 20 mmol) was dissolved in 30 mL ethanol under sonication for 60 min at 60 °C, followed  
460 by adding 4 g melamine (Wako Pure Chemical Industries, Ltd.). The solvent in the solution  
461 was removed by combination of rotatory evaporator and vacuum oven. The as-obtained  
462 white powder was transferred into a tube furnace. To ensure that oxygen was not present  
463 during thermal treatment, the tube furnace was firstly vacuumed to <1 Torr before switching  
464 on the N<sub>2</sub> gas flow. This process was repeated 3 times, and then 50 mL min<sup>-1</sup> N<sub>2</sub> gas flow  
465 was maintained for 30 min before heat treatment. During the synthesis process (including

**Commented [TB33]:** \* We avoid the use of phrases such as 'novel', 'for the first time', 'unprecedented', etc. The novelty should be clear from the context. Please rephrase

**Commented [TB34R33]:** We believe the novelty has been presented already by proposing the collaborative effects between the single atom sites and supports. Therefore, we have change the word "new direction" to "vista".

**Commented [TB35]:** We have chaged the phrase "Experimental section " into "Methods".

**Commented [TB36R35]:** This section subheading has been shortened to be no longer than 60 characters (including spaces).

**Commented [TB37]:** Please remove this part. the Methods section can be up to 3000 words, so please incorporate as much of the Supplementary Information into the main paper as possible.

**Commented [TB38R37]:** We have incorporated as much of the Supplementary Information into the main paper as possible.

466 heating and cooling), the system was pressurized by N<sub>2</sub> flow so that oxygen could hardly  
467 influence the synthesis. The temperature of the furnace was increased from 25 °C to  
468 560 °C at a ramp rate of 2 °C min<sup>-1</sup> in N<sub>2</sub> atmosphere then kept at 560 °C for 4 h. After heat  
469 treatment, the furnace was cooled down naturally to 25 °C lasting for at least 8 h with  
470 continuous N<sub>2</sub> flowing.

471

#### 472 **Photocatalytic reaction toward H<sub>2</sub>O<sub>2</sub> production**

473 100 mg of photocatalyst was added to 50 mL of deionized water in a borosilicate glass  
474 bottle (φ: 60 mm; capacity: 100 mL), and the bottle was sealed with a rubber septum cap.  
475 The catalyst was dispersed by ultrasonication for 15 min, and O<sub>2</sub> was bubbled through the  
476 solution for 30 min. The bottle was kept in a temperature-controlled air bath at 25 ± 0.5 °C  
477 with wind flow and was irradiated at λ > 420 nm using a 300 W Xe lamp (PXE-500, USHIO  
478 Inc.) under magnetic stirring. To study the WOR, 50 mg of photocatalyst was added into  
479 NaIO<sub>3</sub> (0.1 M, 50 mL) solution in a borosilicate glass bottle (φ: 60 mm; capacity: 100 mL).  
480 After completely removing O<sub>2</sub> from the reaction system, the bottle was irradiated by a 300  
481 W Xenon Lamp. The light intensity of visible light and infrared-red light (I<sub>>400</sub>) after passing  
482 a UV cut filter (λ > 400 nm) was firstly measured. Then, a glass filter with λ > 500 nm was  
483 used to replace the UV cut filter for measuring the light intensity (I<sub>>500</sub>). The difference  
484 between I<sub>>400</sub> and I<sub>>500</sub> was used to calibrate the total light intensity. After a certain time  
485 interval, the gas was extracted from the bottle and examined by gas chromatography  
486 equipped with a TCD detector. To examine the H<sub>2</sub>O<sub>2</sub> production from O<sub>2</sub> generated by WOR,  
487 a certain amount of photocatalyst (Sb-SAPC15: 200 mg, 100 mg and 50 mg; Pristine PCN:  
488 200 mg) was added into 50 mL of NaNO<sub>3</sub> solution (pH = 7) with AgNO<sub>3</sub> (0.1 mM). 1.5 mL  
489 of solution was extracted every hour to acquire the time-dependent H<sub>2</sub>O<sub>2</sub> production  
490 without the initial introduction of O<sub>2</sub>. The amount of H<sub>2</sub>O<sub>2</sub> in these experiments was  
491 determined by a colorimetric method using PACKTEST (WAK-H<sub>2</sub>O<sub>2</sub>, KYORITSU  
492 CHEMICAL-CHECK Lab., Corp.) equipped with a digital PACKTEST spectrometer (ED723,  
493 GL Sciences Inc.).

494

#### 495 **Apparent quantum efficiency analysis**

496 The photocatalytic reaction was carried out in pure deionized water (30 mL) with  
497 photocatalyst (60 mg) with or without addition of ethanol as an electron donor in a  
498 borosilicate glass bottle. After ultrasonication and O<sub>2</sub> bubbling, the bottle was irradiated by  
499 an Xe lamp for 4 h with magnetic stirring. The incident light was monochromated by band-  
500 pass glass filters (Asahi Techno Glass Co.), where the full-width at half-maximum of the  
501 light is 11–16 nm. The number of photons that enter the reaction vessel was determined  
502 by a 3684 optical power meter (HIOKI E.E. CORPORATION).

503

#### 504 **Determination of solar-to-chemical conversion efficiency**

505 Solar-to-chemical conversion efficiency was determined by a PEC-L01 solar simulator  
506 (Pecell Technologies, Inc.). The photoreaction was performed in pure deionized water  
507 (100 mL) with photocatalyst (500 mg) under O<sub>2</sub> atmosphere (1 atm) in a borosilicate glass  
508 bottle. A UV cut filter ( $\lambda > 420$  nm) was used to avoid decomposition of the formed H<sub>2</sub>O<sub>2</sub> by  
509 absorbing UV light<sup>12,16,23</sup>. The irradiance of the solar simulator was adjusted to the AM1.5  
510 global spectrum<sup>12,16,23</sup>. The solar-to-chemical conversion efficiency ( $\eta$ ) was calculated by  
511 the following equation:

$$512 \quad \eta(\%) = \frac{\Delta G_{H_2O_2} \times n_{H_2O_2}}{t_{ir} \times S_{ir} \times I_{AM}} \times 100\%.$$

513 where  $\Delta G_{H_2O_2}$  is the free energy for H<sub>2</sub>O<sub>2</sub> generation (117 kJ mol<sup>-1</sup>).  $n_{H_2O_2}$  is the amount  
514 of H<sub>2</sub>O<sub>2</sub> generated, and  $t_{ir}$  is the irradiation time (s). The overall irradiation intensity ( $I_{AM}$ )  
515 of the AM1.5 global spectrum (300–2500 nm) is 1000 W m<sup>-2</sup>, and the irradiation area ( $S_{ir}$ )  
516 is  $3.14 \times 10^{-4}$  m<sup>2</sup>.

517

#### 518 **Instruments**

519 High-resolution transmission electron microscopy, high-angle annular dark field  
520 scanning transmission electron microscopy, selected area electron diffraction and energy-  
521 dispersive X-ray spectroscopy were performed on a Titan Cubed Themis G2 300 electron  
522 microscope with an accelerating voltage of 300 kV. Electron energy loss spectroscopy was  
523 conducted using a Quantum ER/965 P detector. The crystalline phases were characterized  
524 by a powder X-ray diffraction instrument (MiniFlex II, Rigaku Co.) with CuK $\alpha$  ( $\lambda = 1.5418$

(6)

Commented [TB39]: Please name this section as "Methods"

Commented [TB40R39]: We have added the number of the equation presented here.

525 Å) radiation (cathode voltage: 30 kV, current: 15 mA). Absorption properties of the powder  
526 samples were determined using the diffuse reflection method on a UV/VIS/NIR  
527 spectrometer (UV-2600, Shimadzu Co.) attached to an integral sphere at room  
528 temperature. X-ray photoelectron spectroscopy measurements were performed on a  
529 Kratos AXIS Nova spectrometer (Shimadzu Co., Japan) with a monochromatic Al K $\alpha$  X-ray  
530 source. The binding energy was calibrated by taking the carbon (C) 1s peak of adventitious  
531 carbon at 284.6 eV. Valence band X-ray photoelectron spectroscopy was performed on an  
532 ESCALAB 250Xi (Thermo Scientific, USA). The equilibration of Fermi level of the  
533 instrument was performed by measuring the VB-XPS of Au metal basis as the reference.  
534 The Fermi level of the instrument was equilibrated at 4.5 eV. In this case, the numerical  
535 value of the binding energy in the calibrated VB-XPS spectrum is the same as the potential  
536 vs. standard hydrogen electrode. Electron spin resonance signals of spin-trapped  
537 paramagnetic species with 5,5-dimethyl-1-pyrroline N-oxide (DMPO, methanol solution)  
538 were recorded with an A300-10/12 spectrometer. Photoluminescence spectroscopy was  
539 performed on a FP-8500 spectrofluorometer (JASCO Corporation, Japan). The  
540 temperature for the photoluminescence measurements was about 25 °C controlled by an  
541 air conditioner, which worked 24/7. Time-dependent photoluminescence spectroscopy was  
542 conducted on a FS5 fluorescence spectrometer (Edinburgh Instruments Ltd., UK). Raman  
543 spectra was performed on a Laser Microscopic Confocal Raman Spectrometer (Renishaw  
544 inVia, UK) at 785 nm. The pH value of the solution was measured by a pH meter (HORIBA  
545 pH meter D-51, HORIBA, Ltd.).

546 The X-ray absorption spectroscopy for Sb K-edge was measured at beamline BL01C  
547 at the National Synchrotron Radiation Research Center (NSRRC, Hsinchu, Taiwan). The  
548 data analysis for the X-ray absorption spectroscopy using IFEFFIT was conducted by  
549 Demeter system.

550

#### 551 **Photoelectrochemical characterizations**

552 Photoelectrochemical (PEC) characterizations were conducted on a conventional three-  
553 electrode potentiostat setup connected to an electrochemical analyzer (Model 604D, CH  
554 Instruments, Inc.). The fluorine-doped tin oxide (FTO) glass of 1 cm  $\times$  2 cm in size was

555 covered with photocatalyst that was achieved by first mixing a catalyst (100 mg) with ethyl  
556 cellulose binder (10 mg) in ethanol (6 mL) for one hour and then depositing the final viscous  
557 mixture by a doctor blade method followed by drying at room temperature and further  
558 drying at 40 °C overnight in a vacuum oven. The area of the photoelectrode was controlled  
559 to be 1 cm<sup>2</sup>. The PEC system consisted of an FTO glass covered by the photocatalyst, a  
560 coiled Pt wire and a saturated Ag/AgCl/KCl (saturated) electrode as the working, counter,  
561 and reference electrode, respectively. The photocurrent was collected at 0.8 V vs. NHE  
562 (0.6 V vs. Ag/AgCl) in a phosphate buffer solution (PBS, pH = 7.4). The solution was  
563 saturated with O<sub>2</sub> by bubbling O<sub>2</sub> for 15 min (0.5 L min<sup>-1</sup>)<sup>12,56,57</sup>. Electrochemical impedance  
564 spectroscopy (EIS) analysis was performed at a DC voltage of -0.6 V vs. Ag/AgCl with an  
565 AC voltage amplitude of 5 mV in a frequency range from 100 kHz to 0.01 Hz. For the Mott-  
566 Schottky measurements, similar strategy was performed on FTO glass (1.5 cm × 3 cm) by  
567 the same doctor blade method. The area of the electrode for the Mott-Schottky  
568 measurements was controlled to be 0.50 cm<sup>2</sup>. Mott-Schottky measurements were  
569 performed at a potential range from 0.2 V to -0.6 V vs. NHE, with an AC voltage amplitude  
570 of 5 mV, and in a frequency range from 25 Hz to 500 Hz. Each increase of potential is 0.05  
571 V. The quiet time for each test is 2 s.

572

#### 573 **Isotopic experiments with <sup>18</sup>O<sub>2</sub> and H<sub>2</sub><sup>16</sup>O**

574 Firstly, 60 mg of Sb-SAPC15 was dispersed in 30 ml of H<sub>2</sub><sup>16</sup>O via sonication for 15 min.  
575 Subsequently, 10 mL of <sup>18</sup>O<sub>2</sub> gas (≥ 98% <sup>18</sup>O; TAIYO NIPPON SANSO Corporation) was  
576 injected to the suspension. Then, the system was completely sealed and irradiated by  
577 visible light. After a certain time interval (6 h, 24 h, and 72 h), 1 mL suspension was  
578 extracted and injected into a glass test tube filled with N<sub>2</sub> and 0.1 g Fe<sub>2</sub>(SO<sub>4</sub>)<sub>3</sub> dissolved in  
579 1 mL H<sub>2</sub>SO<sub>4</sub>. After injection of suspension, the test tube was sealed and irradiated under  
580 UV light for 5 h. The gas (0.1 mL) in the test tube was extracted by gas chromatography  
581 syringe and injected into a Shimadzu GC-MS system (GCMS-QP2010).

582

#### 583 **Isotopic experiments with H<sub>2</sub><sup>18</sup>O**

584 20 mg of Sb-SAPC15 was dispersed in 10 g of H<sub>2</sub><sup>18</sup>O (≥ 98% <sup>18</sup>O; TAIYO NIPPON

585 SANSO Corporation) containing 1 mM AgNO<sub>3</sub> under sonication for 15 min. Afterwards, N<sub>2</sub>  
586 was bubbled into the suspension for 2 h at a flow rate of 0.5 L min<sup>-1</sup> to ensure complete  
587 removal of the dissolved oxygen (<sup>16</sup>O<sub>2</sub>) in the system<sup>16</sup>. Then, the system was completely  
588 sealed and irradiated by visible light. After a certain time interval (0.5 h, 1 h, 3 h, 5 h, 10 h  
589 and 24 h), 1 mL suspension was extracted and injected into a glass test tube filled with N<sub>2</sub>  
590 and 0.1 g Fe<sub>2</sub>(SO<sub>4</sub>)<sub>3</sub> dissolved in 1 mL H<sub>2</sub>SO<sub>4</sub>. After injection of suspension, the test tube  
591 was sealed and irradiated under UV light for 5 h. The gas (0.1 mL) in the test tube was  
592 extracted by gas chromatography syringe and injected into a Shimadzu GC-MS system  
593 (GCMS-QP2010).

594

#### 595 **Isotopic experiments in real experimental conditions**

596 A poly tetra fluoroethylene gas bag was used for the isotopic experiment. First of all, 3  
597 mL ultrapure N<sub>2</sub> was injected into the bag, followed by injecting 1 mL aqueous suspension  
598 of Sb-SAPC15 (concentration: 1 mg mL<sup>-1</sup>; 1 mg Sb-SAPC15 powder dissolved in 1 mL  
599 H<sub>2</sub><sup>18</sup>O). Subsequently, 100 µL O<sub>2</sub> gas was injected and the bag was properly sealed and  
600 put over an ultrasonicator. Additionally, control experiments in absence of Sb-SAPC15 or  
601 light irradiation were conducted for confirming the photo-induced oxygen generation  
602 reaction. Furthermore, GC-MS spectra of the gas extracted from the Sb-SAPC15 system  
603 with other electron acceptors (0.1 M Ag<sup>+</sup> or 0.1 M NaIO<sub>3</sub>) or without addition of Sb-SAPC  
604 were also conducted for comparison.

605

#### 606 **H<sub>2</sub>O<sub>2</sub> degradation study**

607 50 mL of deionized water in a borosilicate glass bottle (φ: 60 mm; capacity: 100 mL)  
608 without addition of catalyst was bubbled with O<sub>2</sub> for 30 min. Then, a certain amount of H<sub>2</sub>O<sub>2</sub>  
609 was added into the bottle, and the concentration of H<sub>2</sub>O<sub>2</sub> was manipulated to be 1 × 10<sup>2</sup> mg  
610 L<sup>-1</sup>. Finally, the bottle was sealed with a rubber septum cap. To investigate the hole transfer  
611 to H<sub>2</sub>O<sub>2</sub>, the following experiment was performed: 50 mg of photocatalyst was added into  
612 50 mL NaIO<sub>3</sub> (0.1 M) and H<sub>2</sub>O<sub>2</sub> (0.01wt.%) solution in a borosilicate glass bottle (φ: 60 mm;  
613 capacity: 100 mL). The same solution without addition of photocatalyst was also measured  
614 as a control. Additionally, the same experiment was also conducted in 50 mL NaIO<sub>3</sub> (0.1

Commented [TB41]: Subheadings must be no longer than 60 characters including spaces and should not contain punctuation.

Commented [TB42R41]: This section subheading has been shortened to be no longer than 60 characters (including spaces).



615 M) phosphate buffer solution (0.1 M, pH = 7.4). After completely removing O<sub>2</sub> from the  
616 reaction system, the bottle was irradiated by a 300 W Xenon lamp with a UV cut filter (light  
617 intensity: 30.3 W m<sup>-2</sup> at 420-500 nm).

618

#### 619 **Details for TD-DFT calculations**

620 The optimization and frequency combined with the vertical excitation properties were  
621 performed via time-dependent density functional theory (TD-DFT) in the Gaussian 09  
622 program S2, which was carried out by utilizing wb97xd/6-311g(d) level of theory for C, N  
623 and H elements and SDD for Sb element. 3 monolayer cluster models were optimized to  
624 represent the major surface properties of CN sites in PCN, Na sites in PCN\_Na15 and Sb  
625 sites in Sb-SAPC15<sup>50,58</sup>. The charges of monolayer cluster models were settled in  
626 consideration of the oxidation state of Sb and Na based on the experimental results as  
627 follows: 0 for Melem\_3; +1 for Melem\_Na1+; and +3 for Melem\_3Sb3+. To give a  
628 comprehensive understanding of the relationships between the electronic configuration  
629 during excitation and the realistic experiment results. 50 excited states (ES) of these three  
630 cluster models have been used to simulate of UV absorption spectra<sup>50</sup>. Note that the  
631 absorption edge of simulated UV spectra is usually large than that of experimental ones  
632 because of the following two reasons: (1) To simulate the charge-transfer properties of the  
633 model with high qualities, function of ω97xd, a function including large amount of Hartree–  
634 Fock exchange, were used. These exchange functions usually overestimate the excitation  
635 energies, as well as the simulated HOMO-LUMO gap<sup>51,52,58</sup>; (2) In the solid state, p-  
636 conjugated molecules adjacent to the one carrying a charge do strongly polarize, an effect  
637 that stabilizes the cationic and anionic states (each generally by about one eV in p-  
638 conjugated materials). In this case, the band gap is typically considerably smaller in energy  
639 than the molecular fundamental gap, as well as the optical gap<sup>52</sup>. Since the evitable system  
640 error cannot be eliminated, the possible simulated ES that contributed to H<sub>2</sub>O<sub>2</sub> production  
641 (corresponding to the spectra from 420 nm – 470 nm) was confirmed by comparing the  
642 experimental spectra and simulated ones. Then, the transition density of electron/holes  
643 were considered at all these ES.

644 For analysis of the excitation and charge transfer properties, Multiwfn Ver. 3.6 (released

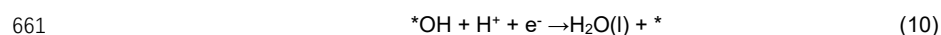
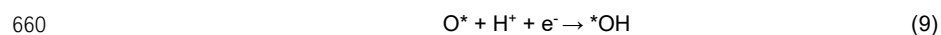
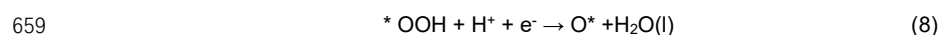
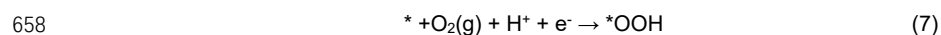
645 on May 21, 2019)<sup>53</sup> was performed. Visualization of hole, electron and transition density  
646 was also performed by Multiwfn; functions of  $IOP(9/40 = 3)$  were set during the vertical  
647 excitation based on TD-DFT calculation<sup>53</sup>. The electron distributions at these ES were  
648 presented as heatmaps by combination of GaussView and Multiwfn<sup>53,59-62</sup>. The iso surface  
649 of LUMO orbitals were presented by setting the isovalue of 0.05.

650

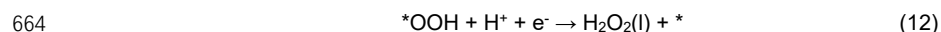
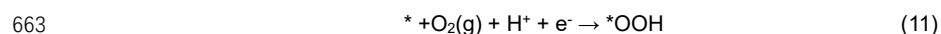
### 651 **Details for Free energy diagram**

652 The cluster model is more likely to predict the ORR process based on our previous  
653 investigation<sup>36</sup>. The free energy diagram of Melem\_3Sb3+ was calculated as follows:

654 The optimized structure of Melem\_3Sb3+ was used as the initial structure for calculating  
655 the most stable adsorption configurations of \*OOH, \*O, and \*OH. The ORR following the  
656 2e<sup>-</sup> and 4e<sup>-</sup> pathway produces H<sub>2</sub>O and H<sub>2</sub>O<sub>2</sub>, respectively. The associative 4e<sup>-</sup> ORR is  
657 composed of four elementary steps (Equation 7-10):



662 The 2e<sup>-</sup> ORR comprises of two elementary steps (Equation 11-12):



665 The asterisk (\*) denotes the active site of the catalyst.

666 The free energy for each reaction intermediate is defined as:

$$667 \quad G = E_{\text{DFT}} + E_{\text{ZPE}} - TS + E_{\text{sol}} \quad (13)$$

668 where  $E_{\text{DFT}}$  is the electronic energy calculated by DFT,  $E_{\text{ZPE}}$  denotes the zero point energy  
669 estimated within the harmonic approximation, and TS is the entropy at 298.15 K ( $T =$   
670 298.15 K). The  $E_{\text{ZPE}}$  and TS of gas-phase H<sub>2</sub> and reaction intermediates are based on our  
671 previous work<sup>36</sup>. For the concerted proton-electron transfer, the free energy of a pair of  
672 proton and electron ( $\text{H}^+ + \text{e}^-$ ) was calculated as a function of applied potential relative to  
673 RHE (U versus RHE), i.e.,  $\mu(\text{H}^+) + \mu(\text{e}^-) = 1/2\mu(\text{H}_2) - eU$ , according to the computational  
674 hydrogen electrode (CHE) model proposed by Nørskov.<sup>63</sup> In addition, the solvent effect

675 was reported to play an important role in ORR. In our calculations, the solvent corrections  
676 ( $E_{\text{sol}}$ ) for \*OOH and \*OH are 0.45 eV in accordance with previous studies<sup>64,65</sup>. We used the  
677 energies of H<sub>2</sub>O and H<sub>2</sub> molecules calculated by DFT together with experimental formation  
678 energy of H<sub>2</sub>O (4.92 eV) to construct the free energy diagram. The free energies of O<sub>2</sub>,  
679 \*OOH, \*O, and \*OH at a given potential U relative to RHE are defined as:

$$680 \quad \Delta G(O_2) = 4.92 - 4eU \quad (14)$$

$$681 \quad \Delta G(OOH) = G(*OOH) + \frac{3G(H_2)}{2} - G(*) - 2G(H_2O) - 3eU \quad (15)$$

$$682 \quad \Delta G(O) = G(*O) + G(H_2) - G(*) - G(H_2O) - 2eU \quad (16)$$

$$683 \quad \Delta G(OH) = G(*OH) + \frac{G(H_2)}{2} - G(*) - G(H_2O) - eU \quad (17)$$

684

#### 685 **Details for simulations of charge transfer**

686 All theoretical calculations were performed based on density functional theory (DFT),  
687 implemented in the Vienna ab initio simulation package (VASP)<sup>66,67</sup>. The electron exchange  
688 and correlation energy were treated within the generalized gradient approximation in the  
689 Perdew-Burke-Ernzerhof functional (GGA-PBE)<sup>68,69</sup>. The valence orbitals were described  
690 by plane-wave basis sets with cutoff energies of 400 eV. For the simulation of Na and Sb  
691 incorporated in bulk phase of g-C<sub>3</sub>N<sub>4</sub>, a 1 × 1 × 2 supercell of pristine bulk g-C<sub>3</sub>N<sub>4</sub> was  
692 adopted. And the k-points were sampled in a 3 × 3 × 2 Monkhorst-Pack grid. For the  
693 simulation of Na and Sb near the surface of g-C<sub>3</sub>N<sub>4</sub>, the k-point sampling was obtained  
694 from the Monkhorst-Pack scheme with a (2 × 2 × 1) mesh. The atomic coordinates are fully  
695 relaxed using the conjugate gradient method (CG)<sup>70</sup>. The convergence criteria for the  
696 electronic self-consistent iteration and force were set to 10<sup>-4</sup> eV and 0.02 eV/Å, respectively.  
697 The vacuum gap was set as 15 Å. To quantitatively compare the degree of charge transfer,  
698 a Bader charge analysis has been carried out<sup>45</sup>.

699

#### 700 **Data availability**

701 The data that support the findings of this study are available from the corresponding author  
702 upon reasonable request. [Source data](#) are provided with this paper.

703

**Commented [TB43]:** Please add a 'Data availability' section at the end of the Methods

This journal strongly supports public availability of all data: we encourage you to make arrangements, wherever possible, to place the data used in your paper into a public data repository. If data can only be shared on request, we ask that you explain why in your Data Availability Statement.

**Commented [TB44R43]:** We have added the "data availability part" here. The source data of this paper will be uploaded in several separated files.

704 **Code availability**

705 The codes that support the findings of this study are available from the corresponding  
706 author upon reasonable request.

707

708 **References**

- 709 [1] Bryliakov, K.P. Catalytic asymmetric oxygenations with the environmentally benign oxidants  
710 H<sub>2</sub>O<sub>2</sub> and O<sub>2</sub>, *Chem. Rev.* **117**, 11406-11459 (2017).
- 711 [2] Shaegh, S.A.M., Nguyen, N.-T., Ehteshamiab, S.M.M. & Chan, S.H., A membraneless  
712 hydrogen peroxide fuel cell using Prussian Blue as cathode material, *Energy Environ. Sci.* **5**,  
713 8225-8228 (2012).
- 714 [3] Gray, H.B. Powering the planet with solar fuel, *Nat. Chem.* **1**, (2009) 7-7.
- 715 [4] Kim, D., Sakimoto, K.K., Hong, D. & Yang, P. Artificial photosynthesis for sustainable fuel  
716 and chemical production, *Angew. Chem. Int. Ed.* **54**, 3259-3266 (2015).
- 717 [5] Xia, C., Xia, Y., Zhu, P., L. Fan & Wang, H. Direct electrosynthesis of pure aqueous H<sub>2</sub>O<sub>2</sub>  
718 solutions up to 20% by weight using a solid electrolyte, *Science* **366**, 226-231 (2019).
- 719 [6] Edwards, J.K. *et al.* Direct synthesis of H<sub>2</sub>O<sub>2</sub> from H<sub>2</sub> and O<sub>2</sub> over gold, palladium, and gold-  
720 palladium catalysts supported on acid-pretreated TiO<sub>2</sub>, *Angew. Chem. Int. Ed.* **48**, 8512–8515  
721 (2009).
- 722 [7] Freakley, S.J. *et al.* Palladium-tin catalysts for the direct synthesis of H<sub>2</sub>O<sub>2</sub> with high selectivity,  
723 *Science* **351**, 965-968 (2016).
- 724 [8] Yang, S. *et al.* Toward the decentralized electrochemical production of H<sub>2</sub>O<sub>2</sub>: A focus on the  
725 catalysis, *ACS Catal.* **8**, 4064-4081 (2018).
- 726 [9] Yi, Y., Wang, L., Li, G. & Guo, H. A review on research progress in the direct synthesis of  
727 hydrogen peroxide from hydrogen and oxygen: Noble-metal catalytic method, fuel-cell method  
728 and plasma method, *Catal. Sci. Technol.* **6**, 1593-1610 (2016).
- 729 [10] Hou, H., Zeng & X. Zhang, X. Production of hydrogen peroxide through photocatalytic process:  
730 A critical review of recent advances, *Angew. Chem. Int. Ed.*, (2019).
- 731 [11] Shi, X. *et al.* Understanding activity trends in electrochemical water oxidation to form  
732 hydrogen peroxide, *Nat. Commun.* **8**, 701 (2017).
- 733 [12] Shiraishi, Y. *et al.* Sunlight-driven hydrogen peroxide production from water and molecular  
734 oxygen by metal-free photocatalysts, *Angew. Chem.* **126**, 13672-13677 (2014).
- 735 [13] Fuku, K. & Sayama, K. Efficient oxidative hydrogen peroxide production and accumulation in  
736 photoelectrochemical water splitting using a tungsten trioxide/bismuth vanadate photoanode,  
737 *Chem. Commun.* **52**, 5406-5409 (2016).
- 738 [14] Baek, J.H. *et al.* Selective and efficient Gd-doped BiVO<sub>4</sub> photoanode for two-electron water  
739 oxidation to H<sub>2</sub>O<sub>2</sub>, *ACS Energy Lett.* **4**, 720-728 (2019).
- 740 [15] Teng, *et al.* Photoexcited single metal atom catalysts for heterogeneous photocatalytic H<sub>2</sub>O<sub>2</sub>  
741 production: Pragmatic guidelines for predicting charge separation, *Appl. Catal. B-Environ.*  
742 **282**, 119589 (2020).
- 743 [16] Shiraishi, Y. *et al.* Resorcinol–formaldehyde resins as metal-free semiconductor photocatalysts  
744 for solar-to-hydrogen peroxide energy conversion, *Nat. Mater.* **18**, 985-993 (2019).
- 745 [17] Fan, W. *et al.* Efficient hydrogen peroxide synthesis by metal-free polyterthiophene via

**Commented [TB45]:** All authors should be included in reference lists unless there are more than five, in which case only the first author should be given, followed by 'et al.'.

Authors should be listed last name first, followed by a comma and initials of given names. There should be no spaces between initials. Article titles should be in Roman text and book titles in italics; the first word of the title is capitalized, the title written exactly as it appears in the work cited, ending with a period. Journal names are italicized and abbreviated (with periods) according to common usage. Volume numbers appear in bold. Please correct the format of your references as necessary.

All authors should be included in reference lists unless there are more than five, in which case only the first author should be given, followed by 'et al.'.

Authors should be listed last name first, followed by a comma and initials of given names. There should be no spaces between initials. Article titles should be in Roman text and book titles in italics; the first word of the title is capitalized, the title written exactly as it appears in the work cited, ending with a period. Journal names are italicized and abbreviated (with periods) according to common usage. Volume numbers appear in bold. Please correct the format of your references as necessary.

DOIs are not included.

**Commented [TB46R45]:** We have revised the formats of references by following the editor's suggestion.

- 746 photoelectrocatalytic dioxygen reduction, *Energy Environ. Sci.* **13**, 238-245 (2020).
- 747 [18] Kim, H., Choi, Y., Hu, S., Choi, W. & Kim, J.-H. Photocatalytic hydrogen peroxide production  
748 by anthraquinone-augmented polymeric carbon nitride, *Appl. Catal. B-Environ.* **229**, 121-129  
749 (2018).
- 750 [19] Moon, G.-H. *et al.* Eco-friendly photochemical production of H<sub>2</sub>O<sub>2</sub> through O<sub>2</sub> reduction over  
751 carbon nitride frameworks incorporated with multiple heteroelements, *ACS Catal.* **7**, 2886-  
752 2895 (2017).
- 753 [20] Chu, C. *et al.* Spatially separating redox centers on 2D carbon nitride with cobalt single atom  
754 for photocatalytic H<sub>2</sub>O<sub>2</sub> production, *PNAS* **117**, 6376-6382 (2020).
- 755 [21] Wei, Z. *et al.* Efficient visible-light-driven selective oxygen reduction to hydrogen peroxide by  
756 oxygen-enriched graphitic carbon nitride polymer, *Energy Environ. Sci.* **11**, 2581-2589 (2018).
- 757 [22] Kaynan, N., Berke, B.A., Hazut, O. & Yerushalmi, R. Sustainable photocatalytic production of  
758 hydrogen peroxide from water and molecular oxygen, *J. Mater. Chem. A* **2**, 13822-13826  
759 (2014).
- 760 [23] Teng, Z. *et al.* Bandgap engineering of polymeric carbon nitride copolymerized by 2,5,8-  
761 triamino-tri-s-triazine (melem) and barbituric acid for efficient nonsacrificial photocatalytic  
762 H<sub>2</sub>O<sub>2</sub> production. *Appl. Catal. B* **271**, 118917 (2020).
- 763 [24] Zeng, X. *et al.* Simultaneously tuning charge separation and oxygen reduction pathway on  
764 graphitic carbon nitride by polyethylenimine for boosted photocatalytic hydrogen peroxide  
765 production, *ACS Catal.* **10**, 3697-3706 (2020).
- 766 [25] Wang, Q. & Domen, K., Particulate photocatalysts for light-driven water splitting: Mechanisms,  
767 challenges, and design strategies, *Chem. Rev.* **120**, 919-985 (2020).
- 768 [26] Hirakawa, H., Hashimoto, M., Shiraishi, Y. & Hirai, T. Photocatalytic conversion of nitrogen  
769 to ammonia with water on surface oxygen vacancies of titanium dioxide photocatalytic  
770 conversion of nitrogen to ammonia with water on surface oxygen vacancies of titanium dioxide,  
771 *J. Am. Chem. Soc.* **139**, 10929-10936 (2017).
- 772 [27] Kulkarni, A., Siahrostami, S., Patel, A. & Nørskov, J.K. Understanding catalytic activity trends  
773 in the oxygen reduction reaction, *Chem. Rev.* **118**, 2302-2312 (2018).
- 774 [28] Watanabe, E., Ushiyama, H. & Yamashita, K., Theoretical studies on the mechanism of oxygen  
775 reduction reaction on clean and O-substituted Ta<sub>3</sub>N<sub>5</sub>(100) surfaces. *Catal. Sci. Technol.* **5**,  
776 2769-2776 (2015).
- 777 [29] Choi, C.H. *et al.* Hydrogen peroxide synthesis via enhanced two-electron oxygen reduction  
778 pathway on carbon-coated Pt surface. *J. Phys. Chem. C* **118**, 30063-30070 (2014).
- 779 [30] Chu, C. *et al.*, Electronic tuning of metal nanoparticles for highly efficient photocatalytic  
780 hydrogen peroxide production. *ACS Catal.* **9**, 626-631 (2019).
- 781 [31] Pegis, M.L., Wise, C.F., Martin, D.J. & Mayer, J.M. Oxygen reduction by homogeneous  
782 molecular catalysts and electrocatalysts. *Chem. Rev.* **118**, 2340-2391 (2018).
- 783 [32] Yang, S., Kim, J., Tak, Y.J., Soon, A. & Lee, H. Single-atom catalyst of platinum supported on  
784 titanium nitride for selective electrochemical reactions. *Angew. Chem. Int. Ed.* **55**, 2058-2062  
785 (2016).
- 786 [33] Montemore, M.M., van Spronsen, M.A., Madix, R.J. & Friend, C.M. O<sub>2</sub> activation by metal  
787 surfaces: Implications for bonding and reactivity on heterogeneous catalysts. *Chem. Rev.* **118**,  
788 2816-2862 (2018).
- 789 [34] Wang, A., Li, J. & Zhang, T. Heterogeneous single-atom catalysis, *Nat. Rev. Chem.* **2**, 65-81

- (2018).
- [35] Shen, R. *et al.* High-concentration single atomic Pt sites on hollow CuSx for selective O<sub>2</sub> reduction to H<sub>2</sub>O<sub>2</sub> in acid solution, *Chem* **5**, 2099–2110 (2019).
- [36] Gao, J. *et al.* Enabling direct H<sub>2</sub>O<sub>2</sub> production in acidic media through rational design of transition metal single atom catalyst, *Chem* **6**, 1-17 (2020).
- [37] Jung, E. *et al.* Atomic-level tuning of Co-C-N catalyst for high performance electrochemical H<sub>2</sub>O<sub>2</sub> production, *Nat. Mater.* **19**, 436–442 (2020).
- [38] Nosaka, Y. & Nosaka, A. Introduction to Photocatalysis: From Basic Science to Applications (Royal Society of Chemistry, 2016).
- [39] Inoue, Y. Photocatalytic water splitting by RuO<sub>2</sub>-loaded metal oxides and nitrides with d<sup>0</sup>- and d<sup>10</sup>-related electronic configurations, *Energy Environ. Sci.* **2**, 364-386 (2009).
- [40] Li, X. *et al.* Single-atom Pt as co-catalyst for enhanced photocatalytic H<sub>2</sub> evolution, *Adv. Mater.* **28**, 2427–2431 (2016).
- [41] Naumkin, A. V., Kraut-Vass, A., Gaarenstroom, S.W. & Powell, C.J. NIST X-ray photoelectron spectroscopy database. figshare <http://dx.doi.org/10.18434/T4T88K> (2012).
- [42] Ravel, B. & Newville, M. ATHENA, ARTEMIS, HEPHAESTUS: data analysis for X-ray absorption spectroscopy using IFEFFIT, *J. Synchrotron Radiat.* **12**, 537–541 (2005).
- [43] Zhang, P. *et al.* Heteroatom dopants promote two-electron O<sub>2</sub> reduction for photocatalytic production of H<sub>2</sub>O<sub>2</sub> on polymeric carbon nitride, *Angew. Chem. Int. Ed.*, **59**, 16209-16217 (2020).
- [44] Kim, S. *et al.* Selective charge transfer to dioxygen on KPF<sub>6</sub>-modified carbon nitride for photocatalytic synthesis of H<sub>2</sub>O<sub>2</sub> under visible light, *J. Catal.* **357**, 51-58 (2018).
- [45] Yamakata, A., Ishibashi, T. & Onishi, H. Water- and oxygen-induced decay kinetics of photogenerated electrons in TiO<sub>2</sub> and Pt/TiO<sub>2</sub>: A time-resolved infrared absorption study, *J. Phys. Chem. B* **105**, 7258-7262 (2001).
- [46] Zhang, P. *et al.* Modified carbon nitride nanozyme as bifunctional glucose oxidase-peroxidase for metal-free bioinspired cascade photocatalysis, *Nat. Commun.* **10**, 940 (2019).
- [47] Sanville, E., Kenny, S.D., Smith, R. & Henkelman, G. Improved grid based algorithm for Bader charge allocation. *J. Comput. Chem.* **28**, 899–908 (2001).
- [48] Gao, H., Yan, S., Wang, J. & Zou, Z. Ion coordination significantly enhances the photocatalytic activity of graphitic-phase carbon nitride, *Dalton Trans.* **43**, 8178–8183 (2014).
- [49] Xiong, T. *et al.* KCl-mediated dual electronic channels in layered g-C<sub>3</sub>N<sub>4</sub> for enhanced visible light photocatalytic NO removal, *Nanoscale* **10**, 8066–8074 (2018).
- [50] Xiong, T., Cen, W., Zhang, Y. & Dong, F. Bridging the g-C<sub>3</sub>N<sub>4</sub> interlayers for enhanced photocatalysis, *ACS Catal.* **6**, 2462–2472 (2016).
- [51] Ghuman, K.K. *et al.* Photoexcited surface frustrated Lewis pairs for heterogeneous photocatalytic CO<sub>2</sub> reduction, *J. Am. Chem. Soc.* **138**, 1206-1214 (2016).
- [52] Bredas, J.-L. Mind the gap! *Mater. Horiz.*, **1**, 17-19 (2014).
- [53] Lu, T. & Chen, F. Multiwfn: A multifunctional wavefunction analyzer, *J. Comput. Chem.* **33**, 580-592 (2012).
- [54] Nakamura, R. & Nakato, Y. Primary intermediates of oxygen photoevolution reaction on TiO<sub>2</sub> (Rutile) particles, revealed by in situ FTIR absorption and photoluminescence measurements, *J. Am. Chem. Soc.* **126**, 1290-1298 (2004).
- [55] Jones, R., Summerville, D. & Basolo, F. Synthetic oxygen carriers related to biological systems,

- 834 *Chem. Rev.* **79**, 139-179 (1979).
- 835 [56] Li, S. *et al.* Effective photocatalytic H<sub>2</sub>O<sub>2</sub> production under visible light irradiation at g-C<sub>3</sub>N<sub>4</sub>  
836 modulated by carbon vacancies, *Appl. Catal. B* **190**, 26–35 (2016).
- 837 [57] Kofuji, Y. *et al.* Carbon nitride–aromatic diimide–graphene nanohybrids: Metal-free  
838 photocatalysts for solar-to-hydrogen peroxide energy conversion with 0.2% efficiency, *J. Am.*  
839 *Chem. Soc.* **138**, 10019-10025 (2016).
- 840 [58] Govind, N., Lopata, K., Rousseau, R., Andersen, A. & Kowalski, K. Visible light absorption  
841 of N-doped TiO<sub>2</sub> rutile using (LR/RT)-TDDFT and active space EOMCCSD calculations. *J.*  
842 *Phys. Chem. Lett.* **2**, 2696-2701 (2011).
- 843 [59] Bahers, T.L., Adamo, C. & Ciofini, I. A qualitative index of spatial extent in charge-transfer  
844 excitations, *J. Chem. Theory Comput.* **7**, 2498-2506 (2011).
- 845 [60] Kraner, S., Scholz, R., Plasser, F., Koerner, C. & Leo, K. Exciton size and binding energy  
846 limitations in one-dimensional organic materials, *J. Chem. Phys.* **143**, 244905 (2015).
- 847 [61] Kraner, S., Prampolini, O. & Cuniberti, G. Exciton binding energy in molecular triads, *J. Phys.*  
848 *Chem. C* **121**, 17088-17095 (2017).
- 849 [62] Kislitsyn, D. *et al.* Spatial mapping of sub-bandgap states induced by local nonstoichiometry  
850 in individual lead sulfide nanocrystals, *J. Phys. Chem. Lett.* **5**, 3701-3707 (2014).
- 851 [63] Nørskov, J.K. *et al.* Origin of the overpotential for oxygen reduction at a fuel-cell cathode. *J.*  
852 *Phys. Chem. B* **108**, 17886-17892 (2004).
- 853 [64] Calle-Vallejo, F., Martí'nez, J.I. & Rossmeisl, J. Density functional studies of functionalized  
854 graphitic materials with late transition metals for oxygen reduction reactions. *Phys. Chem.*  
855 *Chem. Phys.* **13**, 15639–15643 (2011).
- 856 [65] Xu, H., Cheng, D., Cao, D. & Zeng, X.C. A universal principle for a rational design of single-  
857 atom electrocatalysts. *Nat. Catal.* **1**, 339–348 (2018).
- 858 [66] Kresse, G. & Furthmüller, J. Efficient iterative schemes for *ab initio* total-energy calculations  
859 using a plane-wave basis set, *J. Phys. Rev. B* **54**, 11169–11186 (1996).
- 860 [67] Kresse, G. & Furthmüller, J. Efficiency of *ab-initio* total energy calculations for metals and  
861 semiconductors using a plane-wave basis set. *J. Comput. Mater. Sci.* **6**, 15–50 (1996).
- 862 [68] Perdew, J.P., Burke K. & Ernzerhof, M. Generalized gradient approximation made simple,  
863 *Phys. Rev. Lett.* **77**, 3865-3868 (1996).
- 864 [69] Blöchl, P.E. Projector augmented-wave method, *Phys. Rev. B* **50**, 17953-17979 (1994).
- 865 [70] Press, W.H., Teukolsky, S.A., Vetterling, W.T. & Flannery, B.P. Numerical recipes, (Cambridge  
866 University Press, 2007).

867

## 868 **Acknowledgements**

869 The authors acknowledge the financial support of Mitsubishi Chemical Corporation, JSPS  
870 Grant-in-Aid for Scientific Research (B, No. 20H02847), Grant-in-Aid for JSPS Fellows  
871 (DC2, 20J13064), Project National Natural Science Foundation of China (21805191,  
872 21972094), the Guangdong Basic and Applied Basic Research Foundation  
873 (2020A1515010982), Shenzhen Pengcheng Scholar Program, Shenzhen Peacock Plan  
874 (KQJSCX20170727100802505, KQTD2016053112042971), the Singapore Ministry of

31

**Commented [TB47]:** this section together with Author contributions and Competing interests should be placed at the end of the manuscript.

**Commented [TB48R47]:** We have removed these sections at the end of manuscript.

875 Education Academic Research Fund (AcRF) Tier 1: RG115/17 and RG115/18, and Tier 2:  
876 MOE2016-T2-2-004, and Singapore Energy Center (SgEC) M4062755.120. The authors  
877 thank Dr. Xiang Huang from Department of Physics, Southern University of Science and  
878 Technology for his help in theoretical calculation and Dr. Nan Jian from the Electron  
879 Microscope Center of the Shenzhen University for for his help in HRTEM measurement.

880

#### 881 **Author Contributions Statement**

882 Z.T., Q.Z. and T.O. conceptualized the project. T.O., C.S. and B.L. supervised the project.

883 Z.T. synthesized the catalysts, conducted the catalytic tests and the related data

884 processing, and performed materials characterization and analysis with the help of H.Y.,

885 Q.Z., Y.-R.L. and S.L. K.K. and A.Y. conducted transient absorption spectroscopy. Z.T., W.Y.

886 and C.W. performed the theoretical study. Z.T., H.Y. and B.L. wrote the manuscript with

887 support from all authors.

888

#### 889 **Competing Interests Statement**

890 The authors declare no competing interests.

891

**Commented [TB49]:** Competing Interests

**Commented [TB50R49]:** The title of this section has been revised.

**Commented [TB51]:** Please remove "financial", the declarations must be broader as per our policy.

**Commented [TB52R51]:** We have removed the word "financial" by following the suggestion of editor.



892

Supplementary Information for

893 **Atomically Dispersed Antimony on Carbon Nitride for the Artificial Photosynthesis**  
894 **of Hydrogen Peroxide**

895  
896 Zhenyuan Teng,<sup>1,7,8</sup> Qitao Zhang,<sup>2,8</sup> Hongbin Yang,<sup>3,8</sup> Kosaku Kato,<sup>4</sup> Wenjuan Yang,<sup>2</sup> Ying-  
897 Rui Lu,<sup>5</sup> Sixiao Liu,<sup>6,7</sup> Chengyin Wang,<sup>6,7</sup> Akira Yamakata,<sup>4</sup> Chenliang Su,<sup>2,\*</sup> Bin Liu,<sup>3,\*</sup> and  
898 Teruhisa Ohno<sup>1,7,\*</sup>

899

900 <sup>1</sup>Department of Applied Chemistry, Faculty of Engineering, Kyushu Institute of Technology,  
901 Kitakyushu 804-8550, Japan

902 <sup>2</sup>International Collaborative Laboratory of 2D Materials for Optoelectronics Science and  
903 Technology of Ministry of Education, Institute of Microscale Optoelectronics, Shenzhen  
904 University, Shenzhen 518060, China

905 <sup>3</sup>School of Chemical and Biomedical Engineering, Nanyang Technological University, 62  
906 Nanyang Drive, Singapore 637459, Singapore

907 <sup>4</sup>Graduate School of Engineering, Toyota Technological Institute, 2-12-1 Hisakata,  
908 Tempaku Nagoya 468-8511, Japan

909 <sup>5</sup>National Synchrotron Radiation Research Center, Hsinchu 30076, Taiwan

910 <sup>6</sup>College of Chemistry and Chemical Engineering, Yangzhou University, 180 Si-Wang-Ting  
911 Road, Yangzhou 225002, China

912 <sup>7</sup>Joint Laboratory of Yangzhou University, Kyushu Institute of Technology, Yangzhou  
913 University, 180 Si-Wang-Ting Road, Yangzhou 225002, China

914 <sup>8</sup>These authors contributed equally.

915

916 ORCID:

917 Teruhisa Ohno: <https://orcid.org/0000-0002-7825-8189>

918 Chenliang Su: <https://orcid.org/0000-0002-8453-1938>

919 Bin Liu: <https://orcid.org/0000-0002-4685-2052>

920 E-mail address:

921 Teruhisa Ohno: [tohno@che.kyutech.ac.jp](mailto:tohno@che.kyutech.ac.jp)

922 Chenliang Su: [chmsuc@nus.edu.sg](mailto:chmsuc@nus.edu.sg)

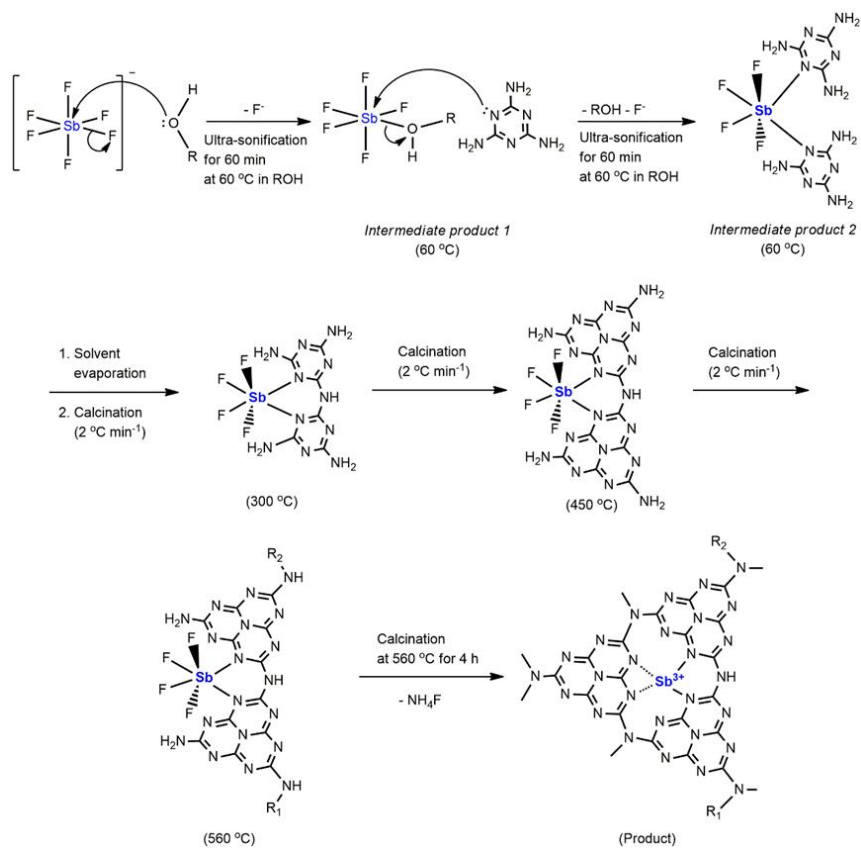
923 Bin Liu: [liubin@ntu.edu.sg](mailto:liubin@ntu.edu.sg)

924

925

Commented [TB53]: Please make the title consistent with the one in the Main Manuscript

Commented [TB54R53]: We agree with the editor that the revised title is more specific. We have changed the title.



926

927 **Supplementary Figure 1. The preparation procedure of the single Sb atom**  
 928 **photocatalyst (Sb-SAPC).** Dashed bonds in the product refers to the weak interaction  
 929 between N and Sb atoms.

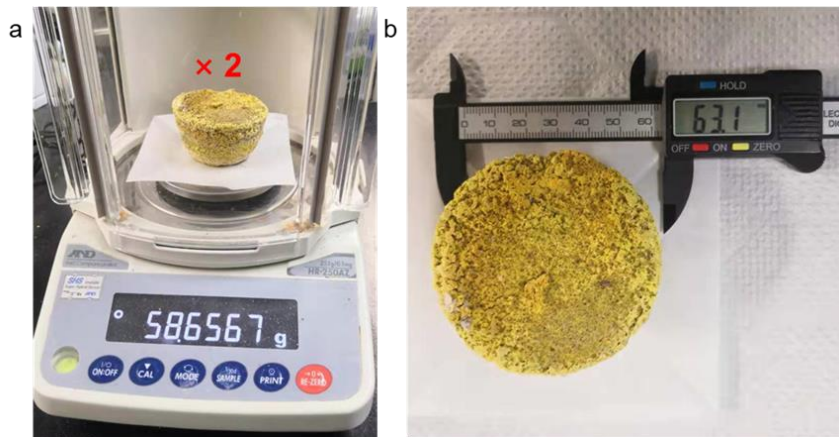
930

Commented [TB55]: Please change this into a figure.

Commented [TB56R55]: We have changed the "scheme" into "figure".

Commented [TB57]: Please consider submitting part of the supplementary figures as EXTENDED DATA: Extended Data is an integral part of the paper and only data that directly contribute to the main message should be presented.

Commented [TB58R57]: Figure 19,23,27,29,30,31,34,40,44 will be submitted as EXTENDED DATA.



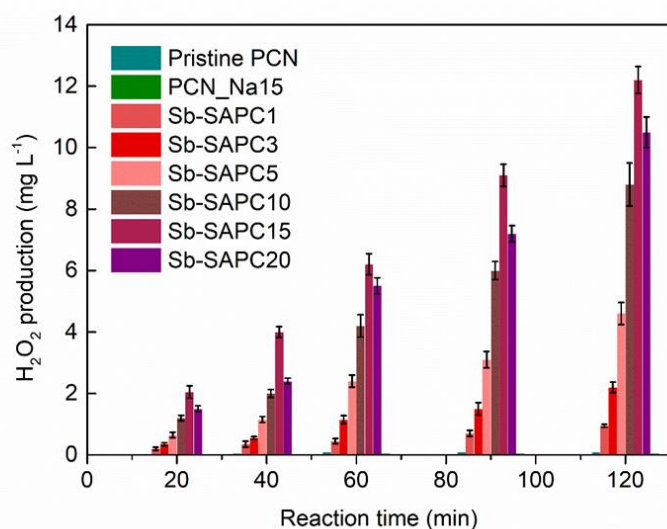
931

932 **Supplementary Figure 2 | Digital photographs showing the as-prepared Sb-SAPC15**

933 **in one batch.**

934

935



936

937

938

939

940

941

942

943

944

945

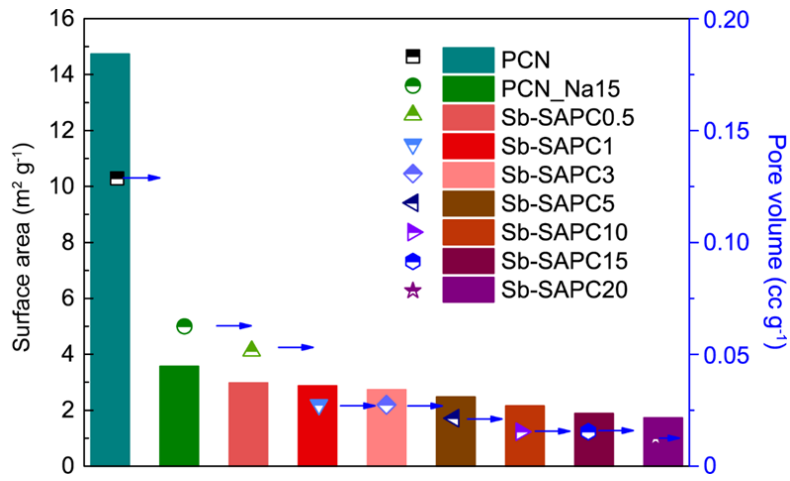
946

947

948

**Supplementary Figure 3 | Comparison of activities of Sb-SAPCs and PCNs for photocatalytic H<sub>2</sub>O<sub>2</sub> production** (light source: Xe lamp, light intensity at 420–500 nm: 30.3 W m<sup>-2</sup>; reaction medium: water at pH = 10.1 for Sb-SAPC15). Error bars represent the standard deviations of 3 replicate measurements.

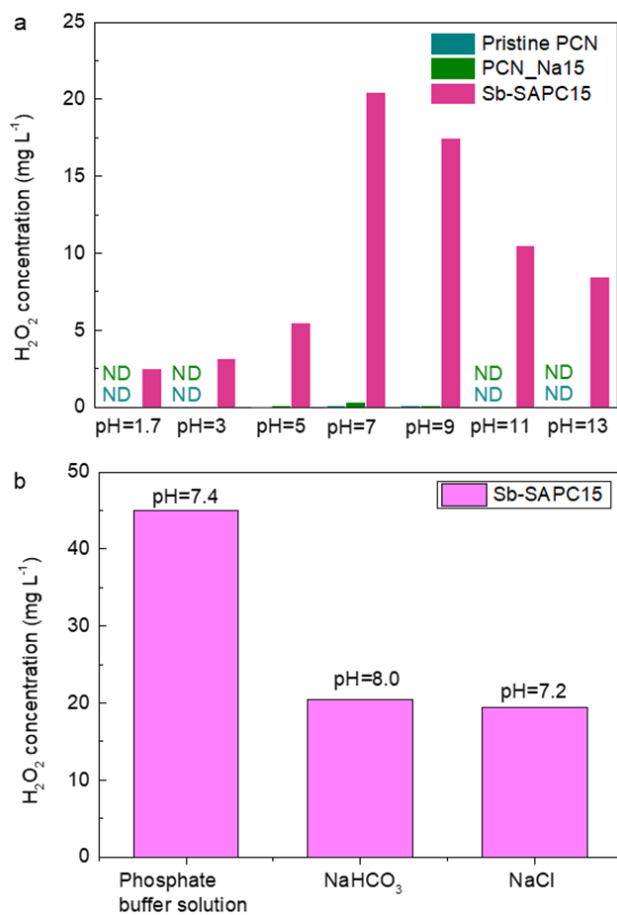
The pH of the Sb-SAPC15 aqueous suspension (solvent is pure water) is 10.1 because addition of Sb-SAPC15 particles significantly accelerated self-ionization of water. The zeta potential of Sb-SAPC15 reached -30 mV in an acid solution, indicating that Sb-SAPC15 could be recognized as a solid-state Lewis base. Addition of Lewis base into pure water could accelerate water self-ionization, thus leading to a significantly increased pH.



949

950 **Supplementary Figure 4 | Specific surface area and average pore volume of PCN,**  
 951 **PCN\_Na15 and Sb-SAPCx.**

952



953

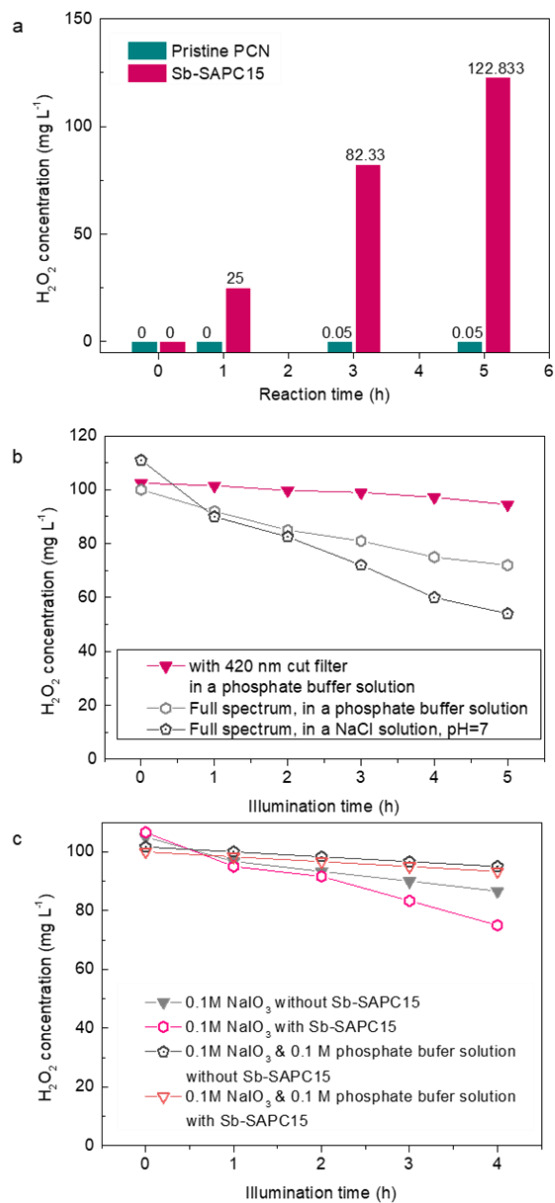
954

955

956

957

**Supplementary Figure 5 | Optimization experiments for non-sacrificial photocatalytic H<sub>2</sub>O<sub>2</sub> production. a, pH optimization. b, Solvent optimization. (light source: Xe lamp, light intensity at 420–500 nm: 30.3 W m<sup>-2</sup>). The reaction time is 90 min.**



958

959

960

961

962

963

964

**Supplementary Figure 6 | Long term activity for non-sacrificial photocatalytic H<sub>2</sub>O<sub>2</sub> production.** **a**, Long term photocatalytic H<sub>2</sub>O<sub>2</sub> production using Sb-SAPC15 and pristine PCN as the photocatalyst. **b**, Optimization for light wavelength for H<sub>2</sub>O<sub>2</sub> degradation study. **c**, Interactions between photogenerated holes and H<sub>2</sub>O<sub>2</sub> in different kinds of solutions. The solution was irradiated by a 300 W Xenon Lamp with a UV cut filter (light intensity: 30.3 W m<sup>-2</sup> at 420-500 nm).

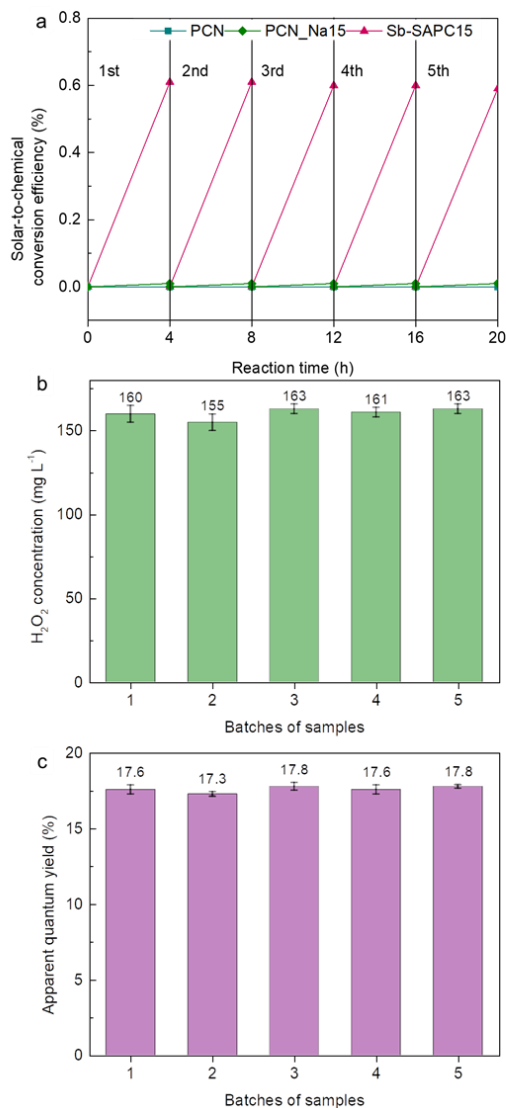
965 The change in concentration of H<sub>2</sub>O<sub>2</sub> with an electron acceptor versus time was plotted  
966 to investigate whether the holes transferred to H<sub>2</sub>O<sub>2</sub> (Supplementary Figure 6c). The  
967 concentration of H<sub>2</sub>O<sub>2</sub> gradually decreased in 0.1 M NaIO<sub>3</sub> without Sb-SAPC since slight  
968 decomposition of H<sub>2</sub>O<sub>2</sub> was unavoidable under visible light irradiation with high light  
969 intensity. After addition of Sb-SAPC15, the decomposition of H<sub>2</sub>O<sub>2</sub> was accelerated,  
970 indicating that the transfer of photogenerated holes could decompose H<sub>2</sub>O<sub>2</sub> in 0.1 M NaIO<sub>3</sub>  
971 solution. This phenomenon further confirmed that H<sub>2</sub>O<sub>2</sub> could serve as a hole scavenger,  
972 which should be considered during the photocatalytic H<sub>2</sub>O<sub>2</sub> production. However, addition  
973 of the phosphate buffer solution could significantly suppress the decomposition of H<sub>2</sub>O<sub>2</sub>.  
974 These results indicate the crucial role of phosphate buffer solution, which is able to stabilize  
975 the produced H<sub>2</sub>O<sub>2</sub> during the photocatalytic process.  
976  
977

**Commented [TB59]:** Please avoid the use of "Note" after the Supplementary Figures, as this may create confusion with the Supplementary Notes.

The text can be kept without caption.

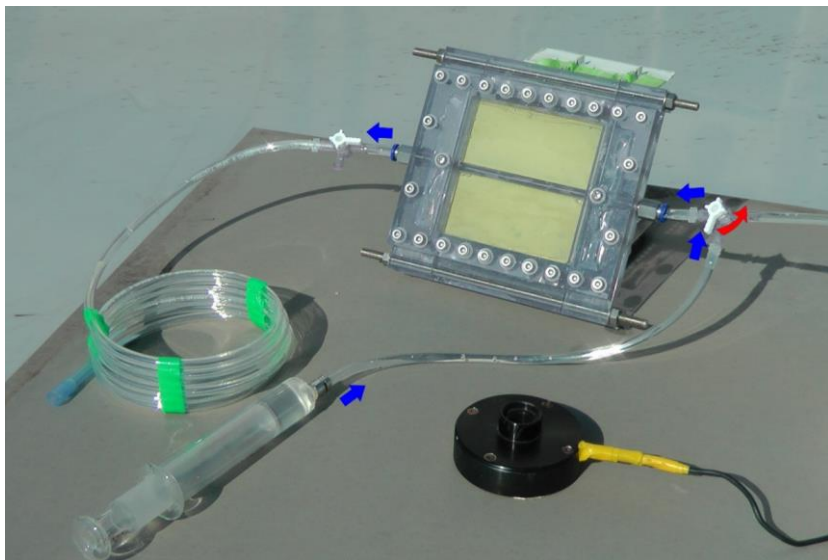
**Commented [TB60R59]:** We have removed the word "Note" below the figures.





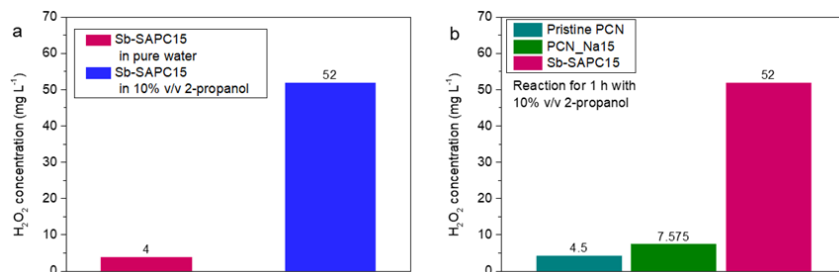
978  
979  
980  
981  
982  
983  
984  
985  
986  
987

**Supplementary Figure 7 | Repeatability and reproducibility of catalysts.** **a**, Repeatability of the CN samples for photocatalytic production of H<sub>2</sub>O<sub>2</sub>. After each run, the catalyst was filtered and re-suspended in a fresh solution with pH adjusted to 7.4 by phosphate buffer solution. **b**, Reproducibility of photocatalytic H<sub>2</sub>O<sub>2</sub> production for calculating solar-to-chemical conversion efficiency. **c**, Reproducibility for apparent quantum yield ( $\lambda = 420$  nm). Light source: Xe lamp, light intensity at 420–500 nm: 30.3 W m<sup>-2</sup>; reaction medium: phosphate buffer solution at pH = 7.4. Error bars represent the standard deviation of 3 replicate measurements.



988

989 **Supplementary Figure 8 | The practical experiment of photocatalytic H<sub>2</sub>O<sub>2</sub>**  
990 **production using solar light.** The blue arrow indicates the flow direction of aqueous  
991 solution. The red arrow tells the direction to open the valve.  
992



993

994

**Supplementary Figure 9 | Half reaction with addition of an electron donor. a,**

995

Comparison of H<sub>2</sub>O<sub>2</sub> formed in pure water and 10% (v/v) 2-propanol aqueous solution

996

catalyzed by Sb-SAPC15. **b,** Comparison of H<sub>2</sub>O<sub>2</sub> production in 10% (v/v) 2-propanol

997

aqueous solution catalyzed by pristine PCN, PCN\_Na15 and Sb-SAPC15. Reaction time:

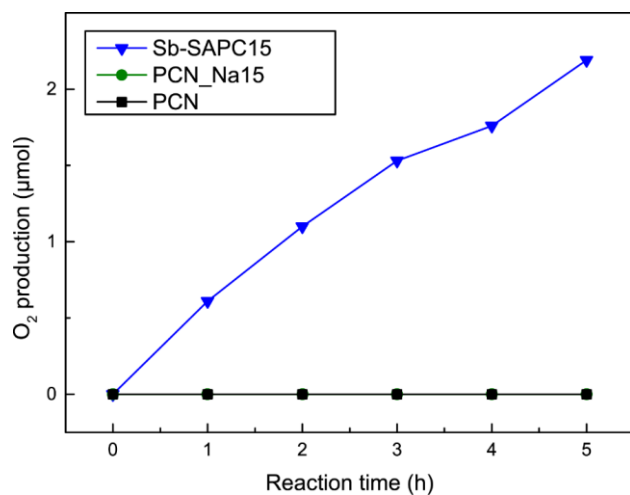
998

60 min. Irradiation condition:  $\lambda > 420$  nm (Xe lamp, light intensity at 400–500 nm: 30.3 W

999

m<sup>-2</sup>), at 298 K.

1000

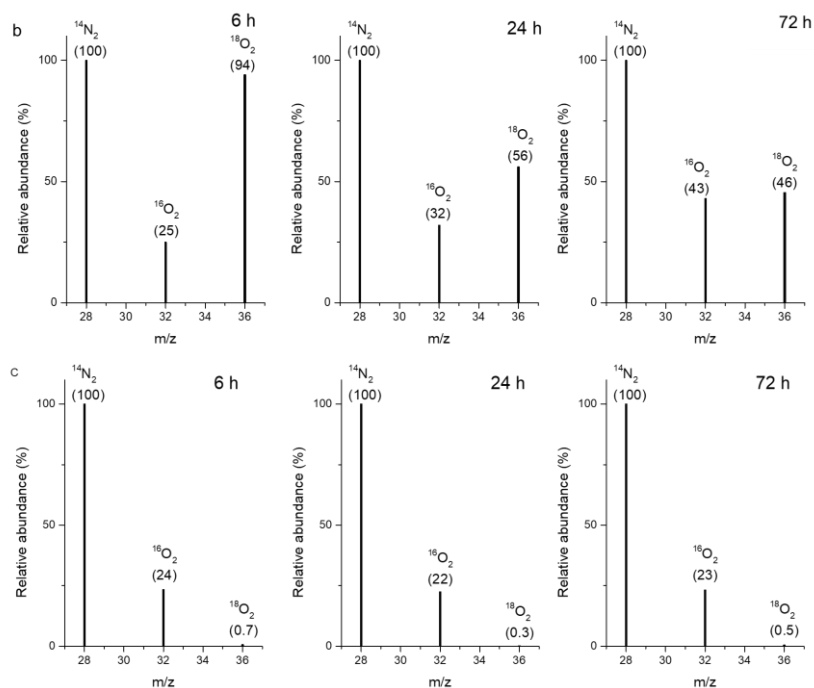
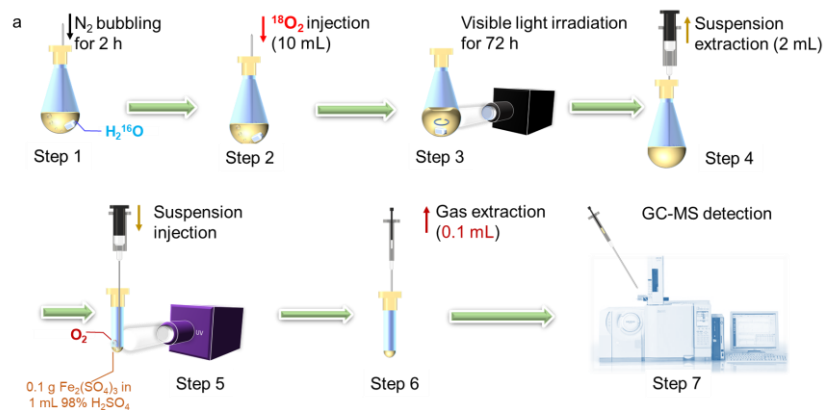


1001

1002 **Supplementary Figure 10 | Comparison of oxygen evolution efficiency for PCN,**

1003 **PCN\_Na15 and Sb-SAPC15 during the half reaction.**

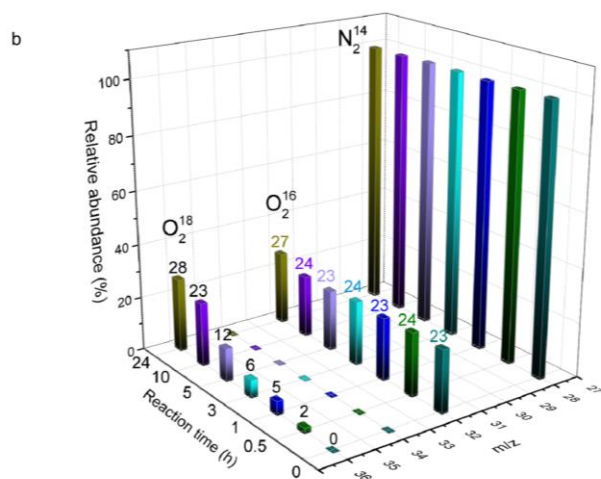
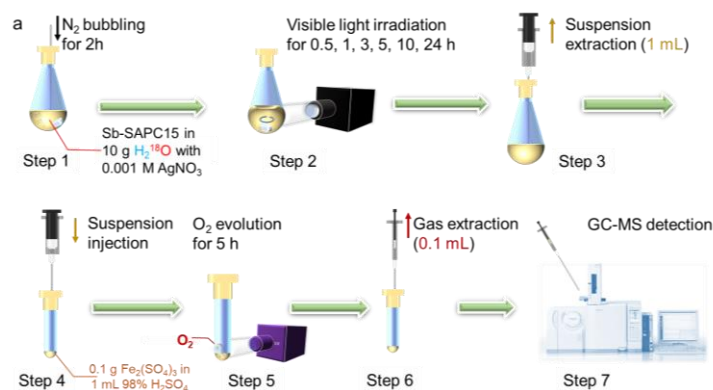
1004



1005

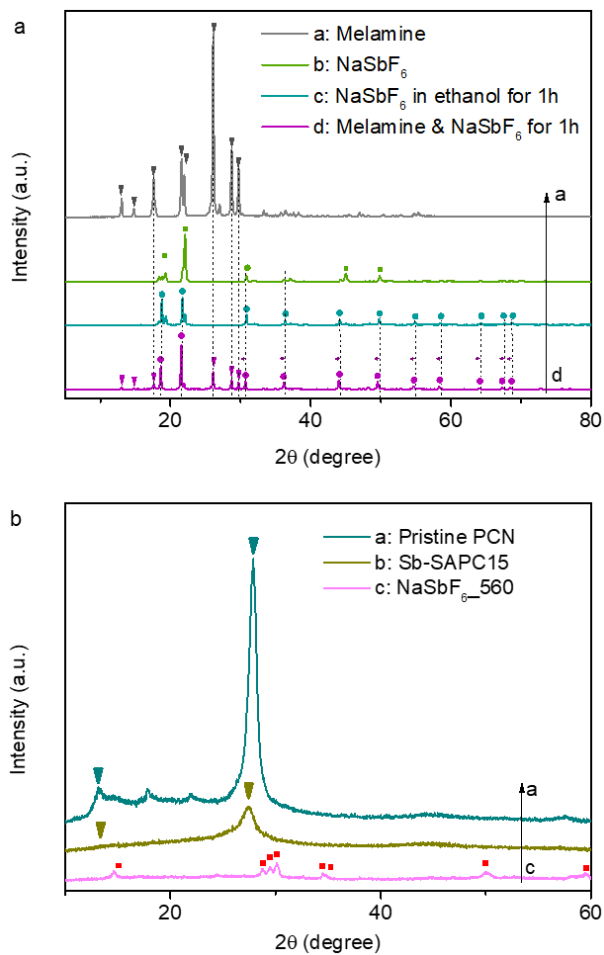
1006 **Supplementary Figure 11 | Isotopic experiments utilizing  $^{18}\text{O}_2$ .** **a**, Schematic diagram  
 1007 showing the isotopic experimental procedure for  $\text{H}_2\text{O}_2$  production with addition of  $^{18}\text{O}_2$  as  
 1008 the electron acceptor (The figure of GC-MS in step 7 is taken from  
 1009 <https://www.an.shimadzu.co.jp/gcms/2010se.htm>). **b**, GC-MS spectra of the gas extracted  
 1010 from the Sb-SAPC15/ $\text{Fe}^{3+}$  system after the light illumination for 6 h, 24 h and 72 h in step  
 1011 3. **c**, GC-MS spectra of the gas extracted from the same system without addition of Sb-  
 1012 SAPC15 at the reaction time point of 6 h, 24 h and 72 h in step 3. The reaction solution is  
 1013 pure  $\text{H}_2^{16}\text{O}$  with injection of 10 mL  $^{18}\text{O}_2$ .

1014 We have performed control experiment to ensure that the  $^{18}\text{O}_2$  injected at the  
1015 beginning of the experiment could be barely measured later. The details for the experiment  
1016 are as follows: all experiments are the same as the experimental procedure except the  
1017 addition of the photocatalyst. In this case, the  $\text{H}_2\text{O}_2$  could hardly be formed, and only  
1018 dissolved oxygen existed in the liquid phase<sup>1</sup>. As shown in step 3, the dissolved oxygen  
1019 could be transferred to step 4 when liquid was extracted from the solution. The gas  
1020 extracted from step 6 was also measured by GC-MS. As shown in the figure above, we  
1021 could hardly detect the signal of  $^{18}\text{O}_2$ , indicating that the dissolved oxygen in the extracted  
1022 solution (step 3) barely influenced the measurement. Note that the signal of  $^{16}\text{O}_2$  is  
1023 attributed to the small leakage of  $\text{O}_2$  during the injection process.  
1024



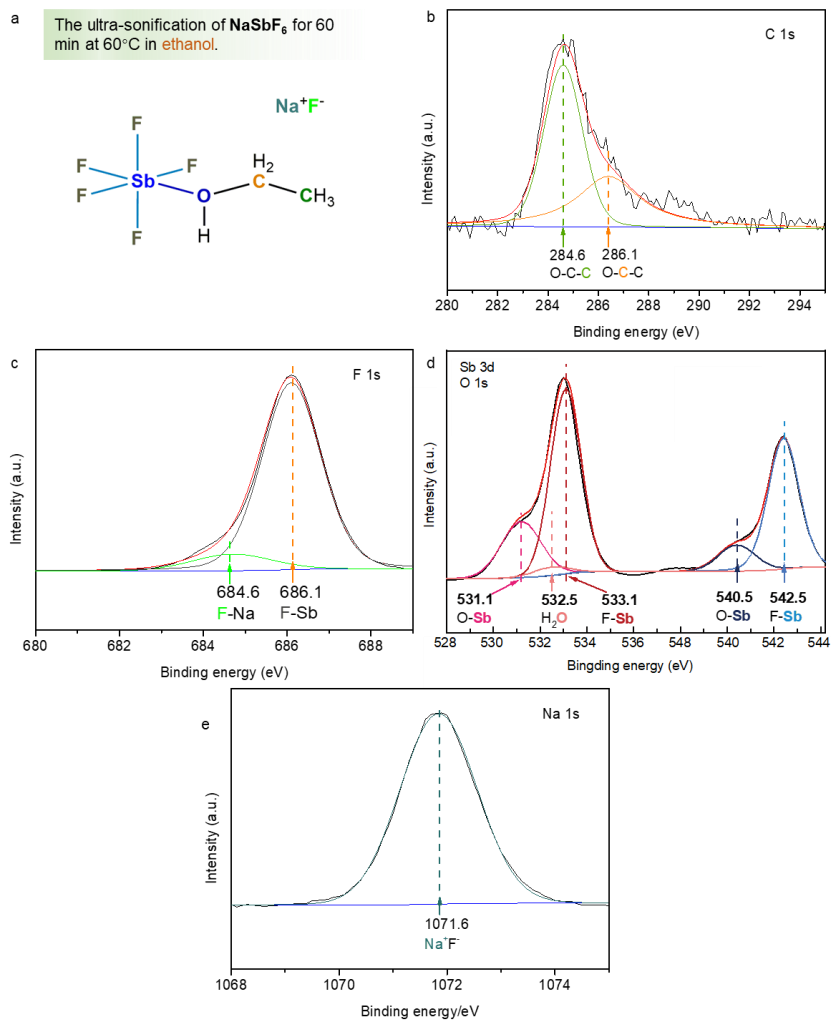
1025  
1026 **Supplementary Figure 12 | Isotopic experiments utilizing  $H_2^{18}O$ .** a, Schematic diagram  
1027 showing the isotopic experimental procedure for  $H_2O_2$  production with addition of  $Ag^+$  as  
1028 the electron acceptor (The figure of GC-MS in step 7 is taken from  
1029 <https://www.an.shimadzu.co.jp/gcms/2010se.htm>). b, GC-MS spectra of the gas extracted  
1030 from the Sb-SAPC15/ $Fe^{3+}$  system after the Xenon lamp illumination of 0 h, 0.5 h, 1 h, 3 h,  
1031 5 h, 10 h and 24 h in step 2. The reaction solution is pure  $H_2^{18}O$  with saturated ultrapure  
1032  $N_2$ . (Mass of the catalyst in step 1: 50 mg,  $Ag^+$  concentration: 0.001M).  
1033

1034 The signal of  $^{16}O_2$  is attributed to the small leakage of  $O_2$  during the injection process  
1035 (step 7) since the signals of  $^{16}O_2$  are almost the same (~23 %). Similar phenomenon could  
1036 be also observed in the Supplementary Figure 11c even no  $^{16}O_2$  was injected in the system.  
1037 Although this system error existed, the increasing signal of  $^{18}O_2$  with extended reaction  
1038 time still revealed the water oxidation gradually happened with the addition of the electron  
1039 acceptor.



1040  
 1041 **Supplementary Figure 13 | X-ray diffraction (XRD) patterns.** a, XRD patterns of a:  
 1042 melamine; b: NaSbF<sub>6</sub>; c: 3.881 g NaSbF<sub>6</sub> in ethanol with sonification for 1 hour  
 1043 (*Intermediate Product 1*); d: sample c mixed with 4 g of melamine in ethanol with 1 hour  
 1044 sonification (*Intermediate Product 2*). b, XRD patterns of pristine PCN, Sb-SAPC15 and  
 1045 NaSbF<sub>6</sub> prepared at 560 °C for 4 h (NaSbF<sub>6</sub>\_560).  
 1046





1047

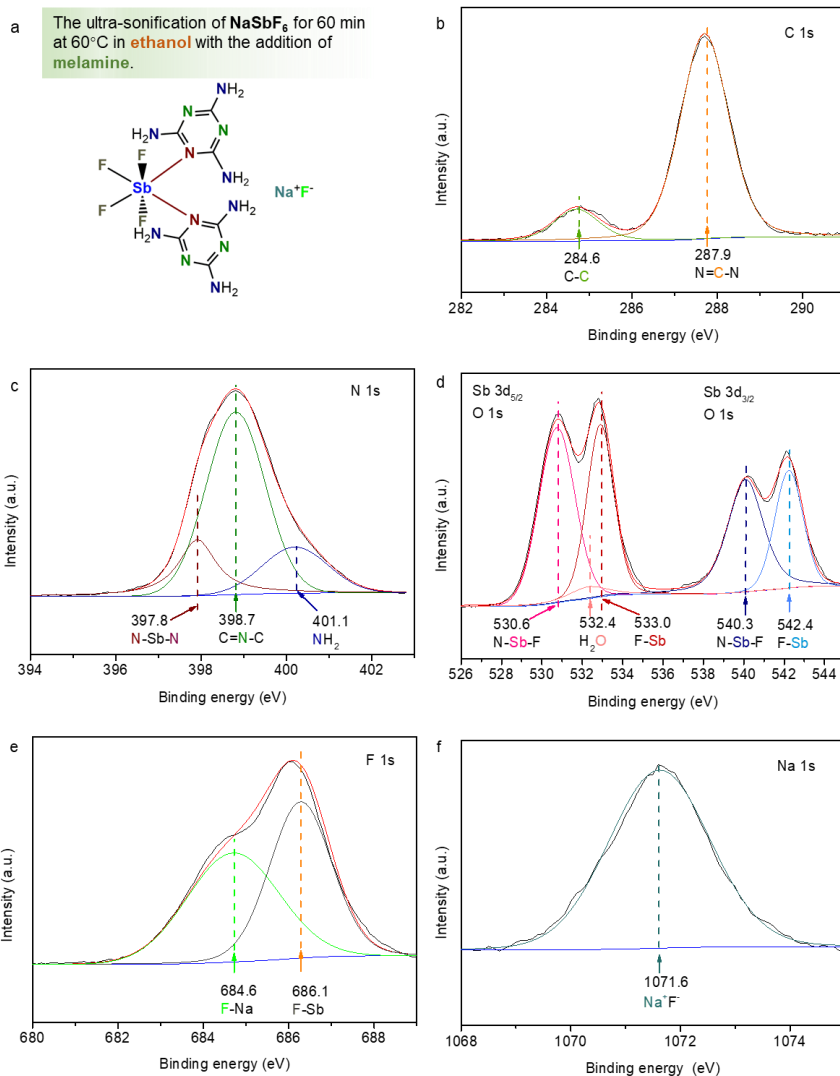
1048

1049

1050

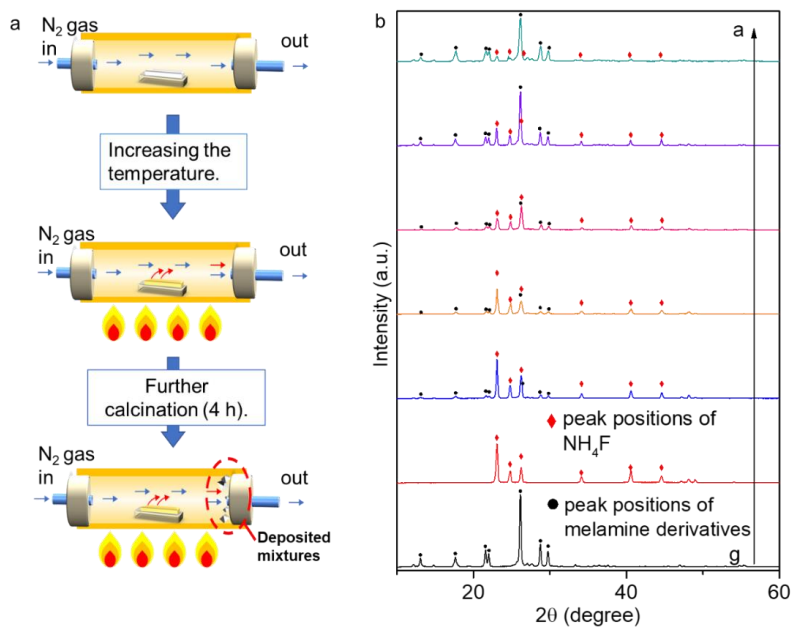
1051

**Supplementary Figure 14 | XPS spectra of 3.881 g  $\text{NaSbF}_6$  in ethanol with sonification for 1 hour (Intermediate Product 1). a, Structure of Intermediate Product 1. b-e, High-resolution XPS spectra of C 1s (b), F 1s (c), Sb3d & O 1s (d) and Na 1s (e).**



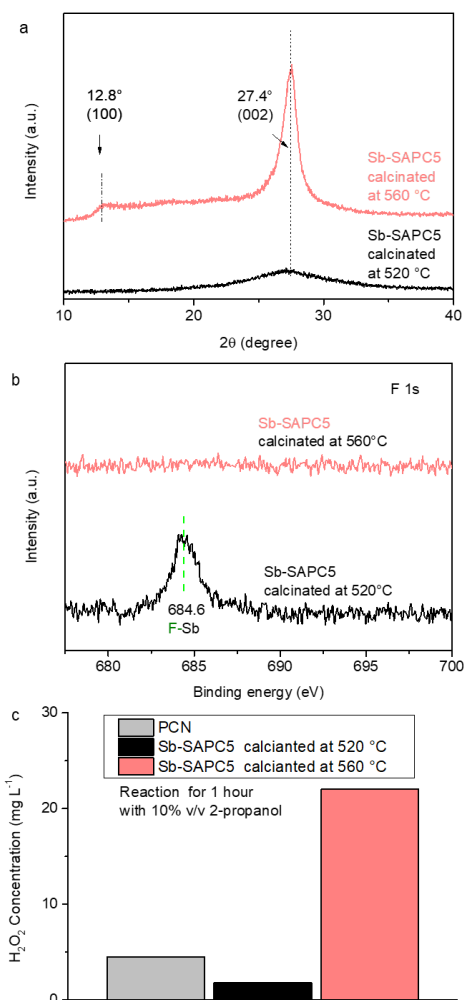
1052

1053 **Supplementary Figure 15 | XPS spectra of 3.881 g  $\text{NaSbF}_6$  in ethanol with sonification**  
 1054 **for 1 hour, followed by mixed with 4 g of melamine in ethanol with 1 hour sonification**  
 1055 **(Intermediate Product 2). a, Structure of Intermediate Product 2. b-f, High-resolution XPS**  
 1056 **spectra of C 1s (b), N 1s (c), Sb3d & O 1s (d), F 1s (e) and Na 1s (f).**  
 1057



1058  
 1059  
 1060  
 1061  
 1062  
 1063  
 1064  
 1065

**Supplementary Figure 16 | Characterization of the deposited mixture on the silicone plug of the tube furnace.** **a.** A schematic diagram showing the deposition process during calcination. **b.** XRD patterns of the deposited mixture obtained during preparation of Sb-SAPC1 (pattern a), Sb-SAPC3 (pattern b), Sb-SAPC5 (pattern c), Sb-SAPC10 (pattern d), and Sb-SAPC15 (pattern e). XRD patterns of pure  $\text{NH}_4\text{F}$  (pattern f) and the deposited mixture during preparation of PCN (pattern g) are also included as references.



1066

1067

1068

1069

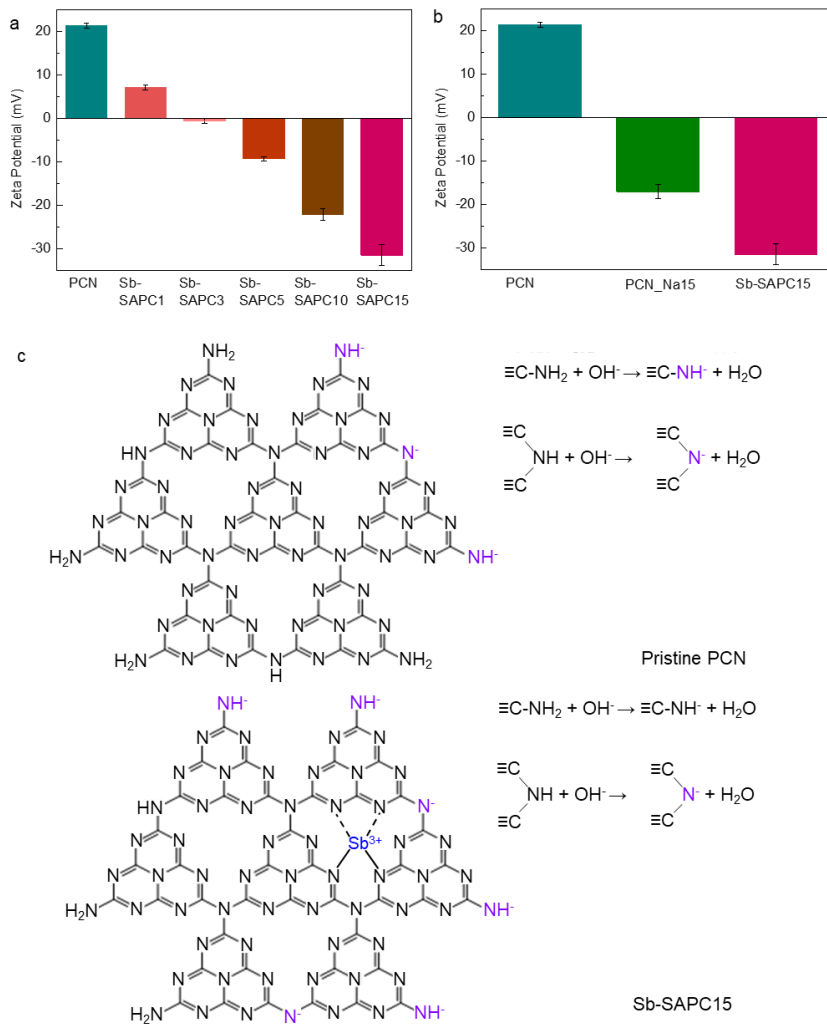
1070

1071

1072

1073

**Supplementary Figure 17 | Comparison of Sb-SAPCs prepared at different temperatures.** **a-b** XRD patterns (**a**) and high-resolution F 1s spectra (**b**) of Sb-SAPC5 prepared at 520 °C and 560 °C. **c**, Comparison of H<sub>2</sub>O<sub>2</sub> formed 10% (v/v) 2-propanol aqueous solution catalyzed by PCN and Sb-SAPC5 prepared at 520 °C and 560 °C. Reaction time: 60 min. Irradiation condition:  $\lambda > 420$  nm (Xe lamp, light intensity at 400–500 nm: 30.3 W m<sup>-2</sup>), at 298 K.



1074

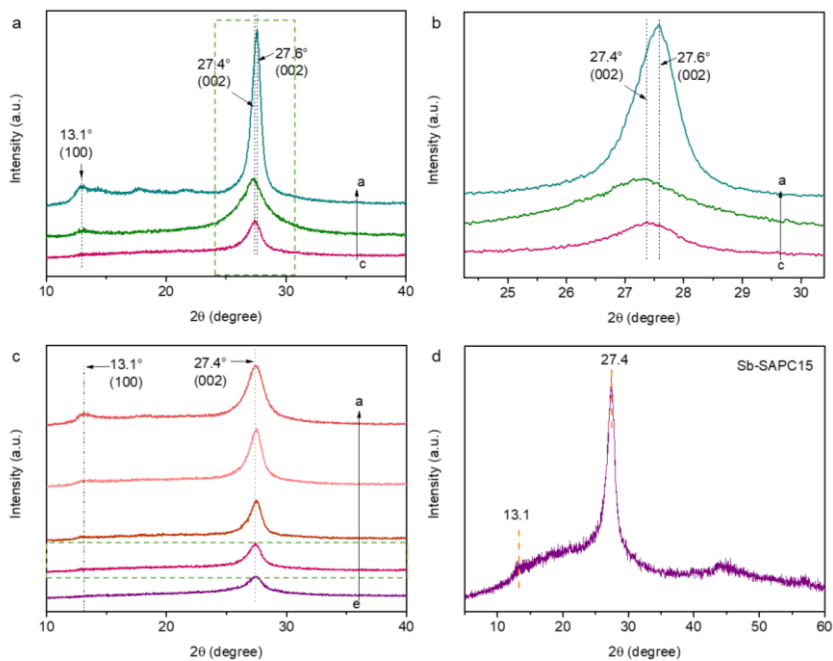
1075

1076

1077

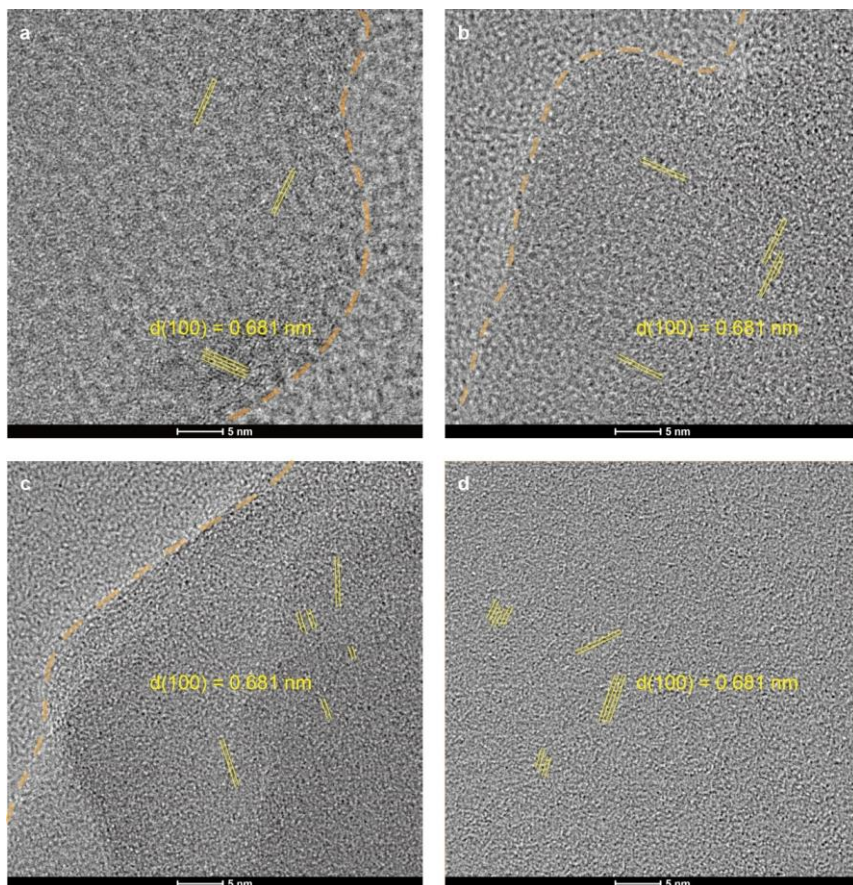
1078

**Supplementary Figure 18 | Surface charge of Sb-SAPCs and PCN samples at pH = 3.**  
**a**, Zeta-potential of Sb-SAPCs with different Sb contents. **b**, Zeta-potential of PCN, PCN\_Na15 and Sb-SAPC15. **c**, The possible mechanism of gradually increased surface negativity of Sb-SAPCs.



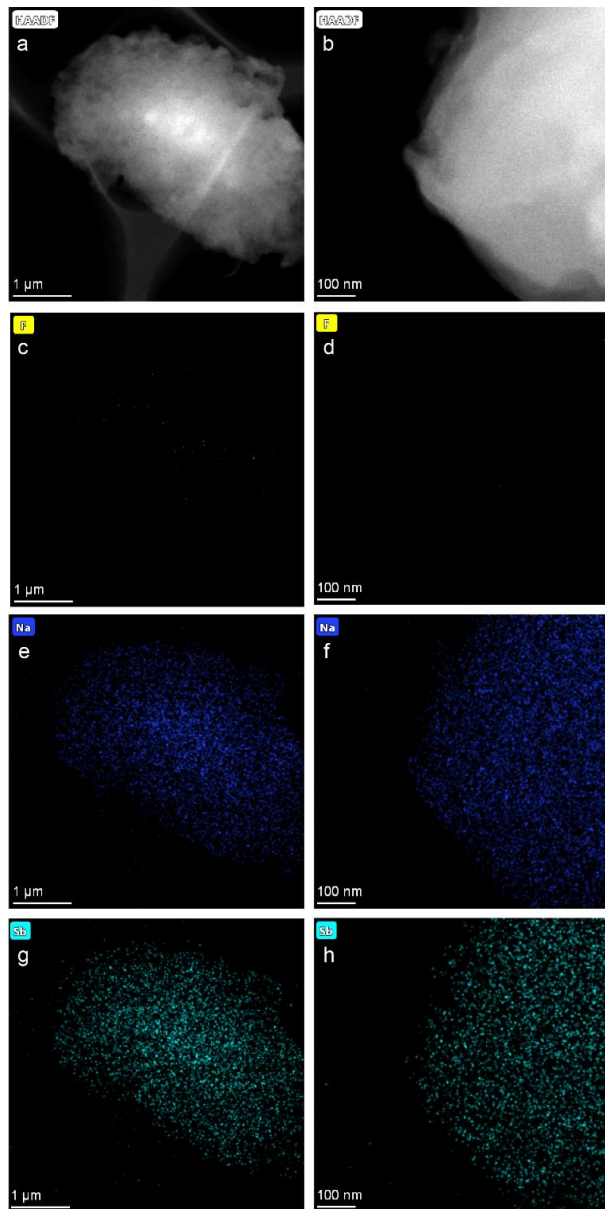
1079  
 1080  
 1081  
 1082  
 1083  
 1084  
 1085

**Supplementary Figure 19 | Crystallinity characterized by X-ray diffraction. a**, XRD patterns of a: pristine PCN; b: PCN\_Na15; and c: Sb-SAPC15. **b**, XRD patterns (high-resolution) of carbon nitride samples. **c**, XRD patterns of a: Sb-SAPC1; b: Sb-SAPC5; c: Sb-SAPC10; d: Sb-SAPC15; and e: Sb-SAPC20. **d**, XRD patterns (high-resolution) of Sb-SAPC15.



1086  
1087  
1088  
1089  
1090  
1091

**Supplementary Figure 20 | Crystallinity characterized by high-resolution transmission electron microscopy. a-d, HR-TEM images of Sb-SAPC1 (a), Sb-SAPC5 (b), Sb-SAPC10 (c) and Sb-SAPC15 (d). The yellow line indicates the lattice fringe of the (100) plane of PCN.**



1092

1093

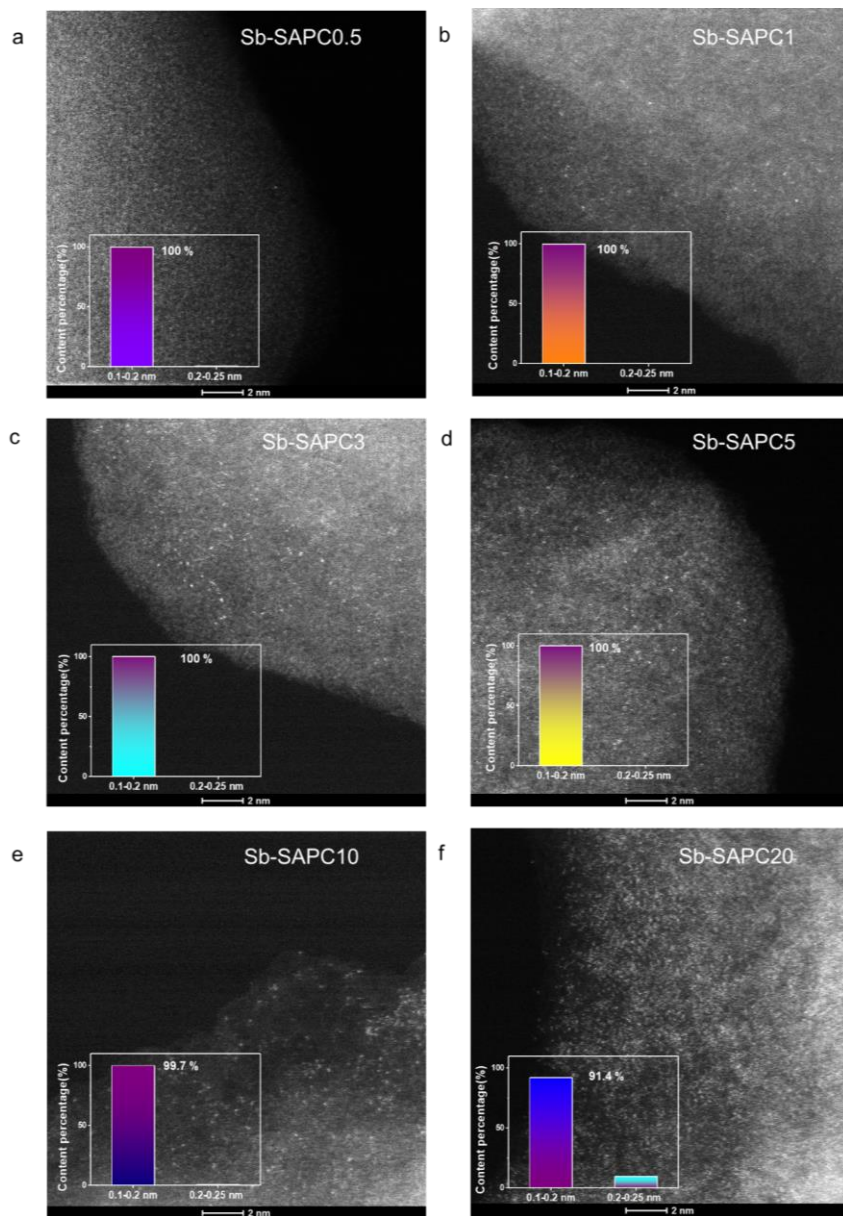
1094

1095

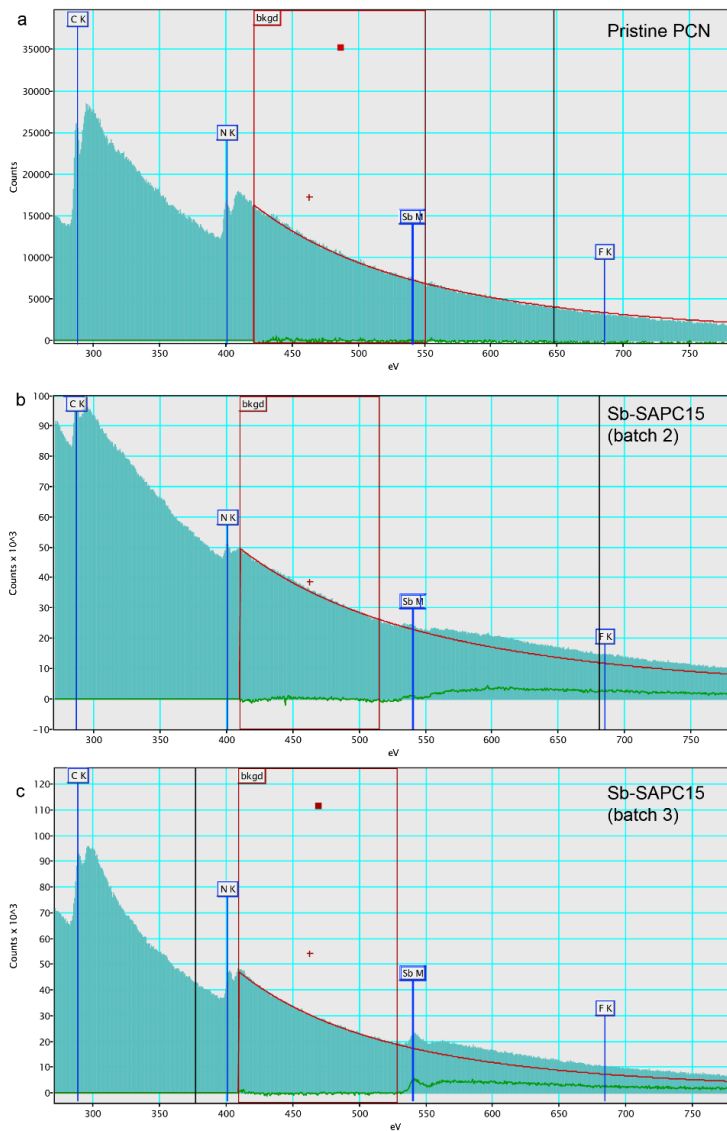
1096

**Supplementary Figure 21 | Elemental distribution in Sb-SAPC15.** a-b, Low and high-magnification HAADF-STEM images of Sb-SAPC15. c-h, The corresponding EDS elemental mapping images of F (c-d), Na (e-f) and Sb (g-h) at low and high-magnification.





1097  
 1098 **Supplementary Figure 22 | Characterization of isolated Sb species in Sb-SAPCs with**  
 1099 **different Sb contents. a-f,** HAADF-STEM images of Sb-SAPC0.5 (a), Sb-SAPC1 (b), Sb-  
 1100 Sb-SAPC3 (c), Sb-SAPC5 (d), Sb-SAPC10 (e) and Sb-SAPC20 (f). Inset shows the size  
 1101 distribution of the bright spots.  
 1102



1103

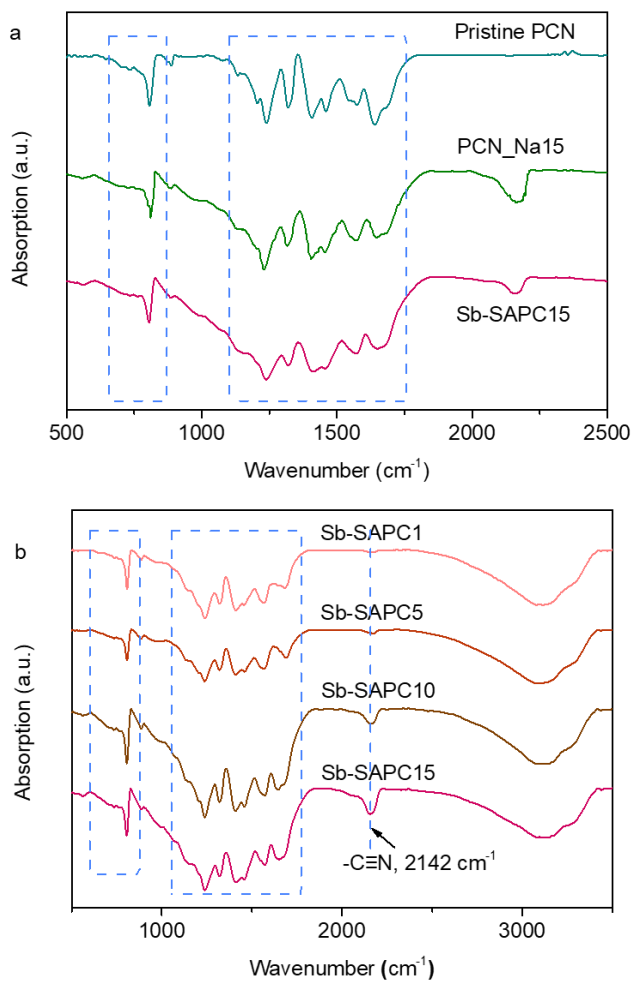
1104 **Supplementary Figure 23 | EELS spectra of CN samples. a,** pristine PCN. **b,** Sb-  
 1105 SAPC15 (batch 2). **c,** Sb-SAPC15 (batch 3).

1106

1107 No edge could be detected at energy range of 685-695 eV of these 3 spectra<sup>23</sup>, further  
 1108 suggesting no F in Sb-SAPC.

1109

1110



1111

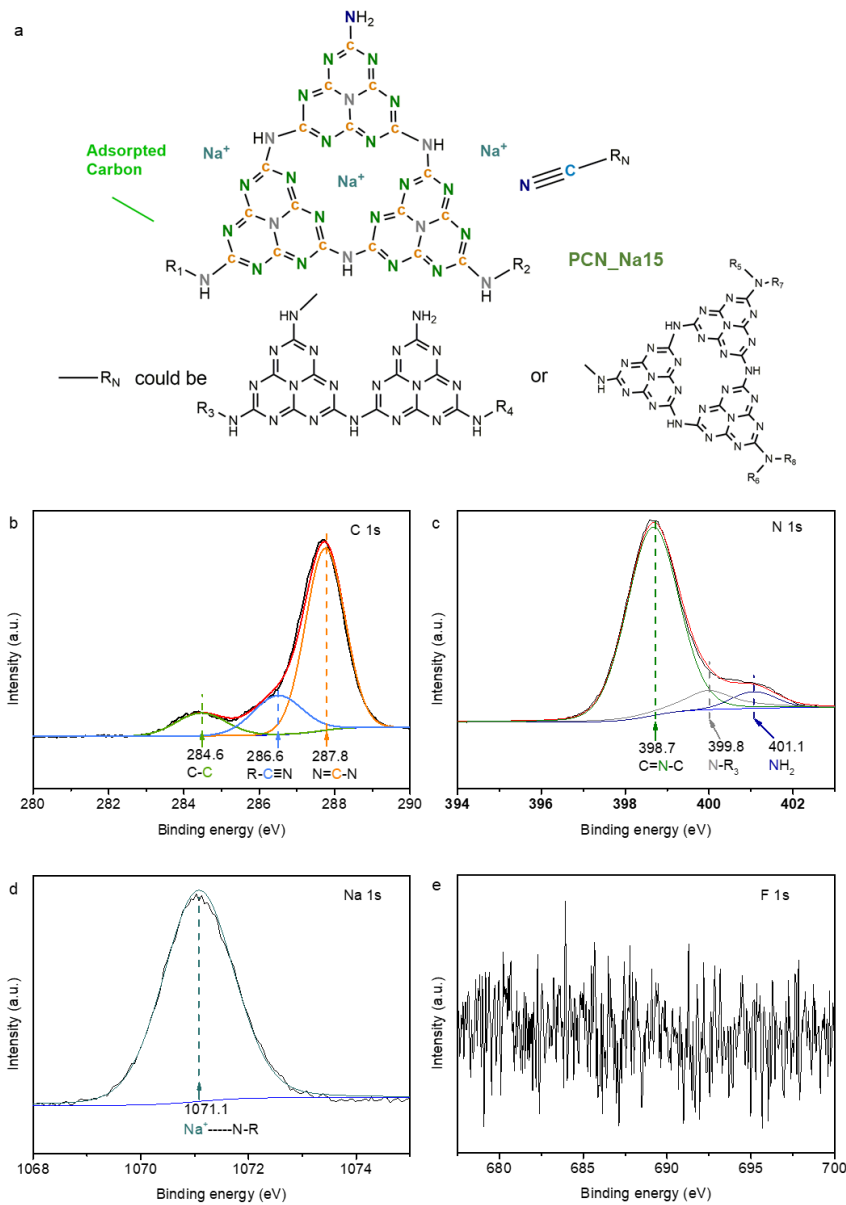
1112

1113

1114

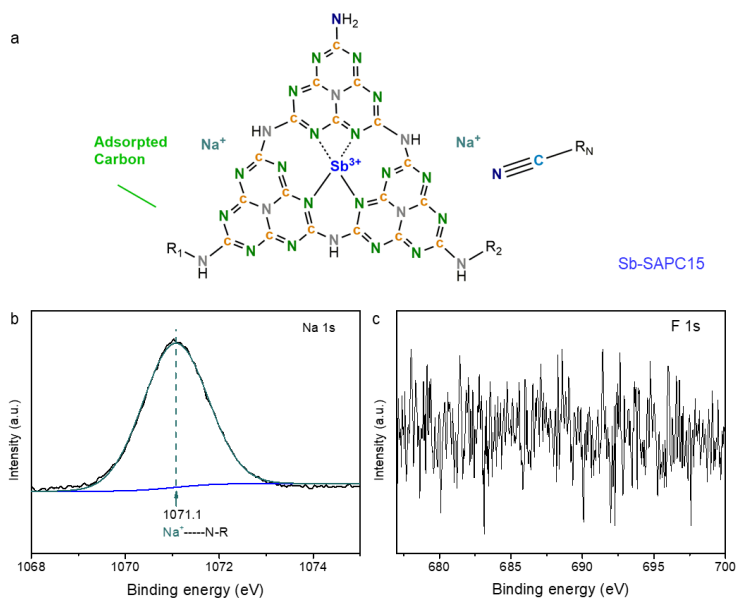
1115

**Supplementary Figure 24 | FT-IR spectra of PCN samples and Sb-SAPCs.** a, FT-IR spectra of pristine PCN, PCN\_Na15, and Sb-SAPC15. b, FT-IR spectra of Sb-SAPC1, Sb-SAPC5, Sb-SAPC10 and Sb-SAPC15.



1116  
1117  
1118  
1119  
1120  
1121

**Supplementary Figure 25 | Surface chemical states of PCN\_Na15.** **a**, Schematic diagram showing the chemical states of elements in PCN\_Na15. **b-e**, High-resolution XPS spectra of PCN\_Na15: C 1s (**b**); N 1s (**c**); Na 1s (**d**); and F 1s (**e**).



1122

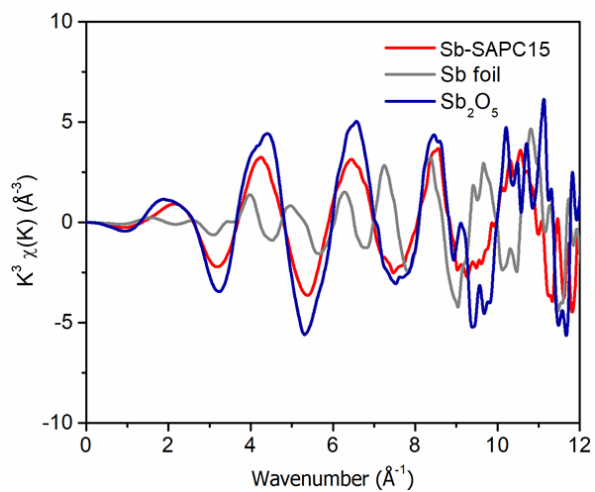
1123

1124

1125

1126

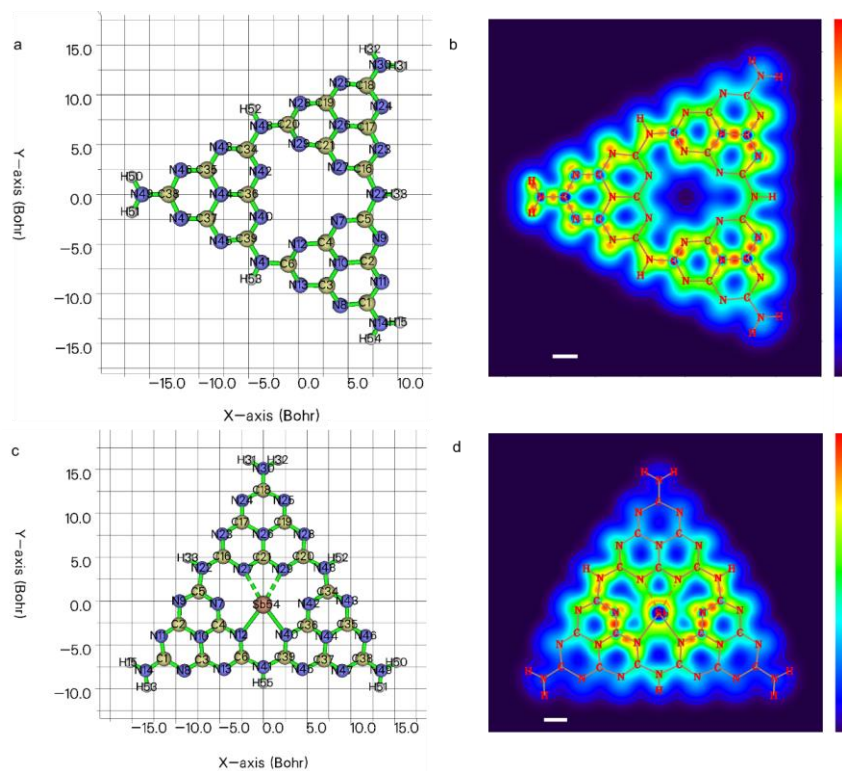
**Supplementary Figure 26 | Surface chemical states of Sb-SAPC15.** **a**, Schematic diagram showing the chemical states of elements in Sb-SAPC15. **b-c**, High-resolution XPS spectra of Sb-SAPC15: Na 1s (**b**) and F 1s (**c**).



1127

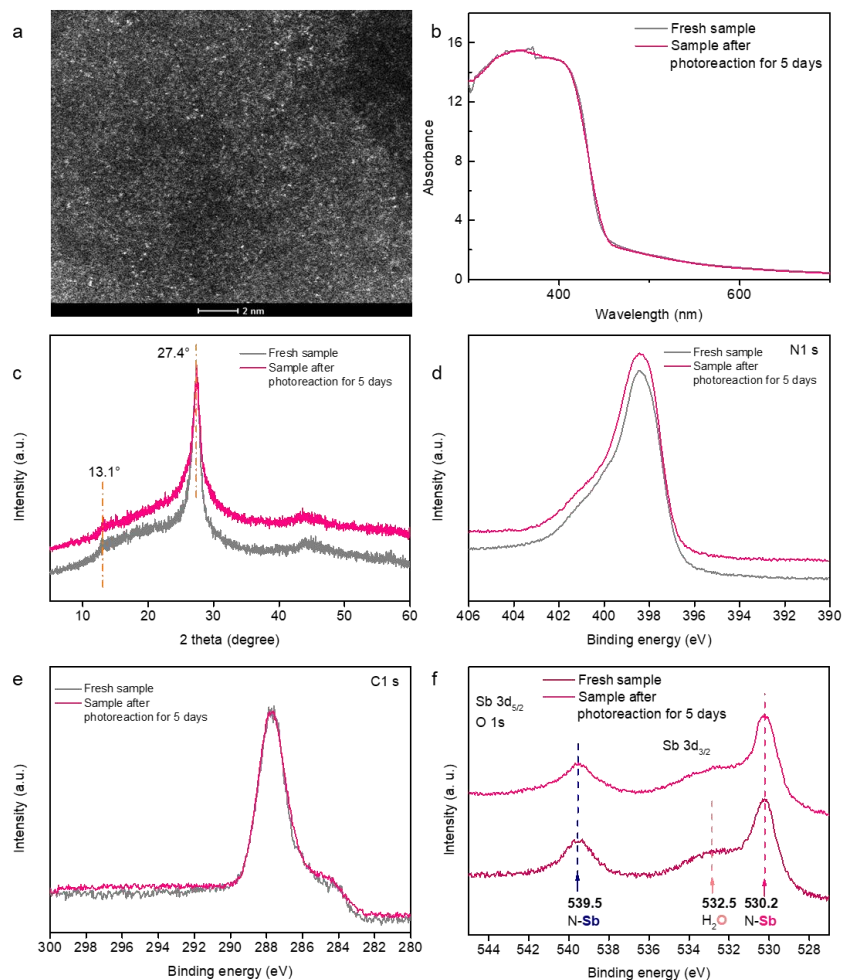
1128 **Supplementary Figure 27 | Extended X-ray absorption fine structure (EXAFS, k<sup>3</sup>-**  
1129 **weighted k-space) of Sb-SAPC15.** The spectrum of Sb-SAPC15 show a significant  
1130 difference compared with references spectra (Sb foil and Sb<sub>2</sub>O<sub>5</sub>).

1131



1132  
 1133 **Supplementary Figure 28 | Optimized geometry configuration and localized orbital**  
 1134 **locator of cluster models.** **a**, Optimized geometry configuration and atomic numbers of  
 1135 Melem\_3 to represent pristine PCN. **b**, Localized orbital locator calculated based on  $\pi$  MOs  
 1136 of melem\_3 (XY plane,  $Z = 0.45$  Bohr). **c**, Optimized geometry configuration and atomic  
 1137 numbers of melem\_3Sb3+ to represent Sb-SAPCs. **d**, Localized orbital locator calculated  
 1138 based on  $\pi$  MOs of melem\_3Sb3+ (XY plane,  $Z = 1.2$  Bohr). The dashed bonds refer to  
 1139 the weak interaction between N and Sb atoms. The scale bars in **(b)** and **(d)** are 5 Bohr.  
 1140 The maximum and minimum electronic density in **(b)** and **(d)** are 0.00 and 0.75.

1141  
 1142 As shown in Supplementary Figure 28c & d, the sum of occupied  $\pi$  MOs at N12 and  
 1143 N40 strongly interacts with that at Sb54, thus two strong covalent bonds can be formed.  
 1144 Additionally, the sum of occupied  $\pi$  MOs at N27 and N28 also interacts with that at Sb54.  
 1145 The summed electronic intensity between N27 and Sb54 (as well as N28 and Sb54) is  
 1146 slightly weaker than that between N12 and Sb54 (as well as N40 and Sb54), indicating the  
 1147 slightly weaker interaction between N27 and Sb54 (Supplementary Figure 28d). These  
 1148 results further manifest the best fitting result for the first shell that each Sb atom is  
 1149 coordinated with about 3.3 N atoms in average (Figure 2h).  
 1150

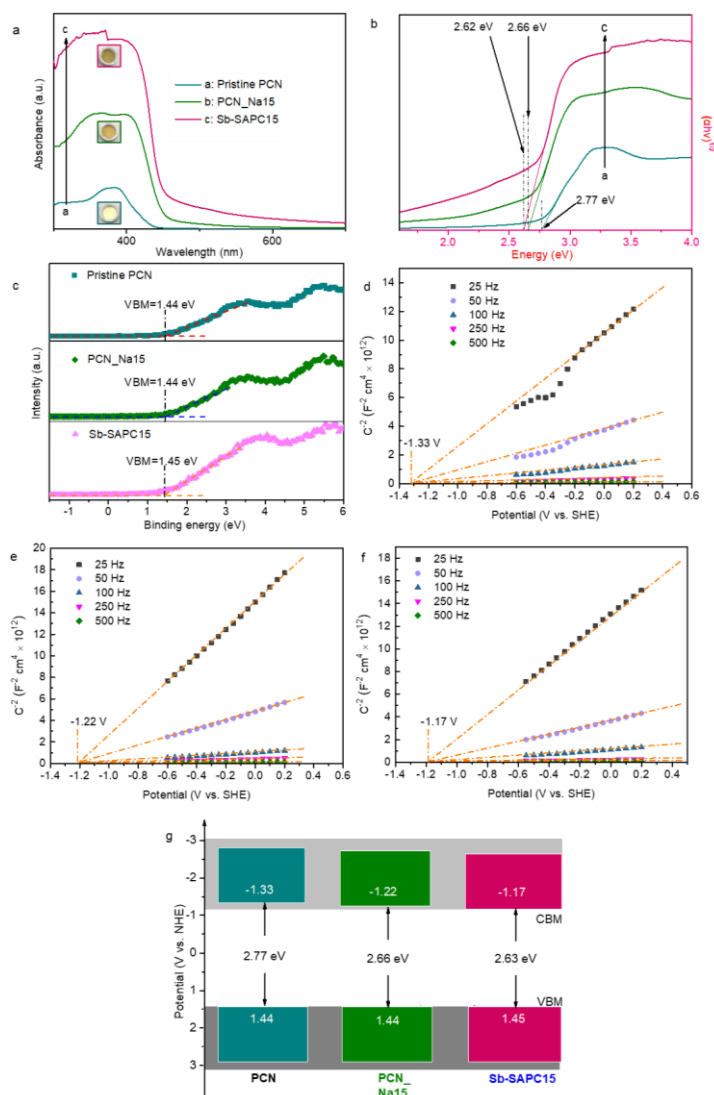


1151  
1152  
1153  
1154  
1155  
1156  
1157  
1158  
1159

**Supplementary Figure 29 | Post-characterization of Sb-SAPC15 after photocatalysis.**

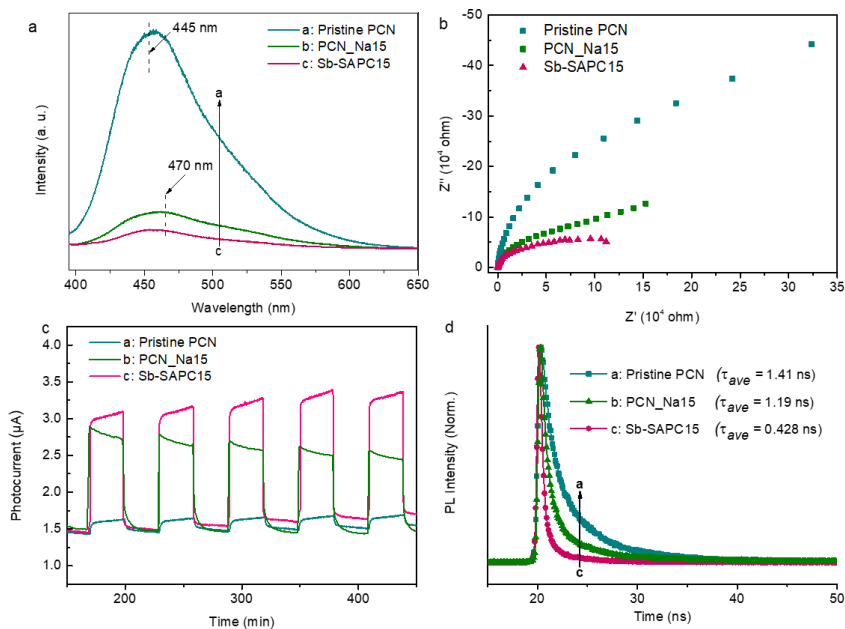
**a**, HAADF STEM image of Sb-SAPC15 after 5 days of photoreaction. **b-f**, Comparison of as-prepared Sb-SAPC15 and Sb-SAPC15 after 5 days of photoreaction: **(b)** UV-vis spectra; **(c)** XRD pattern; **(d)** high resolution XPS N 1s spectra; **(e)** high resolution XPS C 1s spectra; and **(f)** high resolution XPS O 1s and Sb 3d XPS spectra. After every 8 h of reaction, the reaction solution was exchanged by fresh 0.1 M phosphate buffer solution saturated with O<sub>2</sub>. Light intensity: 30.3 W m<sup>-2</sup> at 420-500 nm.





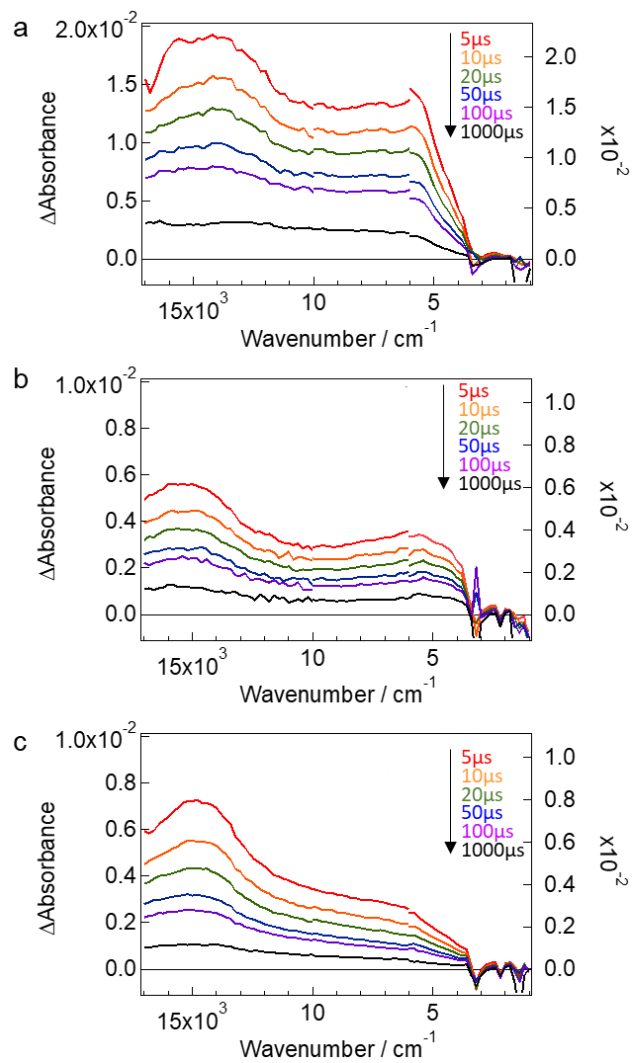
1160

1161 **Supplementary Figure 30 | Characterization of the CBM and VBM.** **a**, UV-vis diffuse  
 1162 reflection spectra of pristine PCN, PCN\_Na15 and Sb-SAPC15. **b**, Tauc plot of pristine  
 1163 PCN, PCN\_Na15 and Sb-SAPC15. **c**, Valence-band XPS spectra of pristine PCN,  
 1164 PCN\_Na15 and Sb-SAPC15. **d-f**, Mott Schottky plots of (d) pristine PCN, (e) PCN\_Na15  
 1165 and (f) Sb-SAPC15. **g**, Band structure diagrams of PCN, PCN\_Na15 and Sb-SAPC15. The  
 1166 Fermi level of the instrument (VB-XPS) is equilibrated at 4.5 eV utilizing Au metal basis as  
 1167 the reference. In this case, the numerical value of the binding energy in the calibrated VB-  
 1168 XPS spectrum is the same as the potential vs. normal hydrogen electrode.



1169  
 1170  
 1171  
 1172  
 1173  
 1174  
 1175  
 1176  
 1177  
 1178  
 1179  
 1180

**Supplementary Figure 31 | Evaluation of charge separation.** **a**, Photoluminescence spectra of PCN, PCN\_Na15 and Sb-SAPC15 at an excitation wavelength of 380 nm. **b**, Electrochemical impedance spectroscopy (EIS) spectra (Nyquist plots) of pristine PCN and Sb-SAPC15 in the frequency range from 100 kHz to 0.01 Hz at 0.6 V (vs. Ag/AgCl) under visible light irradiation. **c**, Comparison of photocurrent response between pristine PCN and Sb-SAPC15 at -0.6 V (vs. Ag/AgCl) under visible light illumination. The light source used in the EIS and photocurrent measurement is a Xe lamp with a UV cut ( $\lambda > 420$  nm) filter (light intensity at 420–500 nm:  $30.3 \text{ W m}^{-2}$ ). **d**, Time-resolved photoluminescence spectra of pristine PCN, PCN\_Na15 and Sb-SAPC15 recorded at 25 °C. The electrolyte used for the EIS and photocurrent measurement is 0.1 M phosphate buffer (pH = 7.4).



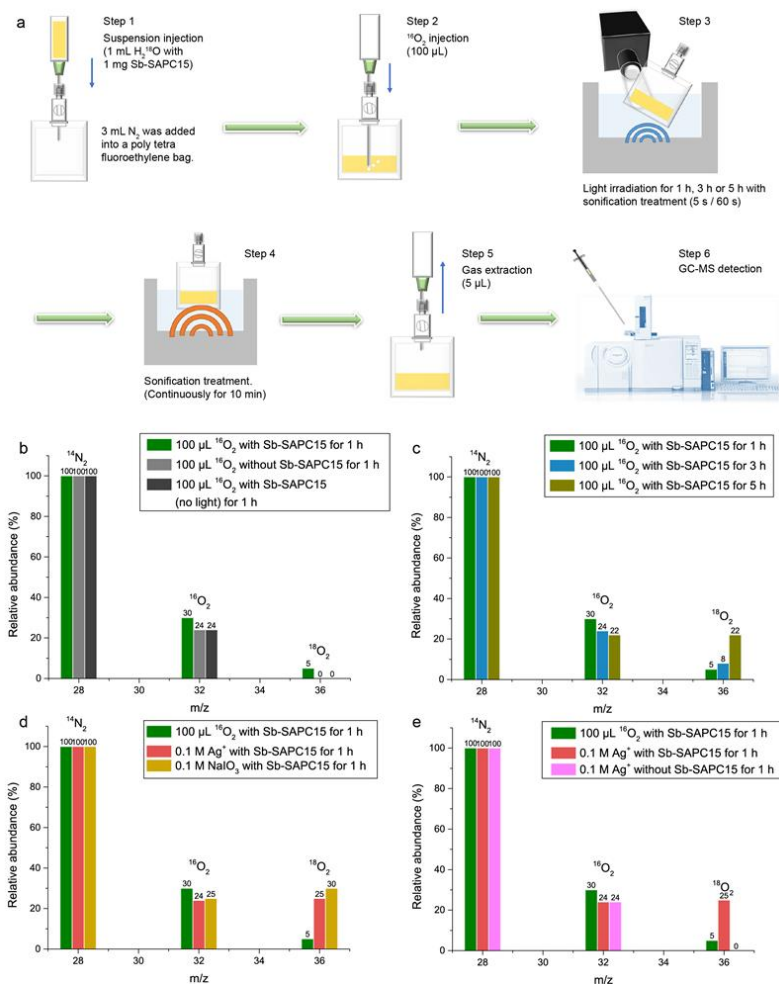
1181

1182 **Supplementary Figure 32 | Transient infrared red (IR) absorption spectra. a-c,**

1183 Transient IR absorption spectra for PCN (a), PCN\_Na15 (b) and Sb-SAPC15 (c) evolved

1184 after 420 nm laser pulse excitation under vacuum (6 ns, 5 mJ, 5 Hz).

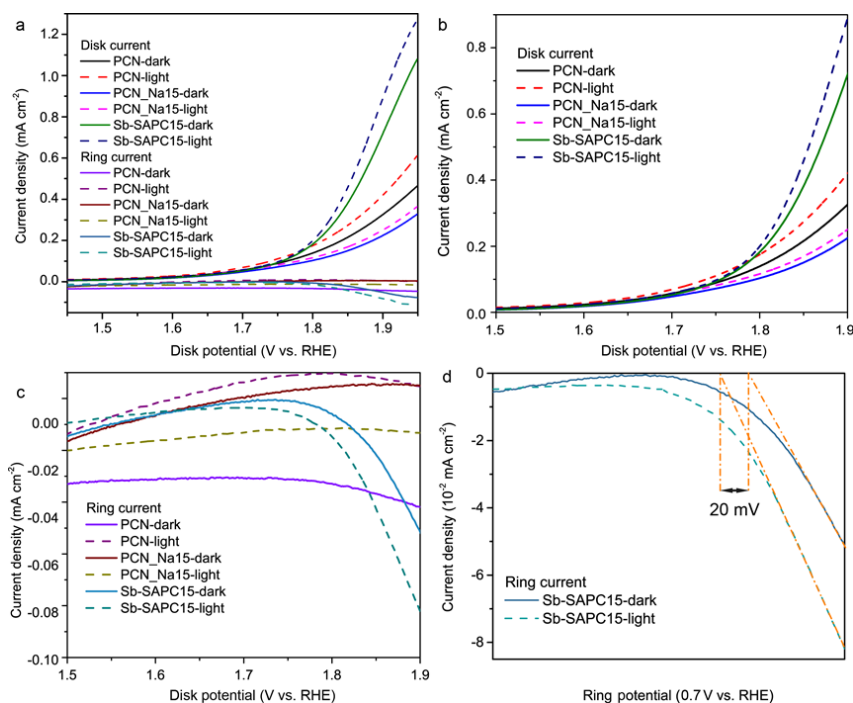
1185



1186  
1187  
1188  
1189  
1190  
1191  
1192  
1193  
1194  
1195  
1196  
1197  
1198  
1199

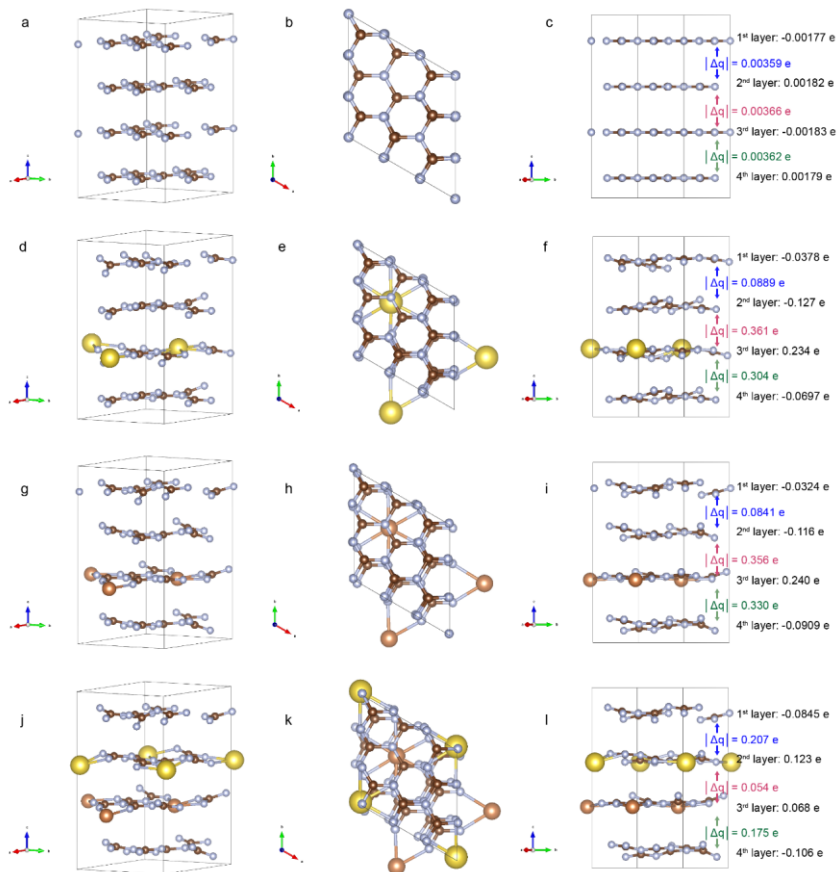
**Supplementary Figure 33 | Water oxidation mechanism. a**, Schematic diagram showing the isotopic experiment for H<sub>2</sub>O<sub>2</sub> production with addition of <sup>16</sup>O<sub>2</sub> as the electron acceptor and H<sub>2</sub><sup>18</sup>O as the electron donor (The figure of GC-MS in step 7 is taken from <https://www.an.shimadzu.co.jp/gcms/2010se.htm>). **b**, GC-MS spectra of the gas extracted from the Sb-SAPC15 system with <sup>16</sup>O<sub>2</sub> as the electron acceptor and H<sub>2</sub><sup>18</sup>O as the electron donor. Control experiments without addition of Sb-SAPC15 or without light irradiation were conducted for confirming the photo-induced oxygen generation reaction. **c**, GC-MS spectra of the gas extracted from the Sb-SAPC15 system after Xenon lamp illumination of 1 h, 3 h and 5 h in step 3. **d**, GC-MS spectra of the gas extracted from the Sb-SAPC15 system with different electron acceptors (100 μL O<sub>2</sub>, 0.1 M Ag<sup>+</sup> or 0.1 M NaIO<sub>3</sub>). **e**, GC-MS spectra of the gas extracted from the system with or without addition of Sb-SAPC in condition of adding different electron acceptors (100 μL O<sub>2</sub> or 0.1 M Ag<sup>+</sup>).

1200 With increasing irradiation time, the signal of  $^{18}\text{O}_2$  ( $m/z = 36$ ) gradually increased  
1201 (Supplementary Figure 33c). Additionally, we also investigated the oxygen generation with  
1202 addition of other electron acceptors (0.1 M  $\text{Ag}^+$  or 0.1 M  $\text{NaIO}_3$ ). The signal of  $^{18}\text{O}_2$  ( $m/z =$   
1203  $36$ ) significantly increased after addition of silver ion or  $\text{NaIO}_3$  compared to the case with  
1204 injection of 100  $\mu\text{L}$   $^{16}\text{O}_2$  (Supplementary Figure 33d), indicating that both of silver ion and  
1205  $\text{NaIO}_3$  could serve as efficient sacrificial reagent for oxygen evolution. To investigate whether  
1206 the  $\text{Ag}^+$  could directly produce oxygen or work as the sacrificial reagent, we conducted a  
1207 control experiment with  $\text{Ag}$  in solution. As shown in Supplementary Figure 33e, the signal  
1208 of  $^{18}\text{O}_2$  ( $m/z = 36$ ) could not be detected without the addition of photocatalyst, indicating  
1209 that pure  $\text{Ag}^+$  in the system could not produce  $\text{O}_2$ , which suggests that the  $\text{Ag}^+$  just serves  
1210 as a sacrificial reagent for photocatalytic WOR.  
1211



1212  
 1213  
 1214  
 1215  
 1216  
 1217  
 1218  
 1219  
 1220  
 1221  
 1222  
 1223  
 1224  
 1225

**Supplementary Figure 34 | The anodic polarization curves of rotating ring disk electrode modified by PCN, PCN\_Na15 and Sb-SAPC15 with or without light irradiation. a,** Comparison of the anodic polarization curves of the rotating ring disk electrode PCN, PCN\_Na15 and Sb-SAPC15 irradiated by light or in the dark condition. **b,** Anodic polarization curves of the rotating disk electrode PCN, PCN\_Na15 and Sb-SAPC15 in dark condition or with light irradiation. **c,** Anodic polarization curves of the ring electrode PCN, PCN\_Na15 and Sb-SAPC15 with light irradiation or in absence of light. **d,** Enlarged ring current of rotating ring disk electrode modified by Sb-SAPC15. The disk potential was shifted from 1.4 to 1.95 V (vs. RHE), and the potential of the ring was set at 0.7 V (vs. RHE). In this case, the signal of O<sub>2</sub> reduction to H<sub>2</sub>O (0.7 V vs. RHE) could be immediately captured by the ring electrode if O<sub>2</sub> was generated by water oxidation reaction. Solution: 0.1 M KOH aqueous solution (pH = 12.9).



1226

1227

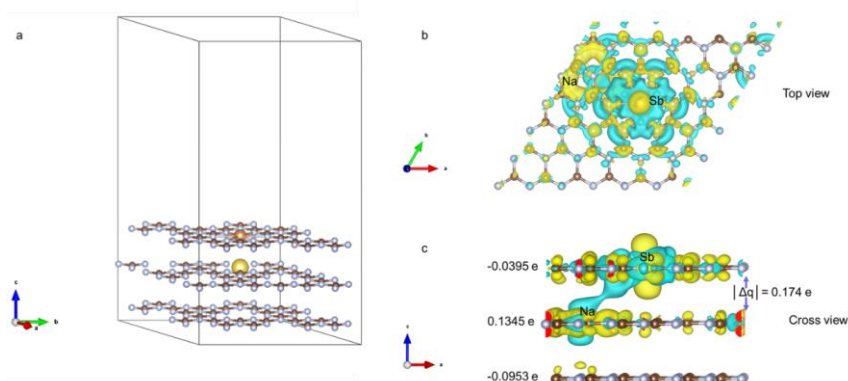
1228

1229

1230

1231

**Supplementary Figure 35 | Bader Charge distribution analysis from density functional theory (DFT) calculations. a-l, Charge distribution of pristine GCN (a-c), Na-GCN (d-f), Sb-GCN (g-i), and NaSb-GCN (j-l).  $|\Delta q|$  represents the absolute value of the difference of the electron distribution between the layers.**



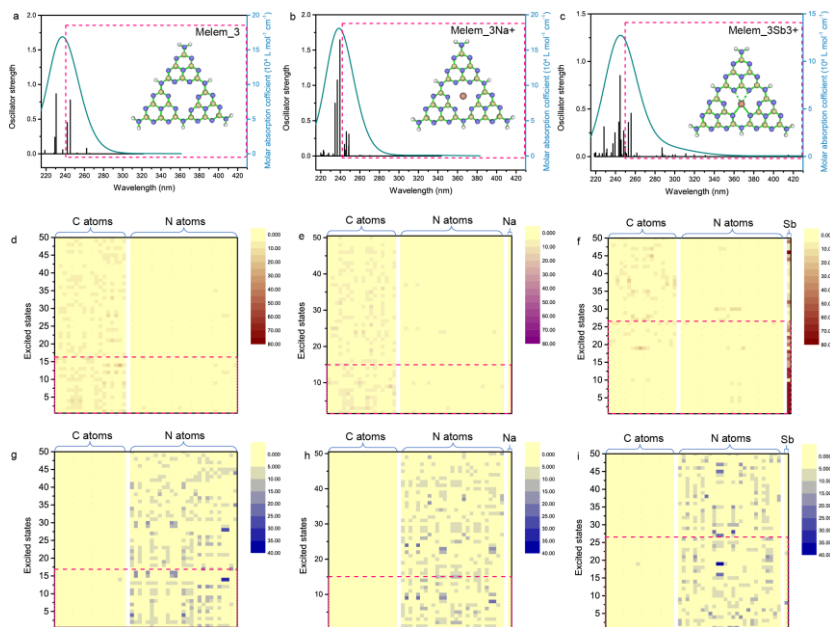
1232  
1233  
1234  
1235  
1236  
1237  
1238  
1239

**Supplementary Figure 36 | Charge distribution analysis near surface of NaSb-GCN from density functional theory (DFT) calculations.** **a**, Optimized near surface crystal structure of NaSb-GCN. **b-c**, Enlarged top view (**b**) and cross view (**c**) of NaSb-GCN.  $|\Delta q|$  represents the absolute value of the difference of electron distribution between the first and second layer. Yellow color represents electron accumulation and blue color represents electron depletion.

**Commented [TB61]:** \*\* Electronic structure calculations  
When electronic structure calculations are reported in the manuscript, the atomic coordinates of the optimized computational models should be provided. For molecular dynamics trajectories at least the initial and final configurations should be supplied. We encourage you to make them available by uploading the structures in any of the existing data repositories (see e.g. <https://www.nature.com/sdata/policies/repositories>). Alternatively, they can be supplied as a separate Supplementary Data file (ideally as a plain, unformatted text file).

**Commented [TB62R61]:** We have prepared the detailed file for providing the atomic coordinates of optimized computational models. Additionally, all .fchk and .log files for Time dependent measurement are provided. In this case, reader could readily do similar analysis for estimating charge separation by using as-proposed method.





1240

1241

1242

1243

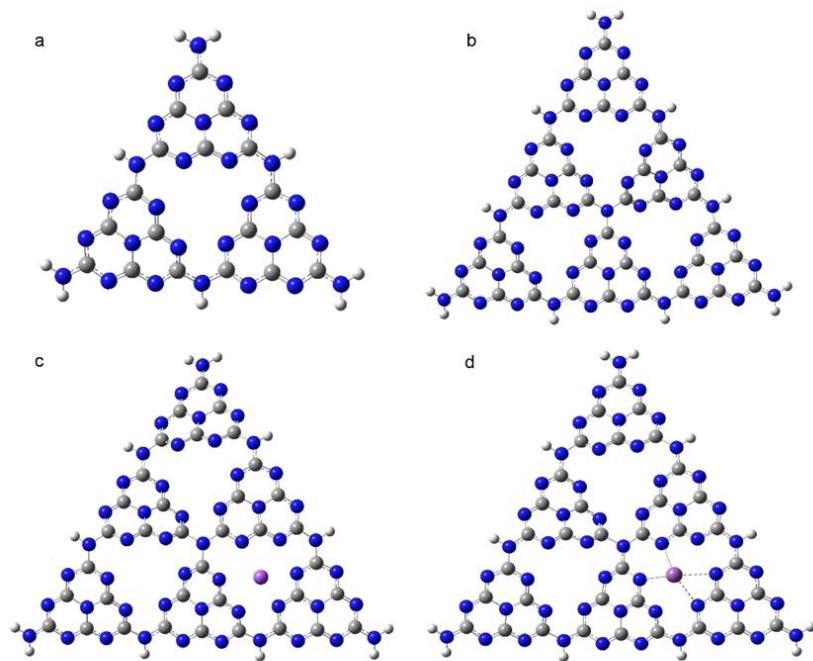
1244

1245

1246

1247

**Supplementary Figure 37 | Simulated excitation properties of Melem\_3, Melem\_3Na+ and Melem\_3Sb3+.** a-c, TDDFT-calculated absorption spectra for (a) Melem\_3, (b) Melem\_3Na+ and (c) Melem\_3Sb3+. d-i, The population of electron and hole distribution (vertical excitation at the excited states 1-50). (d) Electron distribution and (g) hole distribution for Melem\_3. (e) Electron distribution and (h) hole distribution for Melem\_3Na+. (f) Electron distribution and (i) hole distribution for Melem\_3Sb3+. The magenta dash circles are the excited states that possibly participate in the photocatalytic H<sub>2</sub>O<sub>2</sub> production.



Legends:

● a carbon atom ● a nitrogen atom ● a hydrogen atom ● a sodium atom ● an antimony atom

1248

1249

1250

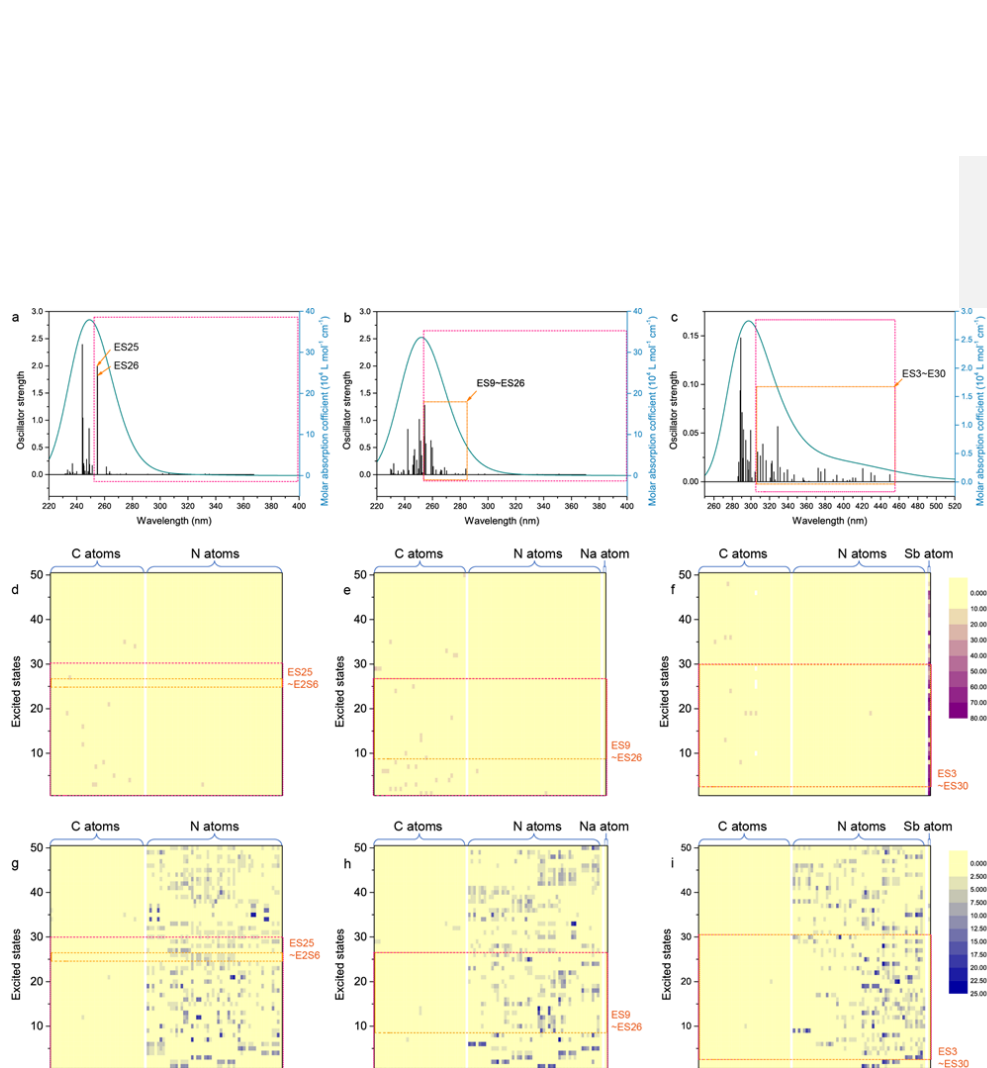
1251

1252

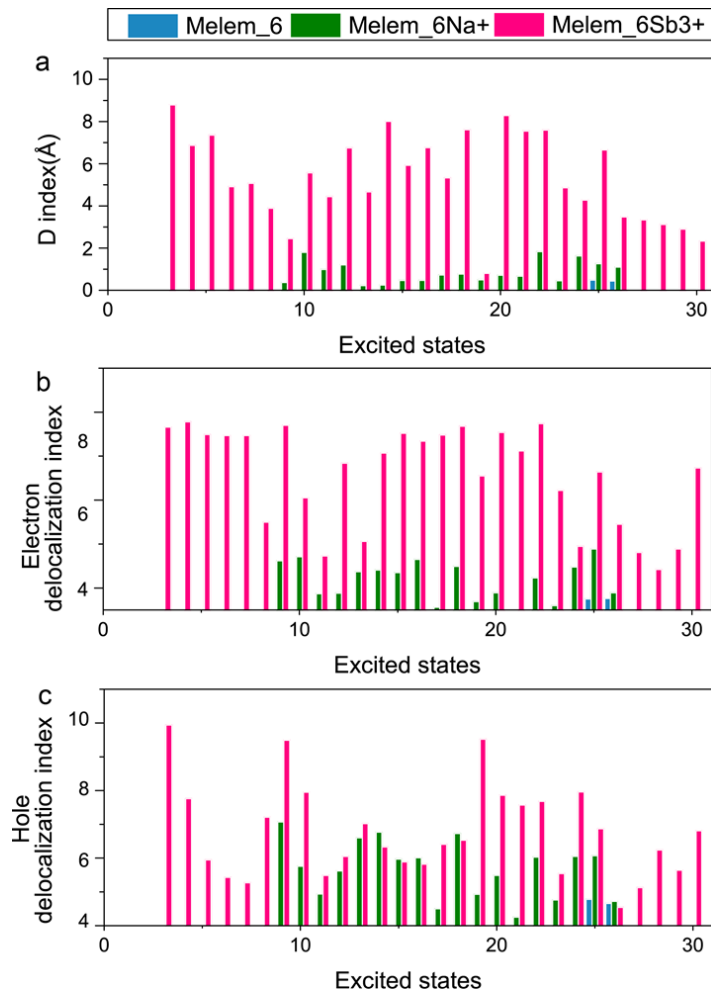
1253

1254

**Supplementary Figure 38 | Cluster models for investigating charge separation properties.** **a**, A cluster model for representing Melem\_3. **b**, Melem\_6 for representing PCN. **c**, Melem\_6Na<sup>+</sup> for representing sodium ion incorporated PCN. **d**, Melem\_6Sb<sup>3+</sup> for representing single atomic Sb incorporated PCN.

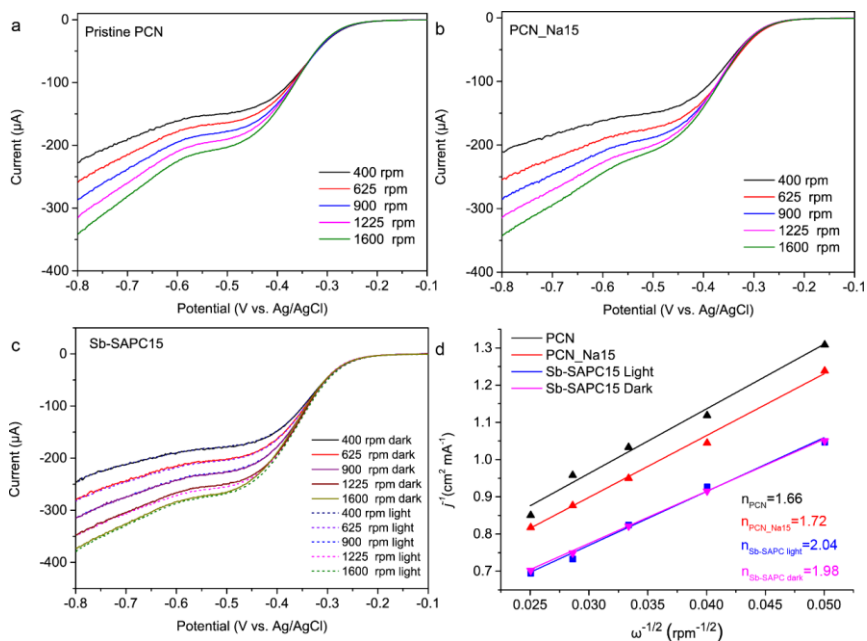


1256 **Supplementary Figure 39 | Simulated excitation properties of Melem\_6, Melem\_6Na+**  
 1257 **and Melem\_6Sb3+.** a-c, TDDFT-calculated absorption spectra for (a) Melem\_6, (b)  
 1258 Melem\_6Na+ and (c) Melem\_6Sb3+. d-i, The population of electron and hole distribution  
 1259 (vertical excitation at the excited states 1-50). (d) Electron distribution and (g) hole  
 1260 distribution for Melem\_6. (e) Electron distribution and (h) hole distribution for Melem\_6Na+.  
 1261 (f) Electron distribution and (i) hole distribution for Melem\_6Sb3+. The magenta dash  
 1262 circles are the excited states that possibly participate in the photocatalytic H<sub>2</sub>O<sub>2</sub> production.  
 1263 The orange dash circles represent the most important transitions that contribute the most  
 1264 for the spectra for photocatalytic H<sub>2</sub>O<sub>2</sub> production.  
 1265



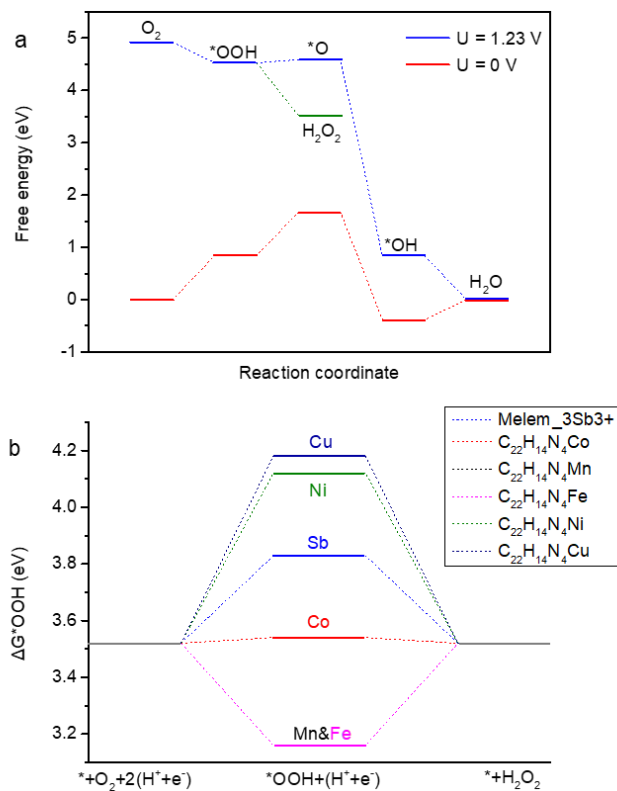
1266  
 1267  
 1268  
 1269  
 1270  
 1271  
 1272  
 1273  
 1274

**Supplementary Figure 40 | Simulated properties of Melem\_6, Melem\_6Na+ and Melem\_6Sb3+ for charge separation and the localization of electrons and holes. a,** *D index of the transitions of ES25 and ES26 of Melem\_6, ES9~ES26 of Melem\_6Na+ and ES3~ES30 of Melem\_6Sb3+.* **b-c,** *Delocalization index of (b) electrons and (c) holes for the transitions of ES25 and ES26 of Melem\_6, ES9~ES26 of Melem\_6Na+ and ES3~ES30 of Melem\_6Sb3+.*



1275  
1276  
1277  
1278  
1279  
1280  
1281  
1282

**Supplementary Figure 41 | Investigation of electron transfer numbers. a-b,** Linear sweep voltammetry (LSV) curves of pristine PCN (a) and Sb-SAPC15 (b) recorded on a rotating disk glassy carbon electrode in 0.1 M KOH saturated with  $\text{O}_2$  in dark condition. **c,** Linear sweep voltammetry (LSV) curves of Sb-SAPC15 recorded on a rotating disk glassy carbon electrode in 0.1 M KOH saturated with  $\text{O}_2$  under dark or visible light illumination. **d,** Koutecky–Levich plots (at -0.6 V vs. Ag/AgCl).



1283

1284

1285

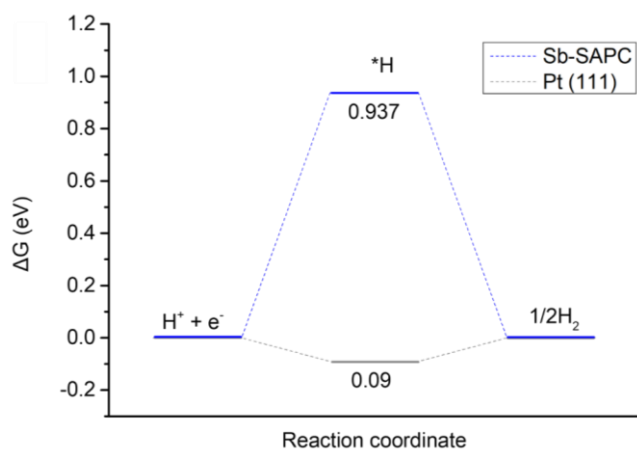
1286

1287

1288

1289

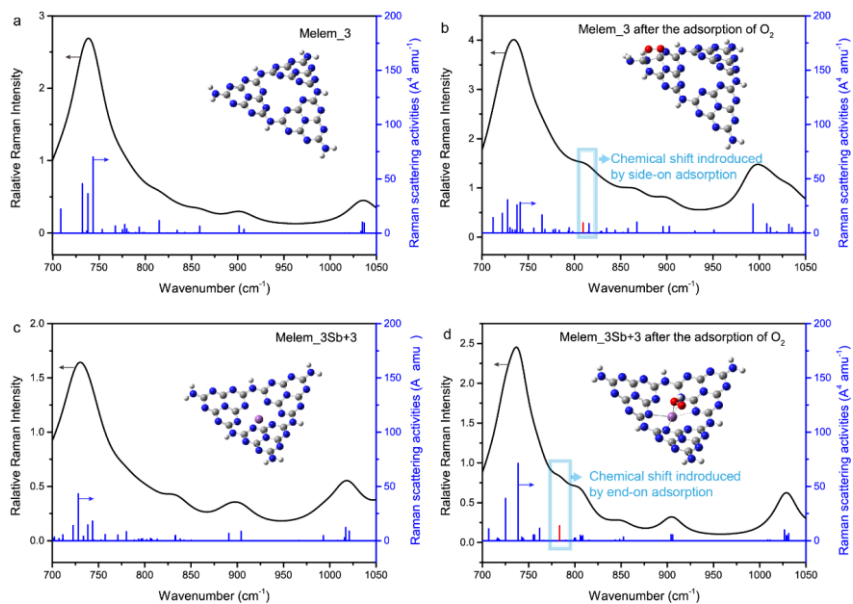
**Supplementary Figure 42 | Energetic diagram for ORR.** **a**, Calculated free energy diagrams at  $U = 0$  (blue line) and  $U = 1.23$  V (red line) vs. RHE for  $2e^-$  (green line) and  $4e^-$  ORR on Melem\_3Sb3+. **b**, Comparison of  $\Delta G^*_{OOH}$  for the  $2e^-$  ORR on Sb-SAPC15 and  $C_{40}H_{16}N_4M$ ,  $M = Mn, Fe, Co, Ni,$  and  $Cu$  at  $U = 0.7$  V vs. RHE. The free energy diagram of  $C_{40}H_{16}N_4M$  is adopted from our previous report<sup>2</sup>.



1290  
1291  
1292  
1293  
1294  
1295  
1296  
1297  
1298  
1299  
1300

**Supplementary Figure 43 | Interaction of hydrogen atoms and Sb sites and energetic diagram for HER.** Comparison of  $\Delta G_{\text{H}}$  for HER on Melem\_3Sb3+ and Pt (111).

The interaction of hydrogen atoms and Sb sites is weak for the following reasons: (1) A typical Sb-H bonding exists in  $SbH_3$ . The oxidation number of Sb in  $SbH_3$  is -3, whereas EXAFS fitting data shows that the chemical state of Sb sites in Sb-SAPC is close to +3. Thus, chemical bonding between Sb(+3) in Sb-SAPC and hydrogen is hardly believed. (2) The free energy diagram of Melem\_3Sb3+\*H is close to 1 eV, indicating that the adsorption of free H is quite hard on the Sb sites.

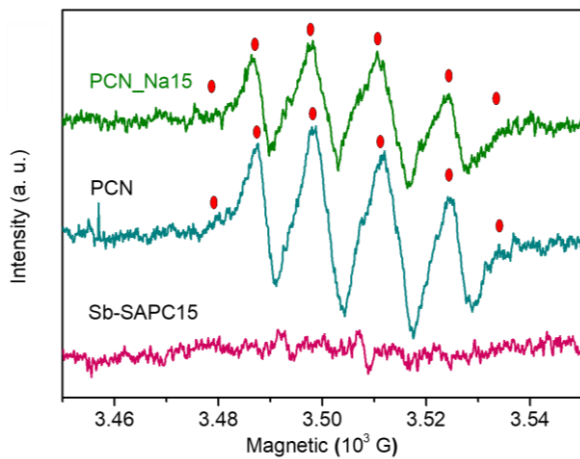


1301  
 1302  
 1303  
 1304  
 1305  
 1306  
 1307

**Supplementary Figure 44 | Calculated Raman shift by using the function of  $\omega_{97xd}$  at 6-311g(d) level. a-b**, Simulated Raman spectra for (a) the tri-s-triazine units and the units with (b)  $^{16}\text{O}-^{16}\text{O}$  side-on species. **c-d**, Simulated Raman spectra for (c) the Sb-sites and the units with (d)  $^{16}\text{O}-^{16}\text{O}$  end-on species. The white, gray, blue, red, and purple spheres represent H, C, N, O and Sb atoms, respectively.



1308



1309

1310

1311

1312

1313

**Supplementary Figure 45 | ESR spectra of PCN, PCN\_Na15 and Sb-SAPC15 recorded in methanol solution using 5,5-dimethyl-1-pyrroline N-oxide as a radical trapper.**

1314 **Supplementary Table 1. Activity comparison between Sb-SAPC15 and other**  
 1315 **reported photocatalysts and photoelectrodes for non-sacrificial H<sub>2</sub>O<sub>2</sub> production.**

Photocatalytic system	Concentration of photocatalyst	Irradiation condition	H <sub>2</sub> O <sub>2</sub> yield	AQE/ SCC efficiency	Ref.
g-C <sub>3</sub> N <sub>4</sub> /PDIx	1.7 mg mL <sup>-1</sup>	λ > 420 nm	50.6 μmol (48 h)	2.5% at 420 nm/ NA	[3]
g-C <sub>3</sub> N <sub>4</sub> /PDI/RGO	1.7 mg mL <sup>-1</sup>	λ > 420 nm	38 μmol (2 h)	6.1% at 420 nm/ 0.2%	[4]
Graphene oxide	0.32 mg mL <sup>-1</sup>	λ > 420 nm	1.4 μmol (6 h)	NA/ NA	[5]
Si/TiO <sub>2</sub> -Au	-----	λ = 365 nm	40 μmol (75 h)	NA/ NA	[6]
TiO <sub>2</sub> -Pt	0.05 mg mL <sup>-1</sup>	Full spectrum	5.096 μmol (1 h)	NA/ NA	[7]
g-C <sub>3</sub> N <sub>4</sub> /MTI	1.7 mg mL <sup>-1</sup>	λ > 420 nm	27.5 μmol (24 h)	6.1% at 420 nm/ 0.18%	[8]
g-C <sub>3</sub> N <sub>4</sub> /PDI-BN-RGO	1.7 mg mL <sup>-1</sup>	λ > 420 nm	34 μmol (24 h)	7.3% at 420 nm/ 0.28%	[9]
Resorcinol-formaldehyde resins	1.7 mg mL <sup>-1</sup>	λ > 420 nm	99 μmol (24 h)	7.5% at 450 nm/ 0.5%	[1]
<b>Sb-SAPC15</b>	<b>2 mg mL<sup>-1</sup></b>	<b>λ &gt; 420 nm</b>	<b>470.5 μmol (8 h)</b>	<b>17.6% at 420 nm/ 0.61%</b>	<b>This work</b>

1316  
 1317

1318 **Supplementary Table 2. Mass percentage of Sb in Sb-SAPCx.**

	Na mass percentage (%)	Substance amount of Na in 1 g catalyst (mmol)	Mass percentage of Sb (%)	Substance amount of Sb in 1 g catalyst (mmol)
PCN	0	0.00	0	0.00
PCN_Na15	2.00	0.87	0	0.00
Sb-SAPC0.5	0.08	0.03	0.63	0.05
Sb-SAPC1	0.16	0.07	0.96	0.08
Sb-SAPC3	0.44	0.19	2.28	0.19
Sb-SAPC5	0.72	0.31	4.31	0.36
Sb-SAPC10	1.18	0.51	7.85	0.65
Sb-SAPC15	1.51	0.66	10.88	0.90
PCN_Na15W*	2.01	0.87	0	0
Sb-SAPC15W*	1.50	0.65	10.85	0.89

1319 \* PCN\_Na15W and Sb-SAPC15W indicate the samples washed by hot water (90 °C)  
1320 for another 24 h.

1321

1322 We have tried to wash the as-prepared Sb-SAPC15 by hot water (90 °C) for  
1323 extremely long time (24 hours) in order to remove the alkaline ions in the CN matrix<sup>10</sup>.  
1324 However, the ICP result showed that the Na content kept almost constant after this  
1325 treatment. The difficulty of removing Na in PCN by washing could be due to its  
1326 existence nature. As revealed in the simulations based on DFT (both cluster model  
1327 and periodic model), sodium tends to bond onto the matrix of PCN. However, the  
1328 introduction of Na into PCN only slightly enhanced its photocatalytic activity.

1329

1330

1331

1332

1333

**Supplementary Table 3. Elemental analysis.**

Sample name	N %	C %	H %	Mass <sub>C</sub> /Mass <sub>N</sub>
PCN	60.7	33.7	2.01	55.5%
PCN_Na15	57.5	33.1	1.70	57.5%
Sb-SAPC1	59.5	33.1	1.90	55.7%
Sb-SAPC5	56.8	31.7	1.78	55.8%
Sb-SAPC10	54.0	30.3	1.66	56.2%
Sb-SAPC15	49.6	28.5	1.61	57.5%
Sb-SAPC20	45.5	26.9	1.57	59.1%

1334

1335

1336 **Supplementary Table 4. Fitting parameters of EXAFS data.**

Sample	Shell	N	R/Å	$\Delta E$	Debye-Waller factor $\sigma^2$ (Å <sup>2</sup> )	R-factor
Sb <sub>2</sub> O <sub>5</sub>	Sb-O	4.2±0.20	1.96±0.007	7.85±1.04	0.003±0.001	0.02
Sb-SAPC	Sb-N	3.3±0.20	2.0±0.03	9.74±0.94	0.002±0.0009	0.018

1337 Shell: scattering pathway; N: coordination number; R: bond distance;  $\Delta E$ : the inner  
1338 potential correction. The obtained XAFS data was processed in Athena (version 0.9.25) for  
1339 background, pre-edge line and post-edge line calibrations. The data range adopted for  
1340 data fitting in k-space and R space are 3-11.5 Å<sup>-1</sup> and 1-3 Å, respectively.  
1341

1342 **Supplementary Table 5. Excitation properties based on the wavefunctions of**  
 1343 **Melem\_3.**

	Molecule orbital contribution (Hole)			Molecule orbital contribution (Electron)			Molecule orbital contribution (Hole)			Molecule orbital contribution (Electron)			
S0→S1	MO	151	14.071%	MO	154	68.397%	S0→S9	MO	138	16.530%	MO	154	51.954%
	MO	152	27.839%	MO	155	14.459%		MO	143	22.826%	MO	155	17.193%
	MO	153	50.968%	MO	157	6.912%		MO	145	9.484%	MO	156	8.394%
S0→S2	MO	151	28.569%	MO	154	18.080%	S0→S10	MO	137	19.313%	MO	154	29.615%
	MO	152	15.441%	MO	155	62.993%		MO	138	11.299%	MO	155	37.942%
	MO	153	48.866%	MO	157	9.812%		MO	150	11.187%	MO	160	7.391%
S0→S3	MO	151	37.218%	MO	154	37.462%	S0→S11	MO	151	36.625%	MO	154	33.124%
	MO	152	37.269%	MO	155	37.027%		MO	152	15.992%	MO	155	14.635%
	MO	153	17.695%	MO	157	13.292%		MO	153	26.999%	MO	156	27.816%
S0→S4	MO	150	47.527%	MO	154	20.177%	S0→S12	MO	151	3.065%	MO	155	34.473%
	MO	151	8.132%	MO	155	57.173%		MO	152	34.192%	MO	156	33.596%
	MO	152	9.408%	MO	156	11.088%		MO	153	35.353%	MO	162	11.681%
S0→S5	MO	146	16.036%	MO	154	39.300%	S0→S13	MO	151	26.303%	MO	154	23.953%
	MO	149	15.260%	MO	155	32.108%		MO	152	7.807%	MO	155	18.083%
	MO	150	20.259%	MO	156	10.911%		MO	153	40.502%	MO	156	36.970%
S0→S6	MO	146	7.248%	MO	154	44.219%	S0→S14	MO	138	22.850%	MO	154	44.924%
	MO	148	33.220%	MO	155	23.903%		MO	141	33.109%	MO	157	12.639%
	MO	149	13.611%	MO	157	7.874%		MO	142	18.279%	MO	158	29.103%
S0→S7	MO	136	13.136%	MO	154	37.571%	S0→S15	MO	140	22.905%	MO	154	16.970%
	MO	143	6.749%	MO	155	28.780%		MO	142	26.607%	MO	155	33.323%
	MO	150	30.250%	MO	160	7.516%		MO	152	8.676%	MO	157	21.247%
S0→S8	MO	136	13.859%	MO	154	40.885%	S0→S16	MO	140	33.930%	MO	155	33.086%
	MO	137	17.967%	MO	155	29.284%		MO	141	24.611%	MO	157	28.433%
	MO	138	10.097%	MO	160	9.744%		MO	142	6.556%	MO	159	15.597%

1344  
 1345

1346 **Supplementary Table 6. Excitation properties based on the wavefunctions of**  
 1347 **Melem\_3Na+.**

	Molecule orbital contribution (Hole)			Molecule orbital contribution (Electron)			Molecule orbital contribution (Hole)			Molecule orbital contribution (Electron)			
S0→S1	MO	156	16.370%	MO	159	50.714%	S0→S9	MO	150	16.143%	MO	159	32.219%
	MO	157	28.906%	MO	160	28.431%		MO	151	14.245%	MO	160	18.088%
	MO	158	47.236%	MO	165	9.882%		MO	152	23.079%	MO	162	16.494%
S0→S2	MO	156	28.665%	MO	159	28.572%	S0→S10	MO	150	17.206%	MO	159	24.905%
	MO	157	16.793%	MO	160	50.573%		MO	151	17.064%	MO	160	22.652%
	MO	158	47.059%	MO	165	9.935%		MO	152	15.489%	MO	165	17.995%
S0→S3	MO	156	38.540%	MO	159	36.710%	S0→S11	MO	151	19.316%	MO	154	33.124%
	MO	157	37.923%	MO	160	37.005%		MO	152	19.447%	MO	155	33.136%
	MO	158	16.787%	MO	165	13.014%		MO	153	8.630%	MO	156	14.383%
S0→S4	MO	147	15.135%	MO	159	37.061%	S0→S12	MO	143	9.834%	MO	159	28.788%
	MO	148	15.314%	MO	160	37.519%		MO	157	18.907%	MO	160	27.355%
	MO	151	8.723%	MO	161	13.147%		MO	158	10.371%	MO	161	18.108%
S0→S5	MO	148	13.833%	MO	159	24.221%	S0→S13	MO	142	9.828%	MO	159	27.347%
	MO	149	20.893%	MO	160	48.620%		MO	156	18.948%	MO	160	28.782%
	MO	152	12.584%	MO	161	10.043%		MO	158	10.349%	MO	161	18.116%
S0→S6	MO	147	14.340%	MO	159	49.006%	S0→S14	MO	141	10.630%	MO	159	28.119%
	MO	149	20.718%	MO	160	23.845%		MO	141	18.961%	MO	160	28.836%
	MO	152	12.348%	MO	161	10.014%		MO	142	16.524%	MO	161	16.263%
S0→S7	MO	145	15.746%	MO	159	28.623%	S0→S15	MO	141	10.658%	MO	159	28.819%
	MO	146	15.655%	MO	160	28.829%		MO	156	18.931%	MO	160	28.102%
	MO	158	15.053%	MO	162	10.142%		MO	158	16.474%	MO	161	16.249%
S0→S8	MO	150	14.208%	MO	159	16.990%							
	MO	151	15.924%	MO	160	33.282%							
	MO	152	23.405%	MO	162	16.511%							

1348

1349

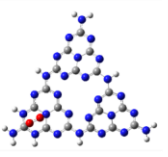
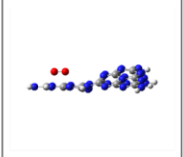

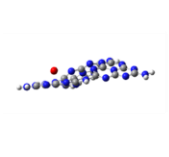
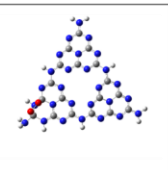
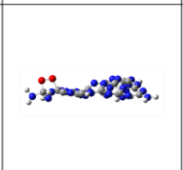
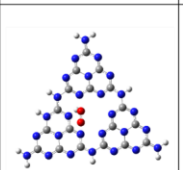
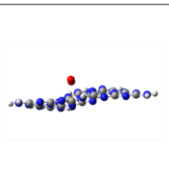
1350 **Supplementary Table 7. Excitation properties based on the wavefunctions of**  
 1351 **Melem\_3Sb3+.**

	Molecule orbital contribution (Hole)		Molecule orbital contribution (Electron)		Molecule orbital contribution (Hole)		Molecule orbital contribution (Electron)		
	MO 149	3.633%	MO 155	<b>99.112%</b>	MO 146	37.096%	MO 155	<b>40.942%</b>	
S0→S1	MO 151	65.610%			S0→S14	MO 153	11.569%	MO 156	27.918%
	MO 154	19.339%				MO 154	11.569%	MO 157	10.666%
	MO 149	17.637%	MO 155	<b>98.594%</b>		MO 141	11.460%	MO 155	<b>37.232%</b>
S0→S2	MO 151	13.214%			S0→S15	MO 151	23.242%	MO 156	20.075%
	MO 154	50.549%				MO 154	12.858%	MO 157	27.434%
	MO 150	12.440%	MO 155	<b>98.773%</b>		MO 147	10.948%	MO 155	<b>64.773%</b>
S0→S3	MO 152	17.901%			S0→S16	MO 148	37.814%	MO 156	6.228%
	MO 153	54.845%				MO 151	13.782%	MO 157	17.977%
	MO 144	7.421%	MO 155	<b>99.225%</b>		MO 146	20.726%	MO 155	<b>44.139%</b>
S0→S4	MO 150	32.476%			S0→S17	MO 151	11.805%	MO 156	27.976%
	MO 153	36.790%				MO 153	11.062%	MO 157	10.670%
	MO 141	32.952%	MO 155	<b>98.441%</b>		MO 141	18.967%	MO 155	<b>77.536%</b>
S0→S5	MO 145	32.842%			S0→S18	MO 142	35.504%	MO 156	5.924%
	MO 154	22.604%				MO 147	20.012%	MO 157	4.105%
	MO 143	12.371%	MO 155	<b>98.625%</b>		MO 147	10.237%	MO 157	55.007%
S0→S6	MO 150	11.062%			S0→S19	MO 148	83.253%	MO 163	5.986%
	MO 152	61.864%						MO 164	20.416%
	MO 141	9.700%	MO 155	<b>95.897%</b>		MO 139	14.951%	MO 155	<b>49.783%</b>
S0→S7	MO 145	31.267%			S0→S20	MO 146	25.432%	MO 156	20.017%
	MO 149	34.516%				MO 147	23.178%	MO 157	6.417%
	MO 139	7.962%	MO 155	<b>97.100%</b>		MO 146	36.714%	MO 155	<b>21.729%</b>
S0→S8	MO 143	23.509%			S0→S21	MO 147	41.974%	MO 156	31.893%
	MO 144	49.833%				MO 148	4.249%	MO 157	14.042%
	MO 143	37.403%	MO 155	<b>98.014%</b>		MO 139	16.928%	MO 155	<b>64.457%</b>
S0→S9	MO 144	28.745%			S0→S22	MO 140	24.402%	MO 156	15.844%
	MO 150	14.566%				MO 146	21.073%	MO 157	5.920%
	MO 152	9.902%	MO 155	8.267%		MO 145	19.544%	MO 155	<b>29.565%</b>
S0→S10	MO 153	22.497%	MO 156	26.006%	S0→S23	MO 151	8.865%	MO 156	28.095%
	MO 154	42.826%	MO 157	43.742%		MO 152	16.424%	MO 157	11.023%
	MO 145	12.654%	MO 155	<b>86.894%</b>		MO 138	38.207%	MO 155	<b>47.750%</b>
S0→S11	MO 148	41.191%	MO 156	4.160%	S0→S24	MO 153	8.226%	MO 156	12.316%
	MO 149	16.773%	MO 157	2.632%		MO 154	8.707%	MO 157	17.450%
	MO 142	38.982%	MO 155	<b>84.579%</b>		MO 146	21.944%	MO 155	<b>19.032%</b>
S0→S12	MO 146	6.215%	MO 156	5.009%	S0→S25	MO 147	24.951%	MO 156	12.536%
	MO 147	43.746%	MO 162	2.747%		MO 148	15.529%	MO 157	27.791%
	MO 139	20.544%	MO 155	<b>87.222%</b>		MO 137	21.180%	MO 155	<b>22.031%</b>
S0→S13	MO 140	27.510%	MO 156	4.259%	S0→S26	MO 146	35.194%	MO 158	20.115%
	MO 146	19.057%	MO 157	2.552%		MO 147	22.580%	MO 165	14.447%



1353 It is noteworthy that the absorption edge of simulated UV spectra as well as computed  
1354 optical gaps are usually larger than the experimental band gaps because of the following  
1355 two reasons: (1) To simulate the charge-transfer properties of the model with high qualities,  
1356 function of  $\omega$ 97xd, a function including large amount of Hartree–Fock exchange, was used.  
1357 These exchange functions usually overestimate the excitation energies, as well as the  
1358 simulated HOMO-LUMO gap; (2) In the solid state, p-conjugated molecules adjacent to the  
1359 one carrying a charge strongly polarize, an effect that stabilizes the cationic and anionic  
1360 states (each generally by about one eV in p-conjugated materials). In this case, the  
1361 experimental band gap is typically considerably smaller in energy than the calculated  
1362 molecular fundamental gap, as well as the calculated optical gap<sup>11</sup>. Since the system error  
1363 cannot be eliminated, the possible simulated ES that contributed to H<sub>2</sub>O<sub>2</sub> production  
1364 (corresponding to the spectra from 420 nm – 470 nm) were confirmed by comparing the  
1365 experimental spectra and simulated ones. Then, the transition density of electron/holes  
1366 was considered at all these ES.  
1367

1368 **Supplementary Table 8. Initial and optimized configuration for investigating the side-**  
1369 **on adsorption of O<sub>2</sub> on PCN surface.**

	Side-on adsorption of O <sub>2</sub> on Melem_3 (Site 1)		Side-on adsorption of O <sub>2</sub> on Melem_3 (Site 2)	
	Top view	Side view	Top view	Side view
Before optimization				
After optimization				

1370  
1371

1372 **Supplementary Notes 1: Probing WOR and ORR with low-concentration electron**  
1373 **acceptor**

1374 To calculate the H<sub>2</sub>O<sub>2</sub> generated from the Sb-SAPC system, we made the following  
1375 assumptions: (1) all added Ag<sup>+</sup> (4n mol) is consumed to provide holes to generate the initial  
1376 O<sub>2</sub> (n mol); (2) then, the Sb-SAPC reduces O<sub>2</sub> (n mol) to form H<sub>2</sub>O<sub>2</sub> (n mol) and  
1377 simultaneously oxidizes H<sub>2</sub>O (n mol) to generate fresh O<sub>2</sub> (1/2n mol); (3) the O<sub>2</sub> generated  
1378 in (2) keeps participating in the H<sub>2</sub>O<sub>2</sub> production and WOR to generate O<sub>2</sub> (1/4n, 1/8n,  
1379 1/16n... mol) until all O<sub>2</sub> is completely consumed. As a result, the amount of H<sub>2</sub>O<sub>2</sub> produced  
1380 by the initially generated O<sub>2</sub> can be calculated as follows:

1381 
$$n_{H_2O_2} = \sum_{k=1}^x n_{O_2} r^{k-1} = \frac{n_{O_2}(1-r^x)}{1-r} \quad (1)$$

1382 where  $n_{H_2O_2}$  is the generated amount of H<sub>2</sub>O<sub>2</sub>,  $n_{O_2}$  is the amount of generated O<sub>2</sub> by Ag<sup>+</sup>,  
1383  $r$  is 1/2,  $k$  is number of reaction cycles for simultaneous H<sub>2</sub>O<sub>2</sub> production and WOR. If the  
1384 initial O<sub>2</sub> generated by Ag<sup>+</sup> ( $k = 1$ ) was all consumed for H<sub>2</sub>O<sub>2</sub> production (i.e.,  $k$  equals to  
1385  $\infty$ ), the total amount of H<sub>2</sub>O<sub>2</sub> produced would be 2 times the amount of O<sub>2</sub> ( $k = 1$ ) and 1/2  
1386 times the amount of added Ag<sup>+</sup>. The constant concentration of H<sub>2</sub>O<sub>2</sub> was measured to be  
1387 0.032 mM with addition of 200 mg catalyst, 64% of the ideal value (0.05 mM) calculated  
1388 based on the initially added Ag<sup>+</sup> (0.1 mM). The 36% deficiency of H<sub>2</sub>O<sub>2</sub> could be due to the  
1389 reaction equilibrium of H<sub>2</sub>O<sub>2</sub> production<sup>9,12</sup> and the dissolved O<sub>2</sub> in aqueous solution (O<sub>2</sub>  
1390 solubility in pure water: 0.25 mM).

1391

1392 **Supplementary Notes 2: Investigation of synthesis process of Sb-SAPC**

1393 The synthesis of Sb-SAPC was first investigated to give a view of the structure of Sb-  
1394 SAPC. Sb-ethoxide was formed after dissolving NaSbF<sub>6</sub> in ethanol. After addition of  
1395 melamine, the lattice distance of the Sb-containing mixture was slightly increased. The  
1396 formed Sb-containing compound can be assigned to the Sb-melamine, verified by X-ray  
1397 diffraction (XRD, [Supplementary Figure 13a](#)) and X-ray photoelectron spectroscopy (XPS,  
1398 [Supplementary Figures 14-15](#)). Then, thermal polymerization and removal of F element  
1399 were performed by calcination at 560 °C for 4 hours ([Supplementary Figure 16](#)).

1400 The calcination temperature was also investigated. Sb-SAPC5 (5 mmol of NaSbF<sub>6</sub>

**Commented [TB63]:** Please remove this numbering and integrated it into "Supplementary Note 1" etc..

**Commented [TB64R63]:** All numbering has been removed and integrated them into the "Supplementary Notes"

**Commented [TB65]:** \* Please number ALL Supplementary Equations sequentially as 1, 2, etc. – If mentioned in the text refer to them as "Supplementary Equation X" not "Equation X".

**Commented [TB66R65]:** We have numbered all Supplementary Equations sequentially. All of the Equations in the test has been revised to "Supplementary Equation X"

1401 mixed with 4 g of melamine were used as the precursor) was prepared at 520 °C and  
1402 560 °C (named as Sb-SAPC5\_520 and Sb-SAPC5\_560), respectively. As shown in  
1403 [Supplementary Figure 17a](#), the inner-panel diffraction of the (100) lattice completely  
1404 disappears in Sb-SAPC5\_520, and the inter-panel diffraction of PCN (002) lattice is also  
1405 significantly decreased in Sb-SAPC5\_560, while the crystalline structure of graphitic  
1406 carbon nitride maintains. Additionally, the F element cannot be completely eliminated by  
1407 heating at 520 °C, as shown in the XPS measurement ([Supplementary Figure 17b](#)). These  
1408 results imply that low calcination temperature cannot remove the F element in the PCN  
1409 matrix, leading to an incomplete polymerization of the graphitic carbon nitride<sup>13</sup>. Additionally,  
1410 the Sb-SAPC5\_520 shows much poorer photocatalytic activity toward H<sub>2</sub>O<sub>2</sub> production,  
1411 even worse than the pristine PCN ([Supplementary Figure 17c](#)). Therefore, Sb-SAPCs  
1412 prepared at 560 °C were used for further photocatalytic investigation.

1413

### 1414 **Supplementary Notes 3: Structure characterization**

1415 The crystalline structures of the as-prepared samples were examined by XRD and  
1416 HRTEM. XRD patterns of all Sb-SAPC samples show two characteristic peaks at about  
1417 27.6° and 13.1° ([Supplementary Figure 19](#)), which can be ascribed to the interlayer  
1418 stacking (002) and the inter planar structure packing (100) of tri-s-triazine units,  
1419 respectively<sup>14</sup>. The slight shift in the diffraction angle of the (002) peak for Sb-SAPC15 can  
1420 be attributed to the electrostatic repulsion between interlayers when positive ions are  
1421 incorporated into the PCN matrix. The intensities of these two peaks gradually decrease  
1422 when increasing the contents of precursors ([Supplementary Figure 19c](#)), indicating that  
1423 polymeric structure of melon/g-C<sub>3</sub>N<sub>4</sub> could be slightly influenced by the foreign ions<sup>15</sup>.  
1424 Although the long-range order of the (002) and (100) lattices significantly decreases, these  
1425 two lattices can still be observed even when the content of ions reaches as high as 20  
1426 mmol. To further investigate whether the pristine structure is changed after the ion  
1427 incorporation, high-resolution TEM measurements of the exfoliated Sb-SAPC were  
1428 conducted (as shown in [Supplementary Figure 20](#)). The (100) inter planar structure  
1429 packing of the tri-s-triazine units can be readily observed, and the lattice distance is  
1430 determined to be 6.81 Å, which is in accordance with the XRD results. Thus, the crystalline

1431 structure of melon can be well preserved in Sb-SAPC.

1432

#### 1433 **Supplementary Notes 4: Influence of the -C≡N group**

1434 FT-IR ([Supplementary Figure 24a](#)) and XPS measurements reveal the existence of -  
1435 C≡N groups in both PCN\_Na15 and Sb-SAPC15. The interrelationship between -C≡N  
1436 groups and cations in carbon nitride matrix was investigated. As shown in [Supplementary](#)  
1437 [Figure 24a](#), the absorption band around the wavenumber of 2180 cm<sup>-1</sup> in the spectrum of  
1438 PCN\_Na15 is slightly stronger than that in the spectrum of Sb-SAPC15, manifesting the  
1439 larger content of -C≡N groups in PCN\_Na15. To investigate the influence of the cation  
1440 content on the formation of -C≡N groups, ICP measurements were performed. As shown  
1441 in [Supplementary Table 2](#), the Na amount in PCN\_Na15 (0.87 mmol per gram) and Sb-  
1442 SAPC15 (0.66 mmol per gram) are close, while PCN\_Na15 contains no Sb species.  
1443 Additionally, the ratios of the integration areas from the deconvoluted peaks at 288.1 and  
1444 286.5 eV are similar in the high-resolution XPS spectra of PCN\_Na15 (0.268) and Sb-  
1445 SAPC15 (0.228). These results indicate that the introduction of Sb sites into PCN has little  
1446 influence on the formation of -C≡N groups, and the -C≡N group formation could be possibly  
1447 due to the incorporation of alkaline metal ions<sup>10</sup>. These results are also in accordance with  
1448 the proposed synthesis mechanism ([Supplementary Figure 1](#)) and the EXAFS fitting  
1449 results.

1450 Several studies have reported that the -C≡N is an electron-withdrawing group that may  
1451 significantly enhance the charge separation, and thus improve the photocatalytic activity<sup>10</sup>.  
1452 <sup>15-17</sup>. To clarify the influence of -C≡N groups and Sb species on charge separation and  
1453 photocatalytic activity, a comprehensive investigation has to be carried out by comparing  
1454 the photocatalytic performance of Sb-SAPC15 and PCN\_Na15. As clarified in the previous  
1455 paragraph, the Na ion content in Sb-SAPC15 is similar to that in PCN\_Na15, giving a  
1456 similar -C≡N content. But Sb-SAPC15 exhibits a much higher photocatalytic activity ([Figure](#)  
1457 [1c](#) and [Supplementary Figure 9b](#)), suggesting the crucial function of the Sb species for  
1458 photocatalysis. Additionally, the photoluminescence intensity of PCN\_Na15  
1459 ([Supplementary Figure 31a](#)) is weaker as compared to that of pristine PCN, indicating that  
1460 the charge recombination can be effectively suppressed by introducing the -C≡N groups.

1461 In the case of Sb-SAPC15, the introduction of Sb species can further decrease the  
1462 photoluminescence intensity, manifesting that the radiative recombination is suppressed.  
1463 The TRPL spectrum also shows the similar phenomenon, i.e. lifetime of the charge carriers  
1464 in Sb-SAPC15 (0.428 ns) is shorter than that in PCN\_Na15 (1.41 ns), indicating that non-  
1465 radiative recombination is facilitated in Sb-SAPC15.

1466

#### 1467 **Supplementary Notes 5: Post characterization and investigation for catalyst** 1468 **poisoning**

1469 The HAADF STEM image of Sb-SAPC15 after 5 days of photoreaction shows that the  
1470 Sb sites remain atomically dispersed ([Supplementary Figure 29a](#)). The UV-vis spectra  
1471 show that the light absorption property of Sb-SAPC15 was hardly influenced by the  
1472 continuous photoreaction ([Supplementary Figure 29b](#)). The XRD pattern indicates that the  
1473 crystallinity of Sb-SAPC15 hardly changed after 5 days of photoreaction. Note that both  
1474 diffractions at 13.1° and 27.4° are clearly observable, indicating that the PCN structure in  
1475 Sb-SAPC15 was well maintained after long-term photoreaction ([Supplementary Figure](#)  
1476 [29c](#)). High-resolution N 1s, C 1s, O 1s and Sb 3d XPS spectra show that the chemical  
1477 states of N, C, O and Sb on the surface of Sb-SAPC15 were hardly influenced by the long-  
1478 time photoreaction ([Supplementary Figure 29d-f](#)). The surface oxidation of CN and Sb  
1479 were not observed. All of the above results demonstrate the excellent photocatalytic  
1480 stability of Sb-SAPC15.

1481 The maximum H<sub>2</sub>O<sub>2</sub> concentration after 8 h of photocatalytic reaction is approximately  
1482 0.016 wt.% of H<sub>2</sub>O<sub>2</sub>. Thus to further investigate whether catalyst poisoning occurred on the  
1483 surface of the catalyst, the photocatalytic activity was measured after soaking the as-  
1484 prepared Sb-SAPC15 catalyst in different concentrations of H<sub>2</sub>O<sub>2</sub> solution (ranging from  
1485 0.01 wt.% to 1 wt.%) for 8 h. The photocatalytic activity of Sb-SAPC15 showed no obvious  
1486 decay after being soaked in different concentrations of H<sub>2</sub>O<sub>2</sub> solution for 8 h. This result  
1487 indicates insignificant catalyst poisoning during our photocatalytic H<sub>2</sub>O<sub>2</sub> production process.

1488

#### 1489 **Supplementary Notes 6: Optical properties and action spectra**

1490 As shown in the insert to [Supplementary Figure 30a](#), Sb-SAPC15 displays a deep

1491 yellow color, darker than the pale yellow color of pristine PCN and PCN\_Na15. To  
1492 determine the precise band positions of these samples, UV-vis spectroscopy, Mott-  
1493 Schottky and valence band XPS measurements were conducted to obtain the bandgap  
1494 width, CBM and VBM, respectively. As shown in [Supplementary Figure 30a-b](#), the light  
1495 absorption ( $\lambda < 450$  nm) of Sb-SAPC15 significantly enhances compared with that of  
1496 PCN\_Na15 and pristine PCN, possibly due to changes in electronic states resulted from  
1497 Sb incorporation. Tauc plots of pristine PCN, PCN\_Na15 and Sb-SAPC15 indicate that the  
1498 bandgap almost keeps constant after introducing Sb and/or Na ions. VB-XPS results show  
1499 that the VBM of PCN\_Na15 and Sb-SAPC15 keep almost the same ( $\sim 1.45$  eV) to that of  
1500 PCN ([Supplementary Figure 30c](#)). Mott-Schottky plots reveal that the CBM slightly become  
1501 more positive from pristine PCN to PCN\_Na15 and to Sb-SAPC15 ([Supplementary Figure](#)  
1502 [30d-f](#)). By summarizing these results for band positions, we draw the band position  
1503 diagrams of these samples, as shown in [Supplementary Figure 30g](#).

1504 The action spectra of Sb-SAPC15 ([Figure 1c](#)) show that the apparent quantum yield  
1505 ( $\Phi_{AQY}$ ) agrees well with the absorption spectrum ([Supplementary Figure 30a](#)). The  
1506 absorption in the wavelength larger than 500 nm of Sb-SAPC15 could not contribute to the  
1507 production of  $H_2O_2$ . These results show that the VB-to-CB excitation of Sb-SAPC15 is  
1508 responsible for the  $H_2O_2$  production.

1509

#### 1510 **Supplementary Notes 7: Verification of WOR mechanism**

1511 OER occurred in our photocatalytic system for the following reasons:

1512 1) We have checked the water oxidation reaction by adding the electron acceptor of  
1513  $NaIO_3$  to make sure whether molecular oxygen could indeed be produced. As shown in  
1514 [Figure 1f](#), oxygen was gradually generated in the system of Sb-SAPC15, while neither  $O_2$   
1515 nor  $H_2O_2$  could be detected in the system of pristine PCN and PCN\_Na15.

1516 2) We have observed that the deeply trapped electrons (at  $5000\text{ cm}^{-1}$ ) in Sb-SAPC15  
1517 were significantly decelerated by TR-IR after addition of 20 Torr water ([Figure 3b](#)). This  
1518 result indicates that the photogenerated holes were consumed by water oxidation reaction  
1519 so that the lifetime of photogenerated electrons was significantly prolonged. In the case of  
1520 PCN and PCN\_Na15, the lifetime of photogenerated electrons kept almost the same

1521 (PCN\_Na15) or even decreased after addition of water into the system, indicating that the  
1522 photogenerated holes could barely participate in the water oxidation reaction. These  
1523 results confirm that the activity of water oxidation for Sb-SAPC is significantly higher than  
1524 that for PCN or PCN\_Na15.

1525 3) To further investigate the oxygen evolution reaction (OER), rotating ring-disk  
1526 electrode measurement was conducted. The anodic polarization curves of the rotating ring-  
1527 disk electrode modified by PCN, PCN\_Na15 and Sb-SAPC15 were recorded. As shown in  
1528 [Supplementary Figure 34a](#), the disk current of the electrode modified by Sb-SAPC15 is  
1529 significantly larger than that of the electrode modified by PCN or PCN\_Na15, indicating  
1530 that the rate of the oxidation reaction taking place on the surface of Sb-SAPC15 is faster  
1531 than that on PCN and PCN\_Na15 ([Supplementary Figure 34b](#)). More importantly, clear  
1532 signals of O<sub>2</sub> reduction to H<sub>2</sub>O were detected by the ring electrode in both cases of Sb-  
1533 SAPC15 with or without light irradiation, verifying O<sub>2</sub> generation on the Sb-SAPC15 surface  
1534 via WOR ([Supplementary Figure 34c](#)). Moreover, the ring current of the electrode modified  
1535 by Sb-SAPC15 under light irradiation is obviously larger than that in the dark condition,  
1536 indicating that photo-induced holes indeed facilitated the WOR. Furthermore, the anodic  
1537 current on the ring electrode under light irradiation appeared much earlier than that in the  
1538 dark condition, which also manifested that the photogenerated holes participated in the  
1539 OER ([Supplementary Figure 34d](#)). Therefore, the highly active photo-generated holes  
1540 boosted the OER via the WOR pathway in the Sb-SAPC15 system.

1541 The water oxidation reaction took place on N atoms of carbon nitride, rather than on the  
1542 Sb atoms, because of the following reasons:

1543 1) Photocatalytic reaction occurs on the surface of a photocatalyst. The excitation  
1544 properties on the surface of photocatalysts have been widely investigated by the cluster  
1545 models, such as N-doped TiO<sub>2</sub><sup>18</sup> and In<sub>2</sub>O<sub>3</sub><sup>19</sup>. The excitation can be systematically  
1546 discussed by combining the simulated UV-vis spectra and transition densities of charge  
1547 carriers. As shown in [Supplementary Figure 37a-c](#), the shape of the computed UV-vis  
1548 absorption spectrum is almost the same as that obtained experimentally, especially in the  
1549 wavelength between 420 nm and 470 nm. To give a comprehensive understanding of the  
1550 transition densities of electrons/holes for boosting the H<sub>2</sub>O<sub>2</sub> production, all transition



1551 densities of the 50 excited states (ES) were summarized in [Supplementary Figure 37d-i](#).  
1552 Electrons are mostly distributed at the C atoms and Sb atoms, while holes are mostly  
1553 distributed at the N sites. To further investigate the excitations that contribute to  
1554 photocatalytic H<sub>2</sub>O<sub>2</sub> production, the excited states 1-16 of Melem\_3, ES 1-15 of  
1555 Melem\_3Na<sup>+</sup> and ES 1-26 of Melem\_3Sb<sup>3+</sup> were highlighted in these figures. On the one  
1556 hand, most of electrons are accumulated at the Sb sites (ES 1-26) of Melem\_3Sb<sup>3+</sup> with  
1557 high density (~20-80%), while most of states show averagely distributed electrons at the C  
1558 sites (< mostly 20%) in the cluster model of Melem\_3 and Melem\_3Na<sup>+</sup>. On the other hand,  
1559 holes are distributed at the N atoms on Melem\_3Sb<sup>3+</sup>, Melem\_3 and Melem\_3Na<sup>+</sup>.

1560 The boundary effect of small cluster models in [Supplementary Figure 37](#) confined the  
1561 distance of possible separated charges. To give a comprehensive assessment of charge  
1562 separation by TDDFT simulation, we built larger models to represent pristine PCN  
1563 (Melem\_6), sodium incorporated PCN (Melem\_6Na<sup>+</sup>) and single atomic Sb incorporated  
1564 PCN (Melem\_6Sb<sup>3+</sup>) to simulate the properties of charge separation ([Supplementary  
1565 Figure 38](#)). Based on the action spectra and the photocatalytic H<sub>2</sub>O<sub>2</sub> production activities,  
1566 the ES 1-26 of Melem\_6, the ES 1-26 of Melem\_6Na<sup>+</sup> and the ES 3-30 of Melem\_6Sb<sup>3+</sup>  
1567 are highlighted in the distribution heatmap of photogenerated electrons and holes  
1568 ([Supplementary Figure 39d-i](#)). It is confirm that most of the electrons are accumulated at  
1569 the Sb sites (ES 3-30, Melem\_6Sb<sup>3+</sup>), a ligand-to-metal charge transfer from neighboring  
1570 melem units to Sb, while most of the states (ES 1-26 for Melem\_6 and Melem\_6Na<sup>+</sup>) show  
1571 averagely distributed electrons at the C sites. The photogenerated electrons and holes  
1572 barely locate at the Na atoms, indicating that the coordinated Na species on the catalyst's  
1573 surface unlikely serve as the active sites for the photocatalytic reaction. The above results  
1574 from Melem\_6, Melem\_6Na<sup>+</sup> and Melem\_6Sb<sup>3+</sup> give almost the same electronic  
1575 configurations as the results from Melem\_3, Melem\_3Na<sup>+</sup> and Melem\_3Sb<sup>3+</sup>  
1576 ([Supplementary Figure 37d-i](#)).

1577 To investigate the properties of charge separation in these three models, the most  
1578 important transitions that can participate in the photocatalytic H<sub>2</sub>O<sub>2</sub> production were figured  
1579 out by checking the oscillator strength of each transition in the UV spectra (as shown in the  
1580 orange dash circles; i. e., the transitions of ES25 and ES26 of Melem\_6, ES9~ES26 of

1581 Melem\_6Na+ and ES3~ES30 of Melem\_6Sb3+)<sup>19</sup>. We then calculated the distance  
1582 between centroid of hole and electron (D index) in these transitions. This D index was  
1583 defined followed by the Manual of the Multiwfn<sup>20,21</sup>, which could reveal whether charge  
1584 separation of photogenerated electron hole pair is efficient. As shown in [Supplementary](#)  
1585 [Figure 40a](#), all of the D index of the transitions of Melem\_6Sb3+ (ES3~ES30) are  
1586 significantly larger than that of Melem\_6 (ES25 and ES26) and Melem\_6Na+ (ES9~ES26),  
1587 indicating that the charge separation is significantly boosted after the introduction of atomic  
1588 antimony sites.

1589 Additionally, another crucial property of photogenerated positive charge carriers  
1590 (photogenerated holes or positive polarons) for facilitating WOR is their high localization  
1591 levels. To simulate the localization level of photogenerated electrons and holes, we  
1592 calculated the hole delocalization index (HDI) and electron delocalization index (EDI) <sup>20,21</sup>  
1593 as defined below:

$$1594 \quad HDI = 100 \times \sqrt{\int [\rho^{hole}(r)]^2 dr} \quad (2)$$

$$1595 \quad EDI = 100 \times \sqrt{\int [\rho^{ele}(r)]^2 dr} \quad (3)$$

1596  $\rho^{hole}$  and  $\rho^{ele}$  respectively indicate the distribution density of holes and electrons <sup>20,21</sup>.

1597 It is found that the smaller the HDI (EDI) is, the larger the spatial delocalization of holes  
1598 (electrons). HDI and EDI are useful in quantifying breadth of spatial distribution for  
1599 electrons and holes. As shown in [Supplementary Figure 40b-c](#), the HDI and EDI of the  
1600 transitions of Melem\_6Sb3+ (ES3~ES30) are significantly larger than those of Melem\_6  
1601 (ES25 and ES26) and Melem\_6Na+ (ES9~ES26), indicating that both of the electrons and  
1602 holes are highly concentrated after introduction of single atomic antimony sites.

1603 2) Additionally, the computational hydrogen electrode (CHE) method also confirmed the  
1604 preferred 2e<sup>-</sup> ORR pathway on Sb-SAPC ([Supplementary Figure 42](#)). This free energy  
1605 diagram could also be used to study the OER activity of Sb sites since the backward  
1606 reaction for 4e<sup>-</sup> ORR is 4e<sup>-</sup> OER. It can be seen that the difference between \*OH and \*O is  
1607 as high as 3.742 eV, indicating that a considerably large energetic barrier needs to be  
1608 overcome for the 4e<sup>-</sup> OER process. In this case, the Sb site should not function as an  
1609 effective site to catalyze 4e<sup>-</sup> OER.

1610 Based on the above evidence, we can draw a conclusion that the Sb sites work as the

1611 2e<sup>-</sup> ORR sites, and the N atoms on melem units work as the 4e<sup>-</sup> OER sites.

1612

### 1613 **Supplementary Notes 8: Simulated Raman spectra for verification of adsorption** 1614 **configurations of O<sub>2</sub>**

1615 To investigate the side-on adsorption of O<sub>2</sub> on PCN, we have re-calculated the possible  
1616 adsorption configurations of O<sub>2</sub> on PCN. In our case, a function of ω97xd at 6-311g(d) level  
1617 was used for optimization to investigate the most favorable adsorption site for O<sub>2</sub> on PCN.  
1618 The initial and optimized configurations are summarized in [Supplementary Table S8](#). The  
1619 calculation results show that the distance between O<sub>2</sub> and Melem\_3 gradually increased  
1620 during the optimization process. Therefore, the side-on adsorption of O<sub>2</sub> is not possible on  
1621 site 2. On the contrary, O<sub>2</sub> can be adsorbed on site 1 of PCN with similar configuration to  
1622 the previous literature. The distance between O<sub>2</sub> and the Melem unit is less than 1.5 Å.  
1623 This bond length indicates that O<sub>2</sub> can be chemically adsorbed on site 1 with a typical side-  
1624 on adsorption configuration.

1625 To further understand the influence of O<sub>2</sub> adsorption configuration on the Raman  
1626 spectrum, we calculated the Raman spectra of the optimized structure for Melem\_3 and  
1627 Melem\_3Sb3<sup>+</sup> after O<sub>2</sub> adsorption. The Raman spectra of Melem\_3 and Melem\_3Sb3<sup>+</sup>  
1628 before O<sub>2</sub> adsorption were also calculated for comparison ([Supplementary Figure 44](#)). A  
1629 new chemical shift appears at around 820 cm<sup>-1</sup> ([Supplementary Figure 44b](#)) after O<sub>2</sub>  
1630 adsorption on Melem\_3. Similarly, a new chemical shift appears at around 780 cm<sup>-1</sup>  
1631 ([Supplementary Figure 44d](#)) after O<sub>2</sub> adsorption on the Sb sites in Melem\_3Sb3<sup>+</sup>. The  
1632 relative position tendency of the changes in these newly observed chemical shifts are  
1633 similar to the experimental results.

1634

### 1635 **Supplementary References**

- 1636 [1] Shiraishi, Y. *et al.* Resorcinol–formaldehyde resins as metal-free semiconductor photocatalysts  
1637 for solar-to-hydrogen peroxide energy conversion, *Nat. Mater.* **18**, 985-993 (2019).  
1638 [2] Gao, J. *et al.* Enabling direct H<sub>2</sub>O<sub>2</sub> production in acidic media through rational design of  
1639 transition metal single atom catalyst, *Chem* **6**, 1-17 (2020).  
1640 [3] Shiraishi, Y. *et al.* Sunlight-driven hydrogen peroxide production from water and molecular  
1641 oxygen by metal-free photocatalysts, *Angew. Chem.* **126**, 13672-13677 (2014).  
1642 [4] Kofuji, Y. *et al.* Carbon nitride–aromatic diimide–graphene nanohybrids: Metal-free

Commented [TB67]: Please change to Supplementary References

Commented [TB68R67]: We have change phrase 'Reference' to 'Supplementary References'.

1643 photocatalysts for solar-to-hydrogen peroxide energy conversion with 0.2% efficiency, *J. Am.*  
1644 *Chem. Soc.* **138**, 10019-10025 (2016).

1645 [5] Kofuji, Y. et.al, Hydrogen peroxide production on a carbon nitride-boron nitride-reduced  
1646 graphene oxide hybrid photocatalyst under visible light, *ChemCatChem* **10**, 2070-2077 (2018).

1647 [6] Kaynan, N., Berke, B.A., Hazut, O. & Yerushalmi, R. Sustainable photocatalytic production of  
1648 hydrogen peroxide from water and molecular oxygen, *J. Mater. Chem. A* **2**, 13822–13826  
1649 (2014).

1650 [7] Wang, L. *et al.* Simultaneous hydrogen and peroxide production by photocatalytic water  
1651 splitting, *Chin. J. Catal.* **40**, 470-475 (2019).

1652 [8] Hou, W.-C. & Wang, Y.-S. Photocatalytic generation of H<sub>2</sub>O<sub>2</sub> by graphene oxide in organic  
1653 electron donor-free condition under sunlight, *ACS Sustainable Chem. Eng.* **5**, 2994–3001  
1654 (2017).

1655 [9] Kofuji, Y. et al. Mellitic triimide-doped carbon nitride as sunlight-driven photocatalysts for  
1656 hydrogen peroxide production, *ACS Sustainable Chem. Eng.* **5**, 6478-6485 (2017).

1657 [10] Qiu, C. *et al.* Photocatalysis: highly crystalline K-intercalated polymeric carbon nitride for  
1658 visible-light photocatalytic alkenes and alkynes deuterations, *Adv. Sci.* **6**, 1970002 (2019).

1659 [11] Bredas, J.-L. Mind the gap! *Mater. Horiz.* **1**, 17-19 (2014).

1660 [12] Qu, X. *et al.* The effect of embedding N vacancies into g-C<sub>3</sub>N<sub>4</sub> on the photocatalytic H<sub>2</sub>O<sub>2</sub>  
1661 production ability via H<sub>2</sub> plasma treatment, *Diamond Relat. Mater. J.* **86**, 159-166 (2018).

1662 [13] Zhu, B., Xia, P., Ho, W. & Yu, J. Isoelectric point and adsorption activity of porous g-C<sub>3</sub>N<sub>4</sub>,  
1663 *Appl. Surf. Sci.* **344**, 188-195 (2015).

1664 [14] Teng, Z. *et al.* Bandgap engineering of ultrathin graphene-like carbon nitride nanosheets with  
1665 controllable oxygenous functionalization, *Carbon* **113**, 63-75 (2017).

1666 [15] Zhang, P. *et al.* Modified carbon nitride nanozyme as bifunctional glucose oxidase-peroxidase  
1667 for metal-free bioinspired cascade photocatalysis, *Nat. Comm.* **10**, 940 (2019).

1668 [16] Kim, S. *et al.* Selective charge transfer to dioxygen on KPF<sub>6</sub>-modified carbon nitride for  
1669 photocatalytic synthesis of H<sub>2</sub>O<sub>2</sub> under visible light, *J Catal.* **357**, 51-58 (2018).

1670 [17] Moon, G.-H. *et al.* Eco-friendly photochemical production of H<sub>2</sub>O<sub>2</sub> through O<sub>2</sub> reduction over  
1671 carbon nitride frameworks incorporated with multiple heteroelements, *ACS Catal.* **7**, 2886-2895  
1672 (2017).

1673 [18] Govind, N., Lopata, K., Rousseau, R., Andersen, A. & Kowalski, K. Visible light absorption of  
1674 N-doped TiO<sub>2</sub> rutile using (LR/RT)-TDDFT and active space EOMCCSD calculations. *J. Phys.*  
1675 *Chem. Lett.* **2**, 2696-2701 (2011).

1676 [19] Ghuman, K.K. *et al.* Photoexcited surface frustrated Lewis pairs for heterogeneous  
1677 photocatalytic CO<sub>2</sub> reduction, *J. Am. Chem. Soc.* **138**, 1206-1214 (2016).

1678 [20] Lu, T. Multiwfn -A Multifunctional Wavefunction Analyzer-Software Manual.  
1679 [http://sobereva.com/multiwfn/misc/Multiwfn\\_3.7.pdf](http://sobereva.com/multiwfn/misc/Multiwfn_3.7.pdf) (2020).

1680 [21] Liu, Z., Lu, T. & Chen, Q. An sp-hybridized all-carboatomic ring, cyclo[18]carbon: Electronic  
1681 structure, electronic spectrum, and optical nonlinearity, *Carbon* **165**, 461-467 (2020).

1682

1683